SHEAR-WAVE AND SPATIAL ATTRIBUTES IN TIME-LAPSE 3-D/3-C SEISMIC AND POTENTIAL-FIELD DATASETS

A Thesis Submitted to the College of

Graduate Studies and Research

In Partial Fulfillment of the Requirements

For the Degree of

DOCTOR OF PHILOSOPHY

in

Geophysics

In the Department of Geological Sciences

University of Saskatchewan

Saskatoon

By

LE GAO

PERMISSION TO USE

In presenting this Dissertation in partial fulfillment of the requirements for a Postgraduate degree from the University of Saskatchewan, I agree that the Libraries of this University may make it freely available for inspection. I further agree that permission for copying of this thesis/dissertation in any manner, in whole or in part, for scholarly purposes may be granted by the professor or professors who supervised my thesis/dissertation work or, in their absence, by the Head of the Department or the Dean of the College in which my thesis work was done. It is understood that any copying or publication or use of this thesis/dissertation or parts thereof for financial gain shall not be allowed without my written permission. It is also understood that due recognition shall be given to me and to the University of Saskatchewan in any scholarly use which may be made of any material in my Dissertation.

Requests for permission to copy or to make other uses of materials in this thesis/dissertation in whole or part should be addressed to:

Head of the Department of Geological Sciences

114 Science Place

University of Saskatchewan

Saskatoon, Saskatchewan S7N 5E2 Canada

ABSTRACT

In this study, I utilize multicomponent time-lapse seismic datasets for investigating subtle seismic properties of Weyburn reservoir undergoing enhanced oil recovery and geologic sequestration of CO_2. The primary focus is on extracting shear-wave information from surface three-dimensional and three-component (3-D/3-C) reflection datasets. Four groups of interrelated objectives are addressed: 1) calibrated and true-amplitude processing of multicomponent time-lapse seismic data, 2) extraction of amplitude variations with angle (AVA) and offset (AVO) attributes for separating pressure and fluid-saturation effects within the reservoir, 3) development of receiver-function methods for investigating the shallow subsurface, and 4) 2-D spatial pattern analysis of attribute maps, intended for automated interpretation of the results and a new type of AVO analysis.

To achieve the first of these objectives, I reprocess the field surface 3-C/3-D reflection datasets by using pre-stack waveform calibration followed by complete reflection processing using commercial ProMAX software. For the second, principal objective of this study, several AVA attributes of the reservoir are examined, including those related to P- and P/S- converted waves and P- and S-wave impedances. The amplitudes and AVA attributes derived from seismic data indicate temporal variations potentially caused by pore-pressure and CO_2-saturation variations within the reservoir. By comparing with AVA forward models, the seismic data suggest correlations between the increasing pore pressure and decreasing AVA intercepts and increasing AVA gradients. Increasing CO_2 saturations appear to correlate with simultaneously decreasing

AVA intercepts and gradients. CO_2-saturated zones are thus interpreted as Class III AVA anomalies.

In order to take further advantage from 3-C recordings and investigate advanced methods for S-wave seismic data analysis, receiver functions are used to study the shallow near-surface structure. This is apparently the first application of this method to reflection seismic datasets on land and in a time-lapse 3-D dataset. I show that it is feasible and useful to measure the near-surface S-wave velocity structure by using multi-component seismic data. From Weyburn reflection data, the average mapped receiver-function time lags are about 35 ms, which corresponds to near-surface S-wave velocities of about 550 m/s. Time-lapse variations of the near-surface structure are measured, and S-wave statics models are derived. Such models can be useful for converted-wave seismic imaging.

The last objective of this Dissertation is to develop tools for interpretation of gridded 2-D spatial images, such as mapping AVO attribute quantitatively and automatically. For this purpose, a new pattern-recognition approach called skeletonization is developed and applied to several regional aeromagnetic and gravity images from southern Saskatchewan and Manitoba. The approach is combined with 2-D empirical mode decomposition allowing pattern analysis at variable spatial scales. The results show that skeletonization helps identifying complex geologic structures and measuring their quantitative attributes that are not available from conventional interpretation. Applications of this approach to interpretation of AVO attributes are discussed.

ACKNOWLEDGEMENTS

First of all, I would like to express my sincere gratitude to my supervisor Prof. Igor B. Morozov for the continuous support of my Ph.D. study and research, for his patience, motivation, enthusiasm, and immense knowledge. His guidance helped me in all the time of research and writing of this thesis.

Besides my supervisor, I would like to thank the rest of my thesis committee: Drs. Christopher Hawkes, Jim Merriam, Samuel Butler and the external examiner Douglas Schmitt (University of Alberta).

I also thank my fellow Ph.D. students in Dr. Morozov's group: Amin Baharvand Ahmadi and Wubing Deng for their interest in this research and numerous discussions. I am also especially grateful to Dr. Jinfeng Ma (Northwestern University, P.R. China) for his contributions to the analysis of Weyburn datasets and many discussions.

This work was facilitated by software grants from Landmark Graphics Corporation (Halliburton) and Hampson-Russell Limited (CGG). Significant portions of this research used IGeoS software by I. Morozov, Matlab, and Generic Mapping Tools.

Last but not least, I would like to thank my husband Tao Chen, my son Noah Chen and my daughter Zoey Chen for numerous support. I also thank my parents Ailing Ma and Liangxiao Gao, for giving birth to me at the first place and supporting me spiritually throughout my life.

SYMBOLS AND ABBREVIATIONS

Symbol	Definition
1C, 1-C	One-Component
1D, 1-D	One-Dimensional
2D, 2-D	Two-Dimensional
3C, 3-C	Three-Component
3D, 3-D	Three-Dimensional
AI	Acoustic Impedance
API	American Petroleum Institute
AVA	Amplitude Variation with Angle
AVO	Amplitude Variation with Offset
BCC	Binary Consistency Checking
CCS	Carbon Capture and Storage (also CO_2 Sequestration)
CMP	Common Mid-Point
CO_2	Carbon Dioxide
EMD	Empirical mode decomposition
EOR	Enhanced Oil Recovery
GLI	Generalized Linear Inversion
GLI3D	Generalized Linear Inverse 3-D (refraction statics program by TomoPlus (previously Hampson-Russell)
IGeoS	Integrated GeoScience Software (by I. Morozov)
NMO	Normal Move-Out

P-wave	Compressional wave
PS, P/S	Converted wave
RF	Receiver Function
RMS	Root-Mean-Square
R_P	Reflected amplitude of P-waves
R_S	S-wave reflectivity in AVO attributes
R_S	Reflected amplitude of S-waves in Zoeppritz equation
SH	S-wave polarized in the horizontal plane
SV	S-wave polarized in the vertical plane
T_P	Transmitted amplitude of P-waves
T_S	Transmitted amplitude of S-waves
V_P	P-wave velocity
V_S	S-wave velocity
VSP	Vertical Seismic Profile

CONTENTS

LIST OF TABLES

LIST OF FIGURES

CHAPTER 1

INTRODUCTION

1.1 Research scope

This dissertation addresses several topics united by a broad topic of analysing the shear- (S-) wave effects in time-lapse three-dimensional and three-component (3-D/3-C) seismic data. Seismic exploration using multicomponent recordings is the subject of extensive studies in both academia and industry providing key information about the properties of subsurface rock. While conventional (single-component) seismic imaging measures only the compressional (P) waves, multicomponent seismic data analysis utilizes multiple wave modes, such as shear (S), surface waves, and converted P/S modes produced upon transmissions or reflections on velocity and/or density contrasts. By analyzing and transforming multicomponent seismic records, additional seismic sections and volumes based on P and S waves can be produced. To extract and fully utilize the information contained in multicomponent data, extensive data analysis is required, including calculation of statics, velocity analysis, imaging, and extraction of additional attributes such as reflection amplitude variations with angle (AVA) or offset (AVO).

Within the general scope above, this Dissertation focuses on the work I conducted within the IEA GHG Weyburn-Midale CO_2 Monitoring and Storage Project in southern Saskatchewan. The seismic component of this work presented in this Dissertation included development and application of four groups of methods: 1) processing of multicomponent time-lapse seismic data using surface reflection 3-D/3-C datasets, 2)

AVA and AVO attributes for separating pressure and fluid saturation effects within the reservoir, 3) receiver-function methods for investigating shallow subsurface using 3-C seismic data, and 4) 2-D spatial pattern analysis of attribute maps, intended for automated interpretation of the results and a new type of AVO analysis.

Time-lapse seismic exploration adds the additional dimension of time to the 3-D analysis of seismic properties of the subsurface. This technology has proven effective for monitoring fluid substitution during enhanced oil recovery or geologic sequestration of carbon dioxide (CO_2). By analyzing time-lapse seismic data, subtle differences are detected between seismic responses in different vintages of reflection datasets. These differences could be caused by changes of reservoir parameters such as pressure, temperature and fluid saturation over the time period between the surveys. These changes in their turn lead to changes in elastic properties such as density, bulk modulus and velocities, all of which affect seismic wave propagation and reflectivity. An important and difficult question arising in applications of this method is in formulating the data processing methods and combinations of data attributes that allow constraining the variations in elastic properties of interest and discriminating between the different physical factors. In this Dissertation, I propose a combination of P/S-wave and time-lapse seismic techniques and AVA analysis to map pressure and CO_2 saturation variations within the reservoir.

The development and application of the methodology and seismic data analysis in this Dissertation are based on time-lapse 3-D/3-C datasets acquired in 1999-2002 for the Phase I of the Weyburn-Midale project. The starting point of my analysis is in estimating the near-surface S-wave velocities by using vertical and horizontal components of

seismic records and deriving accurate S-wave statics. The inversion for a near-surface structure and statics is a key component of any reflection seismic data analysis, because shallow variations of velocity have great impacts on the deep seismic responses. Because of the lack of direct observations of near-surface shear waves, deriving S-wave statics represent a particularly challenging task that has still not been resolved satisfactorily. The receiver-function method appears to be among the most promising techniques for measuring the S-wave statics by analysing the multicomponent waveforms of direct P-wave arrivals. This method is commonly used for mapping the structure of the crust and upper mantle in earthquake seismology (Ammon, 1991). To my knowledge, in this Dissertation, I carry out the first application of this method to land 3-D/3-C reflection seismic data.

The principal approach selected for constraining the S-wave effects in the time-lapse seismic data in Weyburn project is the AVA and AVO analysis, which aims at revealing the variations of seismic responses caused by fluid content and other mechanical properties. Earlier attempts for obtaining reliable converted-wave (P/S) stacked images from these data have been unsuccessful. Nevertheless, because the reflectivity at nonzero angles contains S-wave information, analysis of AVA attributes represents a viable alternative to P/S reflection imaging. The AVA-attribute method is developed in this Dissertation specifically for the Weyburn dataset and applied for extracting empirical pre-stack seismic attributes suitable for separating the effects of CO_2 pressure and saturation. The amplitude versus azimuth and fracturing are out of scope in this Dissertation and would be in the future research. Time-lapse AVO analysis is used to interpret reflection amplitude variations and map them within the reservoir and

potentially to constrain the spatial variations of fluid saturation and pressure. Several new, differential AVA attributes are derived for the combined baseline and monitoring seismic datasets, including the intercept (denoted *I*), gradient (*G*), S-wave reflectivity (*I*–*G*) and a complementary *I*+*G* attribute extracted from pre-stack seismic data. In addition, a new pair of secondary attributes is constructed by considering statistical characterizations of the distributions of *I* and *G*.

The fourth direction of this research relates to quantitative and automated interpretation of mapped AVO anomalies as well as any other geophysical data. Pattern recognition techniques help extracting and interpreting multiple features of the data more completely, precisely, extensively and effectively. Among numerous methods of pattern recognition, a syntactic pattern-recognition method called "skeletonization" is explored. In application to seismic data, this method is capable of identifying spatially-connected wavelets, measuring their parameters, and classifying them. In the past, this method was applied to large volumes of 2-D seismic data for automatic event detection and recognition, and seismic texture and facies analysis, and later extended to arbitrary 2-D gridded geophysical data (Eaton and Vasudevan, 2004). The skeletonization technique is helpful for interpreting various types of feature maps and identifying the boundaries and edges and the correlation of anomalies to geology. I further develop this technique in order reduce its dependence on preferred directions and implement it as part of a powerful and versatile geophysical software package (Morozov, 2009). Although the ultimate goal of this technique is for characterization and interpretation of AVO maps and for high-resolution measurements of AVO effects in pre-stack seismic records, this Dissertation only presents an initial "pilot" development and tests by using regional

potential-field images from Saskatchewan. I also combine the skeletonization with 2-D empirical mode decomposition (EMD) (Morozov, 2009), which allows examining the structures at a hierarchy of scales and exploring them for various quantitative attributes.

1.2 Objectives

Broadly, the presented research program focuses on several types of spatial attributes in time-lapse 3-C/3-D seismic data and potential-field data. The focus of the research is to investigate subtle seismic property variations detected among different acquisition vintages of 3-D/3-C seismic data. The selected attributes take advantage of close acquisition patterns of the time-lapse data and of its three-component and time-lapse character. The specific objectives of this study are as follows:

1. Re-process time-lapse seismic data with identical or close geometries and processing parameters. Several data volumes are generated during this re-processing:
    a. Common Receiver Point (CRP) gathers;
    b. CMP gathers and angle gathers for pre-stack analysis
    c. Stacked data volumes.
2. Pick key horizons, such as caprock and reservoir.
3. Apply the receiver-function analysis to CRP gathers.
4. Perform time-lapse analysis based on full stacked data for amplitude variation and time-shift at the reservoir and proxy area.
5. Perform AVA/AVO analysis on CMP gathers and angle gathers:

a. Derive new AVO attributes suitable for interpretation of time-lapse CO_2 pressure and saturation effects.

b. Interpret the resulting attribute images and correlate with the available injection-well patterns.

6. Develop an improved 2-D pattern analysis (skeletonization) technique and apply it to seismic data and potential-field data for spatial-attribute analysis.

1.3 Structure of this Dissertation

This Dissertation is based on several papers addressing the goals outlined in the preceding section. The relevant papers are listed at the beginnings of the respective chapters.

The Dissertation is organised as follows. Chapter 1 contains a general introduction and formulates the research objectives for this study. Chapter 2 gives an overview of time-lapse reflection seismic data, as well as the background of Weyburn project, a summary of the geology of the Weyburn oilfield, and descriptions of the seismic datasets and processing procedures and parameters. The main part of the data processing and analysis is given in Chapter 3, which describes the time-lapse attribute analysis including reflection time shifts, and measurements of amplitude variations and AVA/AVO analysis. In Chapter 4, I present the receiver function (RF) method, principles of RF interpretation, examples of its previous applications to controlled-source datasets, and an application to the Weyburn field. Chapter 5 discusses the skeletonization approach and its applications to arbitrary gridded data, including pre-stack seismic data and potential-field maps.

Finally, in Chapter 6, I summarize the results of this Dissertation and provide further discussions.

CHAPTER 2

OVERVIEW OF WEYBURN TIME-LAPSE 3-C/3-D SEISMIC DATA

This Chapter gives an overview of Weyburn CO_2 project and geology of the study area, and also describes the initial pre-processing (pre-stack calibration) of the 3-C/3-D surface seismic datasets. The presentation of the seismic data are based on the following publications:

*Baharvand Ahmadi, A., **Gao, L**., Ma, J. and Morozov, I. 2011, CO_2 saturation vs. pressure effects from time-lapse 3-D P-S surface and VSP seismic data: Final report as part of IEA GHG Weyburn-Midale CO_2 Monitoring and Storage Project. 102 pp., http://seisweb.usask.ca/Reports/Weyburn_USask_Report_Apr 2011.pdf, last accessed 20 Oct 2016*

This was a multi-year report for the entire seismic work on this project conducted at our group at the University of Saskatchewan. The placement of the authors was alphabetic, and the chapter "3-D 3-C Surface Data Analysis" in this report was entirely my contribution. The first two sections of this chapter of the report are used in the present Chapter. I expect that material from another chapter of this report about vertical seismic profiles (VSP) will be used by Amin Baharvand Ahmadi in his Ph.D. dissertation at the University of Saskatchewan. There is no overlap between my and Amin's data and studies.

Morozov, I. B., and ***Gao, L****., 2009, Pre-stack calibration of 3-C 3-D time-Lapse Seismic Data,* Proceedings of *2009 CSPG/CSEG/CWLS Convention, Calgary, AB, Canada,* Calgary, AB, Canada, *p. 215-219,*http://cseg.ca/assets/files/resources/abstracts/2009/101.pdf, last accessed 20 Oct 2016.

In this paper, my supervisor (Dr. I. Morozov) developed the software for pre-stack calibration, and I developed the processing procedures and applied the calibration to the data, conducted testing of the codes and checked the results. I estimate my contribution to this paper as 40%.

Ma, J., ***Gao, L****. and Morozov, I., 2009. Time-lapse repeatability in 3-C-3-D dataset from Weyburn CO_2 Sequestration Project,* Proceedings of 2009 CSPG/CSEG/CWLS Convention, Calgary, AB, Canada, p. 255-258,http://cseg.ca/assets/files/resources/abstracts/2009/096.pdf, last accessed 20 Oct 2016.

In this paper, Dr. Ma formulated the general approach and wrote the paper. I performed tests of the methods and final data analysis. I estimate my contribution to this paper as 30%. These contributions are described in subsections 2.3.2 and 2.3.3.

Copyrights for the above publications belong to the authors. The papers and the corresponding chapter in Weyburn report were shortened, modified to provide links to other parts of this Dissertation and reformatted for inclusion in this Dissertation. Some of the figures were also re-plotted differently, and bibliographic references were integrated at the end of this Dissertation.

2.1 Weyburn project

Most of the present research was conducted as part of the Final (second) phase of the International Energy Agency Greenhouse Gas (IEA GHG) Weyburn-Midale CO_2 monitoring and storage project (IEA GHG, 2004). This project represented a major international collaborative scientific study to assess the technical feasibility of CO_2 storage in geological formations with a focus on oil reservoirs. One of the principal goals of this project was the development of world-leading best practices for implementation of carbon capture and geological CO_2 sequestration (CCS). The research on CO_2 geological storage and CO_2-injection based enhanced oil recovery (EOR) in the Weyburn oilfield in southeastern Saskatchewan (Figure 2.1) was started in October 2000. The IEA R&D Programme (IEA GHG) and other research groups participated in it due to the recognized global significance of CCS for mitigation of projected climate change. This project included several research themes, in which the seismic data analysis was included under the theme on storage monitoring methods.

After Phase I of the Weyburn IEA GHG project was completed (Weyburn Phase I Report, 2004, editors: M. Wilson and M. Monea), the final phase was initiated in 2005 and largely completed by the end of 2011. The research at the final phase focused on assessment for monitoring techniques and validation of CO_2 geological storage. In this study, the datasets acquired for Phase I in 1999, 2001 and 2002 are used. Because all three of the available datasets belong to the early stages of CO_2 injection, this Dissertation focuses on development and testing of seismic imaging and data analysis methodology rather than on detailed operational monitoring of the reservoir.

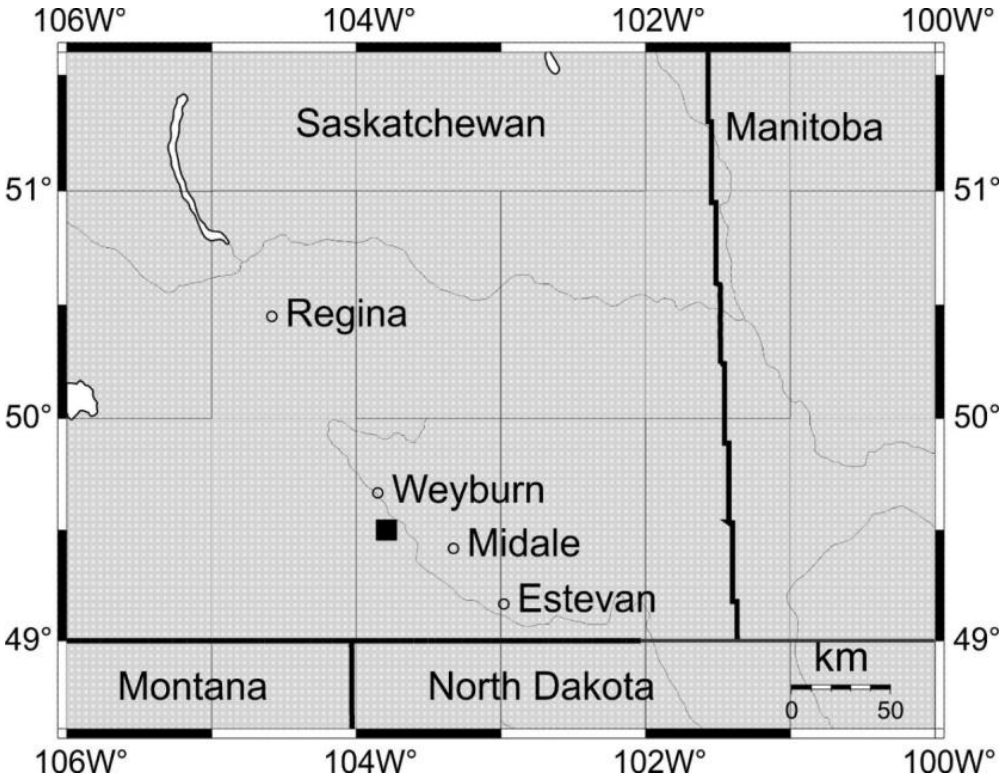

Figure 2.1. Location of Weyburn Oil Field in south-eastern Saskatchewan (highlighted in black).

2.2 Geological overview of Weyburn oilfield

The Weyburn oilfield is located within the Williston Basin in the southeast corner of the province of Saskatchewan in Canada (Figure 2.1). This field was discovered in 1954 and produced on primary production until 1964 at 22° to 35° API gravity (Wegelin, 1984), that is, around 920 to 849 kg/m^3 (crude oil with API gravities in the 25° to 35° range), after which its water flooding began. In October 2000, CO_2 injection was started with commercial CO_2-based EOR operations. The Weyburn oilfield contained approximately 1.4 billion barrels of original oil in place. CO_2 injection resulted in incremental production of 18,000 barrels per day, with total production of about 28,000

barrels per day. By the end of 2011, approximately 18 million tonnes (Mt) of anthropogenic CO_2 had been stored in the Weyburn reservoir.

The Weyburn reservoir is located the fractured Midale beds of Mississippian age carbonates at an average depth of 1.5 km. Figure 2.2 shows the stratigraphic column of the Williston Basin. The thickness of Midale reservoir beds is relatively small and ranges from 16 to 28 m, which are divided into two main zones: 1) an upper dolostone Marly, which is 3-10 m thick (mean of ~6m) and 2) lower limestone Vuggy, which is 8 to 22 m thick, with a mean of about 7 m. The Marly zone has porosity from 16% to 38%, with an average of 29% and the permeability ranges from 1 md to over 100 md, with an average of ~10 md. The porosity of the Vuggy zone is relatively low and ranges from 8% to 20%, with an average of ~10% and much higher permeability of 10 to over 300 md, with an average of ~50 md (Brown, 2002). The seal over the Marly and Vuggy reservoirs consists of a highly-competent sedimentary anhydrite, which is in evaporitic dolomite and shale sequence ranging from 1 m to more than 10 m in thickness.

The porous but less permeable Marly is the main target for CO_2 flooding, with 75 injection patterns being used for maximizing the oil production and recovery (Hancock, 1999). The injected CO_2 migrates laterally and downwards, which is caused by the variations of pressure and differences between the porosity and permeability of Marly and Vuggy zones. The residual oil is driven by this pressure into the horizontal and vertical production wells. In order to monitor the injection, CO_2 storage, and oil recovery, 3-D and 3-C/3-D seismic data were acquired nearly annually, starting from a baseline survey in December 1999 (White et al., 2004). The main objective of this monitoring was to track and quantify the distribution of CO_2 within the subsurface (Gao

and Morozov, 2011; White, 2009). Three of the earlier 3-C/3-D vintages of the data acquired under Phase I of the Weyburn CO_2 project (1999, 2001, and 2002) are used in this Dissertation.

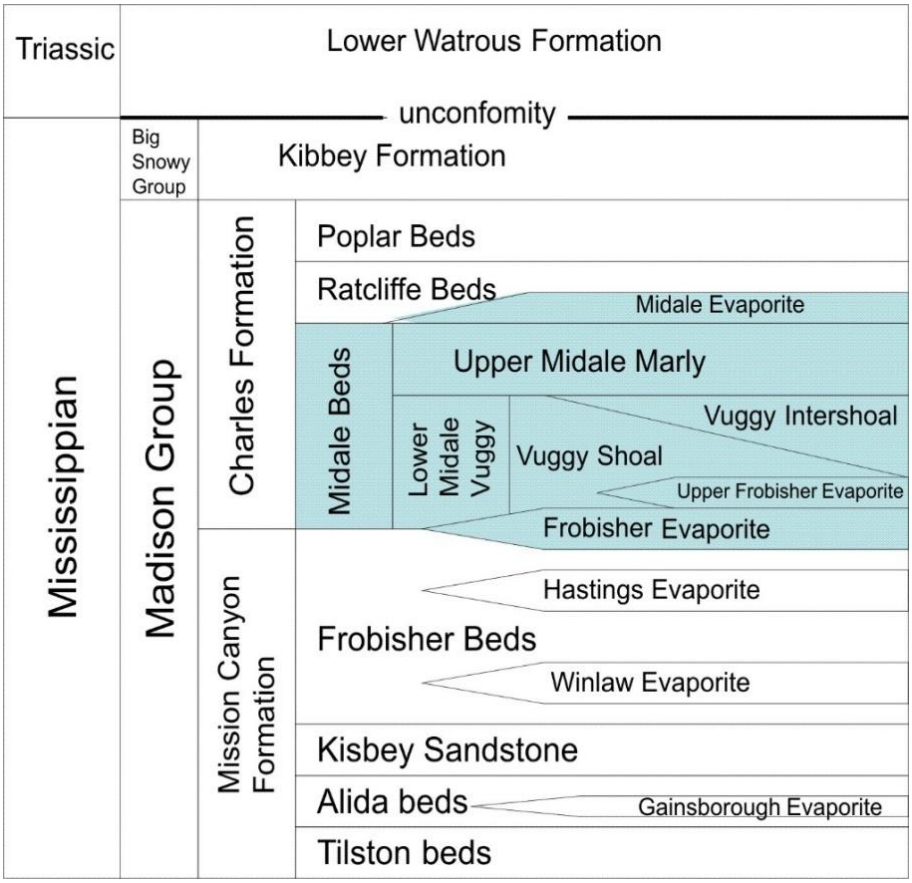

Figure 2.2. Stratigraphic column of Weyburn oilfield. The reservoir zone is highlighted in cyan.

2.3 Seismic data processing

Seismic data reduction and processing was applied to the seismic data by using commercial ProMAX software (Landmark Graphics, Halliburton) and the in-house software package IGeoS at the University of Saskatchewan (Morozov, 2008). Because of its unparalleled flexibility, the use of IGeoS was particularly beneficial for complex tasks

utilizing multiple 3-C datasets, such as pre-stack time-lapse calibration described in subsection 2.3.1. The general processing procedure (subsection 2.3.2) was standard for reflection seismic processing, with additional measures taken to maintain consistency between the three time-lapse datasets. One of the most critical steps of reflection data processing consists in inversion for refraction statics. This inversion was also carried out in a time-lapse consistent manner (subsection 2.3.3).

Consistency of the data analysis is the most critical factor for time-lapse seismic monitoring. Therefore, calibration of the different vintages of the datasets is vital for subsequent data analysis. The calibration includes corrections for variable acquisition conditions and processing procedures. Because the principal tools of data analysis in this Dissertation are pre-stack (AVO and receiver-function method), the calibration also had to be conducted in the pre-stack domain in order to keep consistency for different vintages. The consistency of pre-stack time-lapse datasets implies similar acquisition and processing. During acquisition, constant source and receiver positions should be used, similar charge types and sizes are required, and similar other recording conditions should be maintained. As shown in Table 2.1, these conditions are satisfied by the three Weyburn datasets reasonably well, although the datasets (and particularly the 2001 monitor) contain differences in shot numbering and use different types of geophones. During time-lapse data processing, common binning, identical processing steps, wavelet equalization and statics and velocity models should be correlated between the different seismic datasets (Morozov and Gao, 2009). The standard procedure of seismic processing is insufficient for preservation of amplitude variations with offset, and also for correlation of amplitudes and phases between different time-lapse datasets.

Table 2.1. Weyburn surface 3-D/3-C acquisition parameters.

Parameters\Year	Baseline (1999)	Monitor (2001)	Monitor (2002)
Number of shots	630	882	630
Number of Receiver stations	986	986	986
Sample rate	2 ms	2 ms	1 ms
Maximum offset	2152.87 m	3445.84 m	2105.627 m
Maximum fold	77	132	78
Source type	Dynamite,1 kg, 12 m	Dynamite, 1kg, 12 m	Dynamite,1 kg, 12 m
Receiver type	Mitcham, 3-C 10Hz Damping 70%	OYO, 3-C 10Hz Damping 1%	I/O, VectorSeis, 3-C, MEMS
Source interval	160 m	160 m	160 m
Receiver interval	160 m	160 m	160 m
Swath	19 lines × 39 stations	19 lines × 39 stations	19 lines × 39 stations

2.3.1 Repeatability measurements

Although the geometries and acquisition parameters of Weyburn time-lapse datasets were close, they were not completely identical (Table 2.1), and the resulting differences in recorded parameters need to be assessed and mediated. Without repeatability measurements, interpretation of the differences between the baseline and monitor datasets can be problematic (Altan, 1997), and particularly with respect to extraction of AVA attributes. Together with Dr. J. Ma, I performed repeatability measurements of the available three vintages of the vertical-component data by using the traditional techniques

(Ma et al., 2009). I compared the source and receiver coordinates from different acquisition years and measured amplitudes and phases in shot and CMP gathers. These measurements help in evaluating the repeatability limitations resulting from seismic acquisition and developing the calibrated processing sequence and its parameters.

In each of the monitor datasets, we measured the deviations of the source and receiver coordinates and elevations, first-break time shifts and amplitude variations in shot gathers. We also checked the differences in offset and azimuth distributions between the baseline and monitor datasets.

The source and receiver coordinates show moderate but significant differences in the three vintages (Figures 2.3 and 2.4). For most source and receiver locations, monitor coordinates deviate by several meters, with occasional 20-m deviations noted from the baseline dataset. Elevation deviations of the sources and receivers are mostly within 0.5 m. Considering that the data were acquired by re-deploying the geophones for each monitor survey, the achieved field repeatability of spread locations is good. However, the observed deviations in the source and receiver coordinates still remain among the main reasons causing time shifts and amplitude variances in the monitor datasets.

First-arrival travel-time differences were measured in several shot gathers of the baseline and monitor datasets. For shot 2116171 (Figure 2.5), the time shifts between the 2001 monitor and baseline are around –10 ms. Between the 2002 monitor and the baseline, the time differences are around 6 ms. However, these time differences also depend on receiver locations, which makes it difficult to align all first breaks accurately. These shifts could be related to the variations in the subsurface conditions.

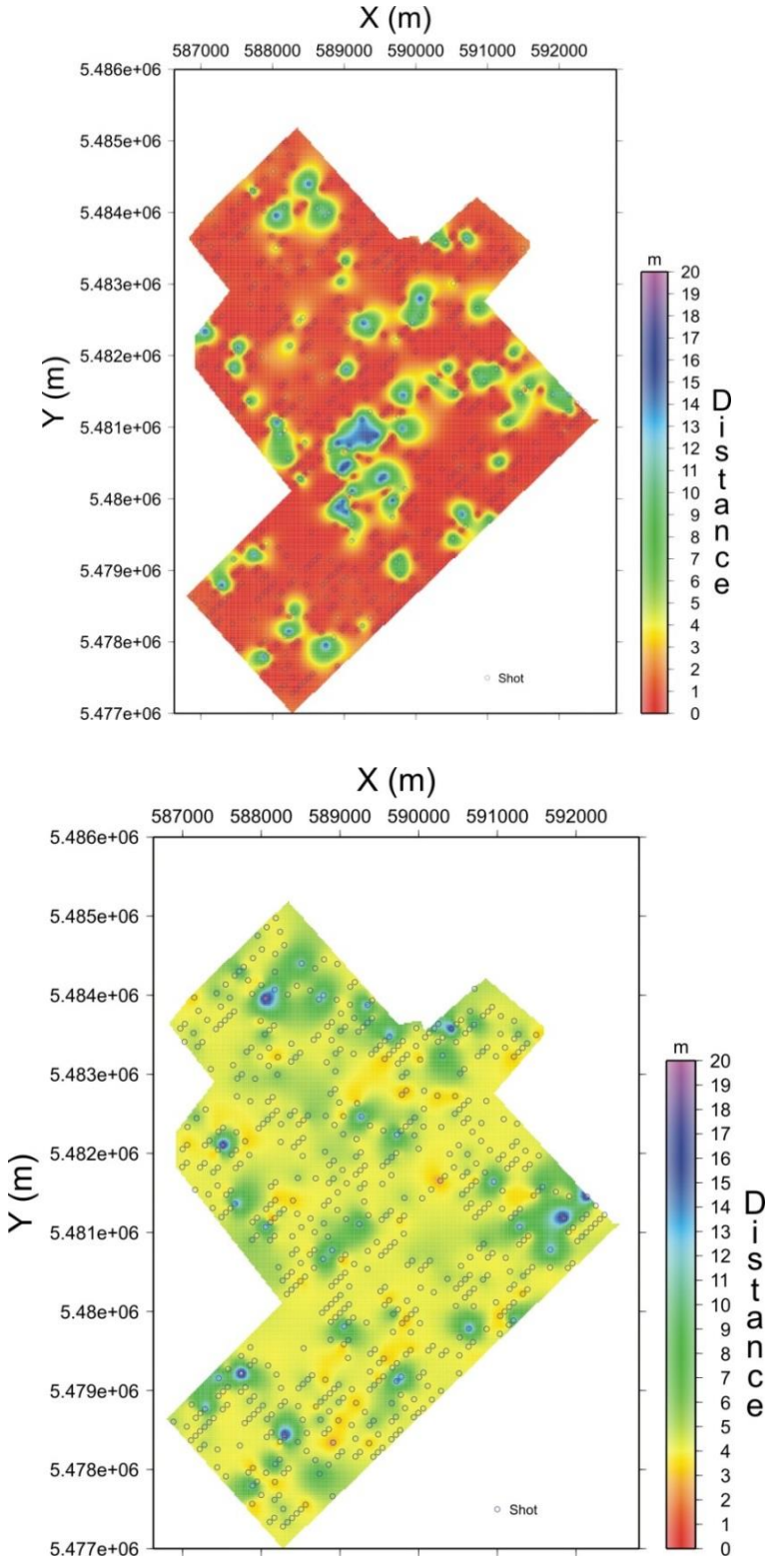

Figure 2.3. Shot coordinate deviations. Top: distances between shot positions in 2001 and 1999; bottom: distances between shots in 2002 and 1999 datasets.

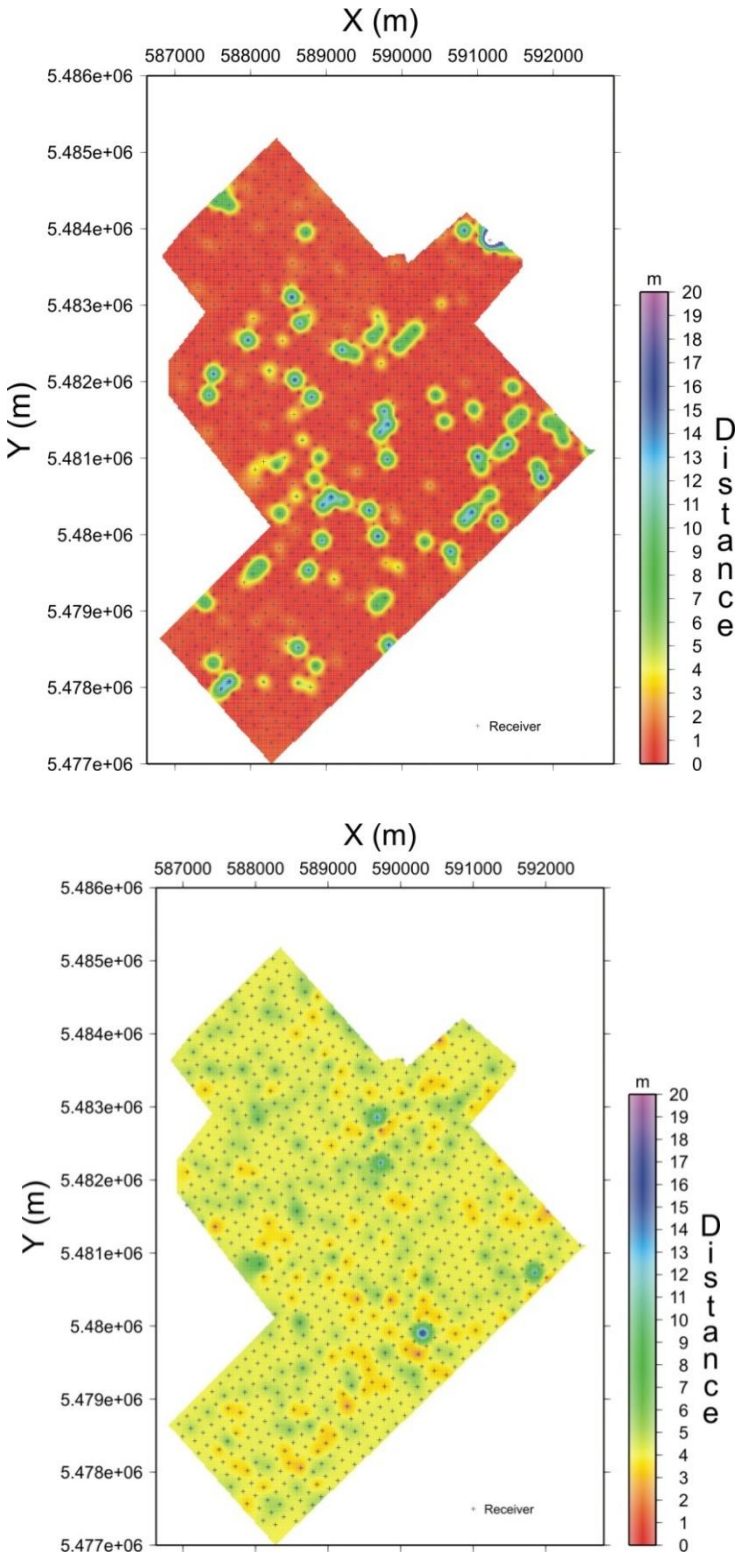

Figure 2.4. Receiver coordinate deviations. Top: distances between receiver positions in 2001 and 1999; bottom: distances between receiver positions in 2002 and 1999.

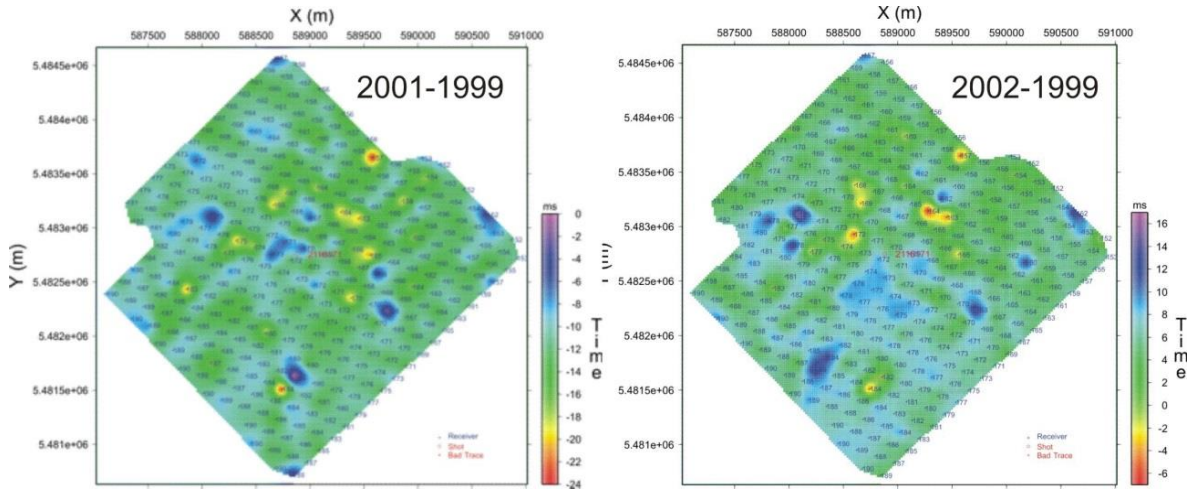

Figure 2.5. First-break time deviations of 2001 and 2002 datasets compared with baseline, for shot 2116171.

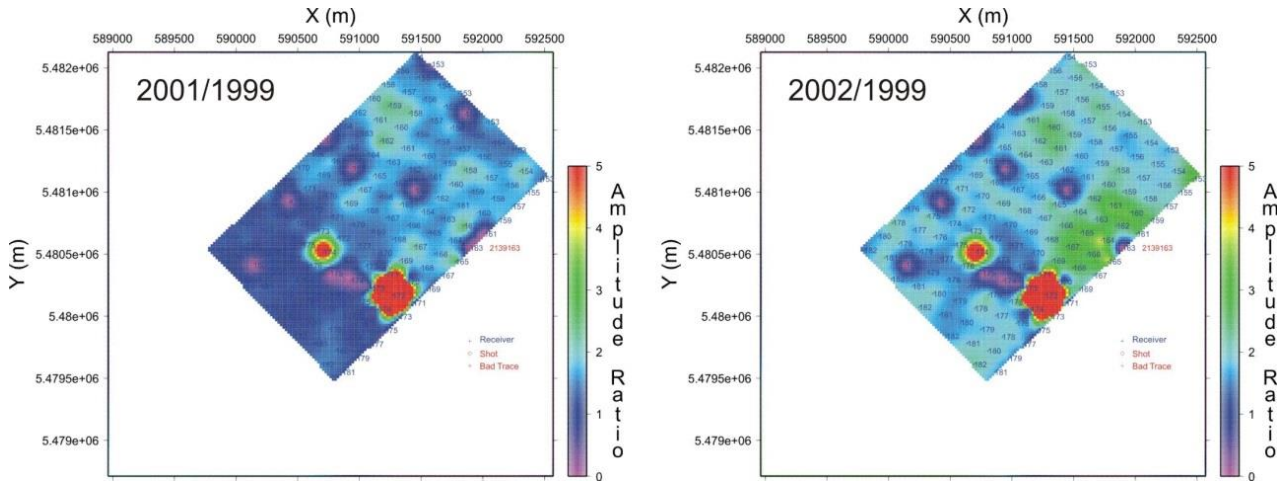

Figure 2.6. First-break average amplitude ratios for 2001 and 2002 with baseline, in shot 2139163.

In order to check the consistency of amplitudes, first-arrival amplitude ratios were measured (Figure 2.6). As an example typical of the 2001 survey, shot 2139163 shows a characteristic amplitude decrease in the south of the swath (Figure 2.6). This difference should be due to the fact that this shot was actually conducted as two separate shots during the data acquisition. Further inconsistency of first-arrival amplitudes could be

caused by geophone coupling, spectral differences between the shots, and potentially variations in the near-surface velocity and attenuation.

A certain level of non-repeatability of amplitudes in shot gathers still does not automatically mean the same in the CMP domain. The consistency of NMO velocities, folds, offset ranges, and azimuths may cause additional uncertainties in stacked amplitudes and also lead to incorrect AVA inversion. Therefore, I performed similar repeatability measurements in CMP gathers. The general result confirmed the above observations of the 2001 dataset being less repeatable compared to 1999 and 2002.

I also checked the resulting stacked amplitude variations above and below the reservoir (Figure 2.7). The measurements were repeated before and after the residual static correction. The 2001 dataset still showed some inconsistency in the middle of the observation area, and the 2002 monitor showed a better repeatability (Figure 2.7). In addition, acquisition footprints (edges of shot swaths) are visible in the 2001 to 1999 data comparison (Figure 2.7, left). As above, the non-consistency of the amplitude ratios should relate to the difference in the geometries of shot swaths used in the 2001 survey.

2.3.2 Pre-stack calibration of time-lapse data

In order to achieve a consistent and true-amplitude pre-stack processing, pre-stack, trace-by-trace calibration of all datasets was performed before any reflection data processing. All three vintages of 3-C pre-stack data were combined in a single 9-C seismic dataset grouped into “trace ensembles” for the individual source-receiver pairs. Within each source-receiver group, the following operations are applied to adjust each monitor-dataset record the corresponding baseline record (Morozov and Gao, 2009):

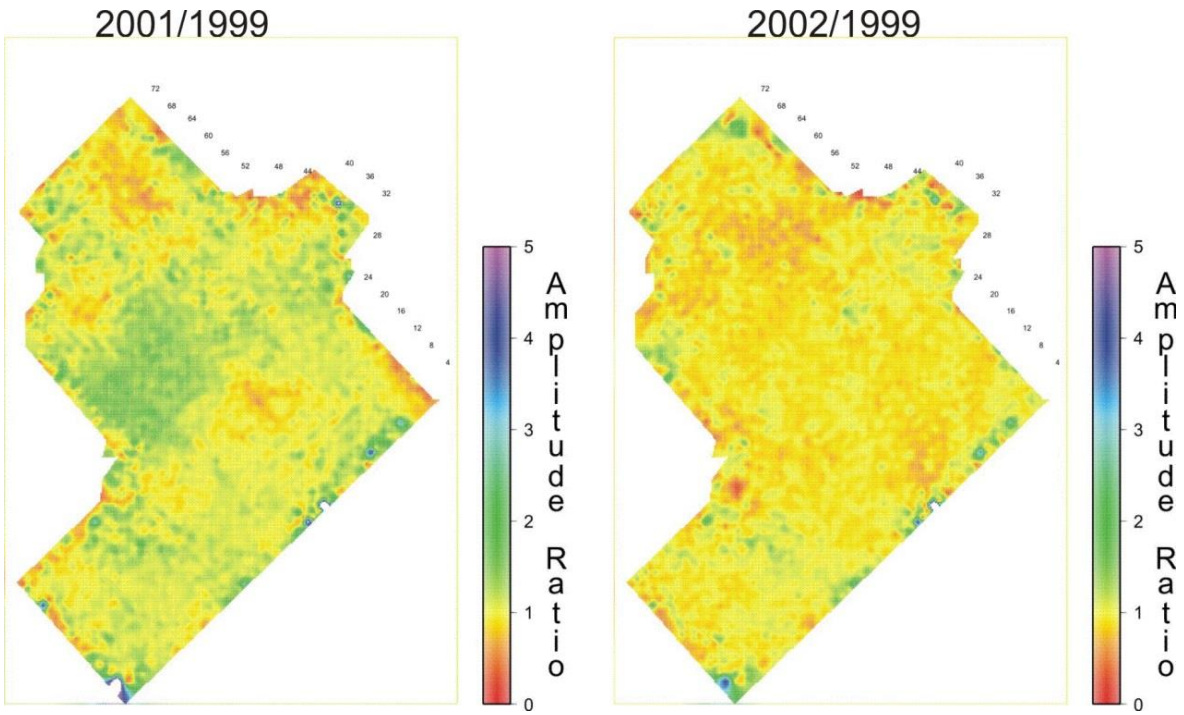

Figure 2.7. Average amplitude ratio in stacked data above the target zone (near 750 ms). Left: 2001/1999 ratios; Right: 2002/1999 ratios. Note the stronger variations and acquisition footprint in the 2001/1999 amplitude ratios.

1) First-arrival and reference-horizon time matching by static shifts and time shifts, respectively.

2) Amplitude scaling and wavelet phase rotations.

3) Spectral balancing.

As a result of these corrections, the three vintages of the seismic dataset attain common timing and similar spectra. Based on this common pre-stack timing, common P-wave refraction and stacking-velocity models were used in subsequent reflection data processing. These common models were associated with the baseline dataset.

As an additional result of this calibration procedure, a number of differential properties are extracted directly from the pre-stack data, such as differences in statics (denoted Δt below), in logarithms of amplitudes ($\Delta \log A$), or relative spectral slopes ($\Delta(d\log A/df)$; this parameter is also known as t^* in earthquake seismology). To a zero-order approximation, such parameters (denoted p in the equation below) can be decomposed into the corresponding source and receiver contributions:

$$\Delta p_{SR} \approx \Delta p_S + \Delta p_R \,. \tag{2.1}$$

The separated contributions from sources and receivers represent important time-lapse information and could be used, for example in time-lapse surface-consistent deconvolution (Morozov and Gao, 2009). Figure 2.8 shows such variations of the source and receiver static shifts between the two monitor and baseline datasets. Interestingly, the time-lapse variations of the source statics show clear correlation with the acquisition pattern, whereas receiver statics variations are less systematic (Figure 2.8).

Finally, at the end of the calibration procedure, the horizontal-component data are rotated into radial and transverse directions. Ideally (in a horizontally-layered Earth), the vertical and radial responses contain the P- and SV- wave amplitudes, and the transverse component would only contain SH waves.

2.3.3 Reflection data processing

Based on the calibrated pre-stack 3-C data, common processing procedures and identical parameters were applied to each vintage of the data, including de-noising, geometrical spreading correction, multiple attenuation, and refraction statics application.

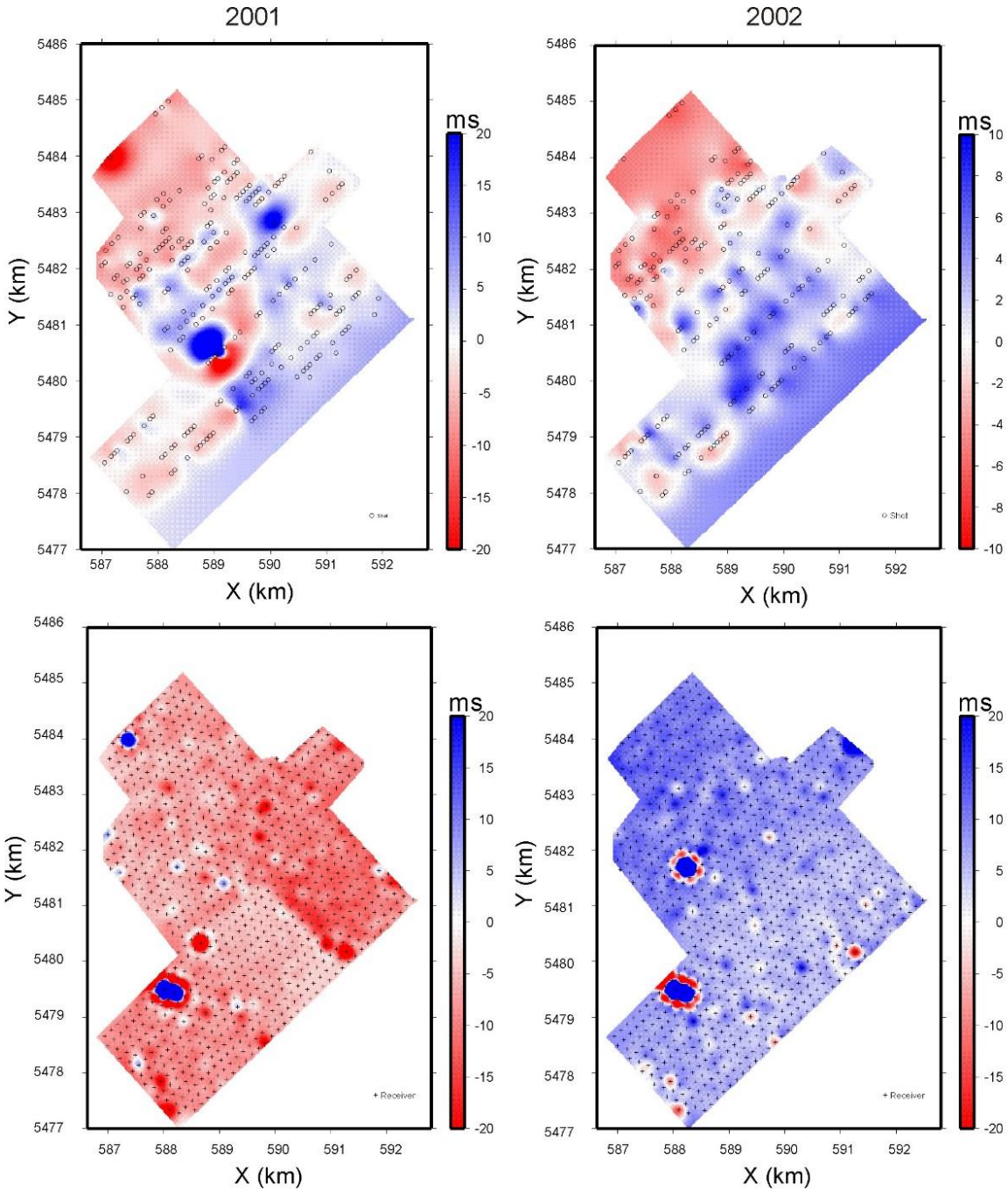

Figure 2.8. Differential time shifts (statics) measured between the pre-stack, vertical-component 2001 and 2002 monitor datasets and the baseline. Upper row: source static terms Δt_S in eq. (1); bottom row: receiver terms Δt_R.

Bad traces were removed by trace editing. Identical geometry, statics, and RMS velocity models were used for three vintages of dataset. CMP bin size of 80×80 m is applied to match the nominal source and receiver intervals of 160 m. Processing parameters are given in Table 2.2, and the geometries of shots and receivers are shown in Figure 2.9.

Table 2.2. Processing sequence and parameters for 3-D surface datasets.

WEYBURN 3-D – Processed by ProMAX software.	
P-WAVE (1999, 2001 and 2002 SURVEY)	
PROCESS	**PARAMETERS**
PROCESSED LENGTH: SAMPLE RATE: GEOMETRY – 3-D CASE BIN SIZE = 80 m×80 m	3000 ms 2 ms
MANUAL TRACE EDITS	
AMPLITUDE EQUALIZATION TYPE: COMPONENTS APPLIED: SPHERICAL DIVERGENCE:	 SURFACE CONSISTENT SHOT, RECEIVER 1/DISTANCE
SURFACE CONSISTENT DECON:	PREDICTIVE
STRUCTURE STATICS METHOD: NUMBER OF LAYERS: WEATHERING VELOCITY: DATUM ELEVATION: REPLACEMENT VELOCITY:	 G.L.I 2 1000 m/s 600 m ASL 2000 m/s
PRELIMENARY VELOCITY ANALYSIS TYPE: REFERENCE:	 INTERACTIVE VELOCITY ANALYSIS (VELOCITYIES FROM YEAR 1999 BASE SURVEY) SURFACE
NORMAL MOVEOUT CORRECTION	

STRETCH MUTE PERCENTAGE	30
RESIDUSTAL STATICS	2D/3-D MAX. POWER AUTOSTATICS
3-D STACK	

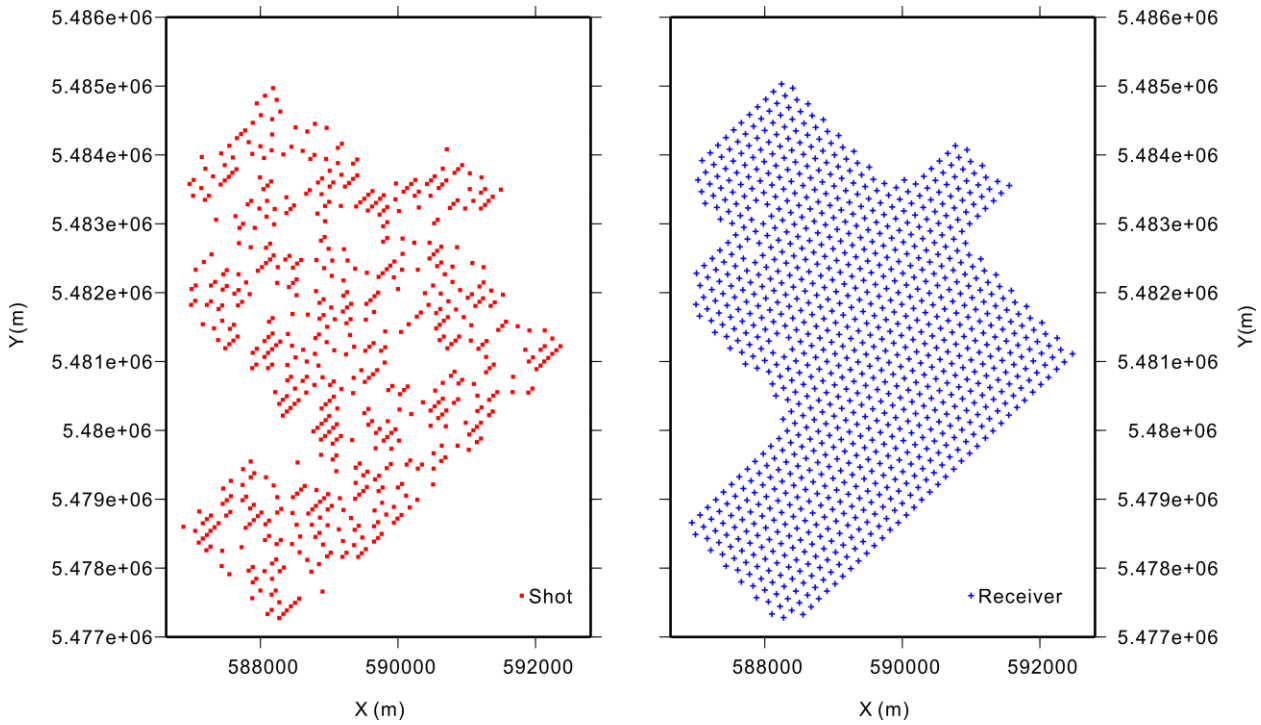

Figure 2.9. Locations of shots (red dots; left) and receivers (blue dots; right).

As a first step of data processing, geometry information was extracted from SEGY trace headers and loaded into ProMAX for all three years of acquisition. With 80×80 grid bin size, 6205 CDPs were created in 73 inlines and 85 crosslines. A fold map of the survey is shown in Figure 2.10. Second, in order to preserve true amplitudes for the subsequent data analysis, predictive surface-consistent deconvolution was applied to equalize the source and receiver responses, and band-pass Ormsby filters of 10-20-100-200 Hz were used to suppress noise outside of the recorded frequency band. In the third step, by using the program GLI3D of GeoTomo software (Hampson-Russell at the time

of this work), a two-layer refraction model was built with the first-arrival input picked from 1999 data in ProMAX. Using these picks, refraction statics for all sources and receiver were estimated as described in the next subsection. The derived refraction static corrections were imported back into ProMAX and applied to all three vintages of data. Next, stacking velocity analysis was performed in ProMAX by using CMP super-gathers with 5×5 inline and crossline ensemble sizes. The obtained stacking velocities were used for normal move-out (NMO) corrections in order to create pre-stack datasets for AVO analysis.

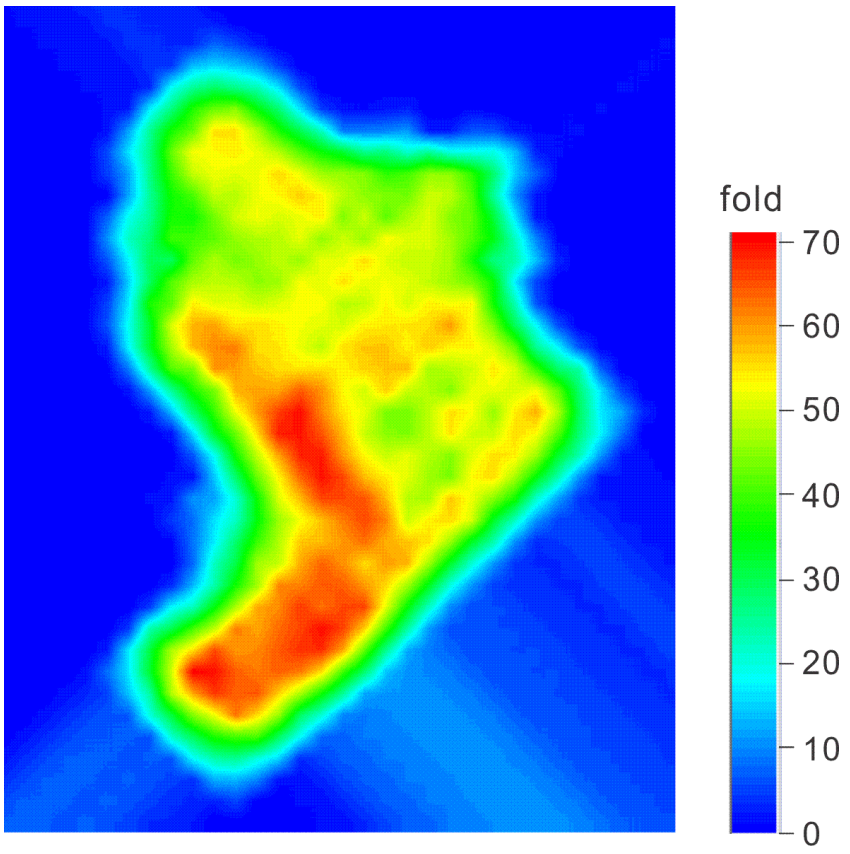

Figure 2.10. CMP fold map. The fold number is the largest (~70) in the southwestern part of the study area.

Finally, the NMO-corrected seismic traces were stacked to produce 3-D volumes that were used for displays and input in further time-lapse analysis. One line from the resulting 3-D vertical-component seismic volumes and the key horizons is shown in Figure 2.11.

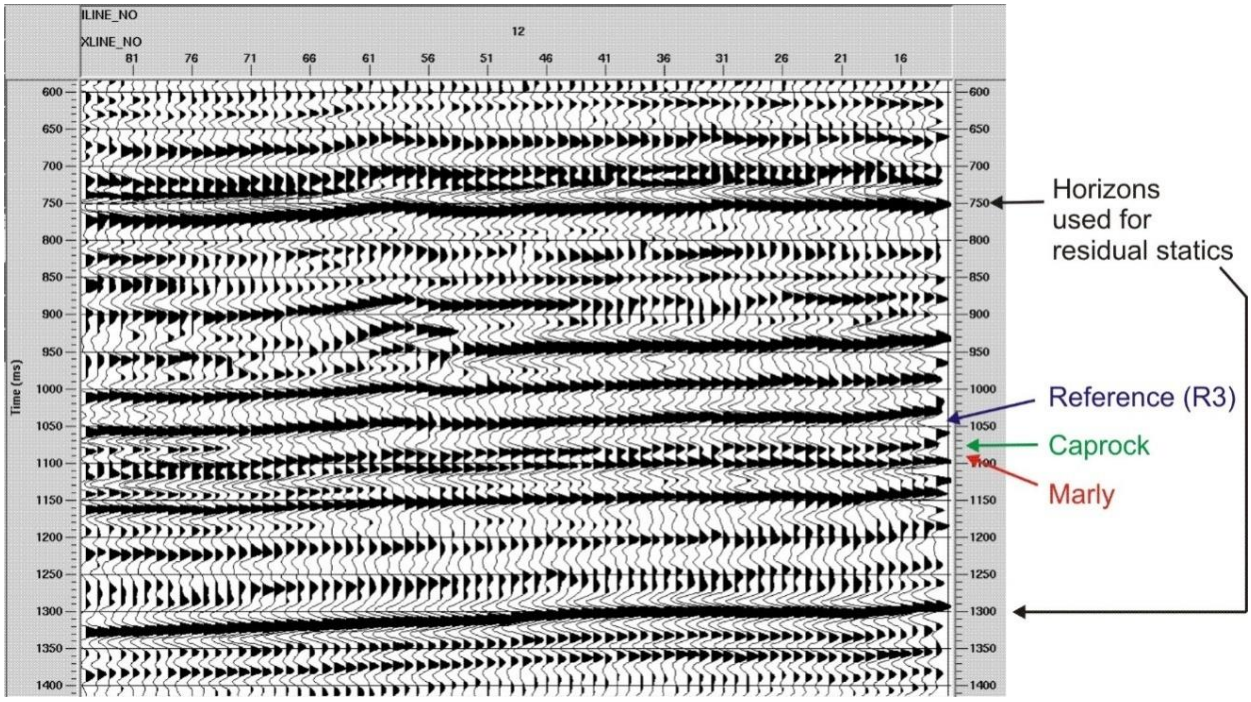

Figure 2.11. One line from baseline (1999) vertical-component stacked section. Labels indicate the key horizons used for calibration of the time-lapse datasets and interpretation.

2.3.4 Refraction statics

Program GLI3D by Hampson-Russell (currently this program is included in GeoTomo software) was used to derive the refraction-statics model. This approach is based on tomographic inversion for a layered near-surface velocity structure. It appears to be the most accurate and advanced and is broadly used in the reflection-data processing industry. Because the calibration procedure (subsection 2.3.2) achieves identical timing for the first arrivals in all three vintages of the data, a single refraction statics model was

inverted from the baseline dataset and applied to all three calibrated datasets. The GLI3D procedure derived the P-wave statics in three basic steps: 1) building an initial 1D near-surface model at a set of control points by using the first-arrival times (picked and output from ProMAX), 2) obtaining an improved tomographic model by using an iterative least-squares algorithm (called the Generalized Linear Inversion (GLI) in this approach) and 3) calculating the static corrections by using the travel times for rays traced vertically through this model (Figure 2.12). During the calculation, a set of control points (shots) were selected from the initial model (Figure 2.13).

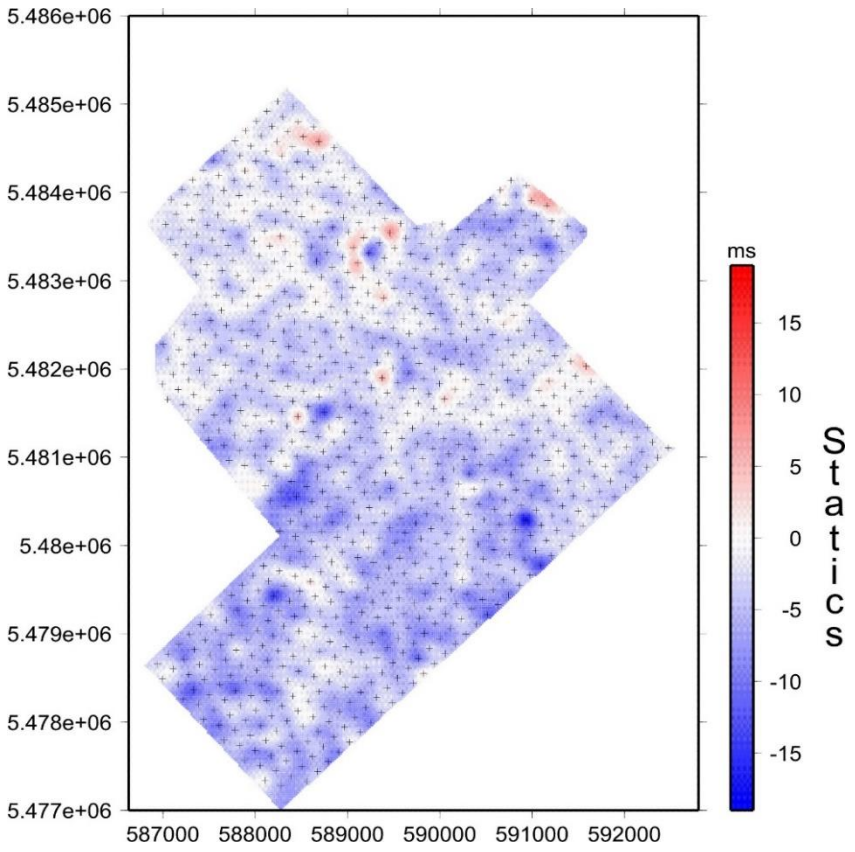

Figure 2.12. Baseline (1999) receiver statics obtained by using GLI3D program

The resulting GLI3D model shows that the average depth of the shallowest resolvable refractor in the shallow subsurface is near 26 m (Figure 2.14). The average P-wave velocities above and below this refractor were estimated as 1966 m/s and 2300 m/s respectively. This refractor corresponds to the bottom of the layer shown in blue in Figure 2.14. As it will be shown in Chapter 4, this boundary also produces P/S wave mode conversions in the first-arrival waveforms. These mode conversions can be used for constructing receiver functions and estimating the S-wave velocities within the shallowest layer in Figure 2.14.

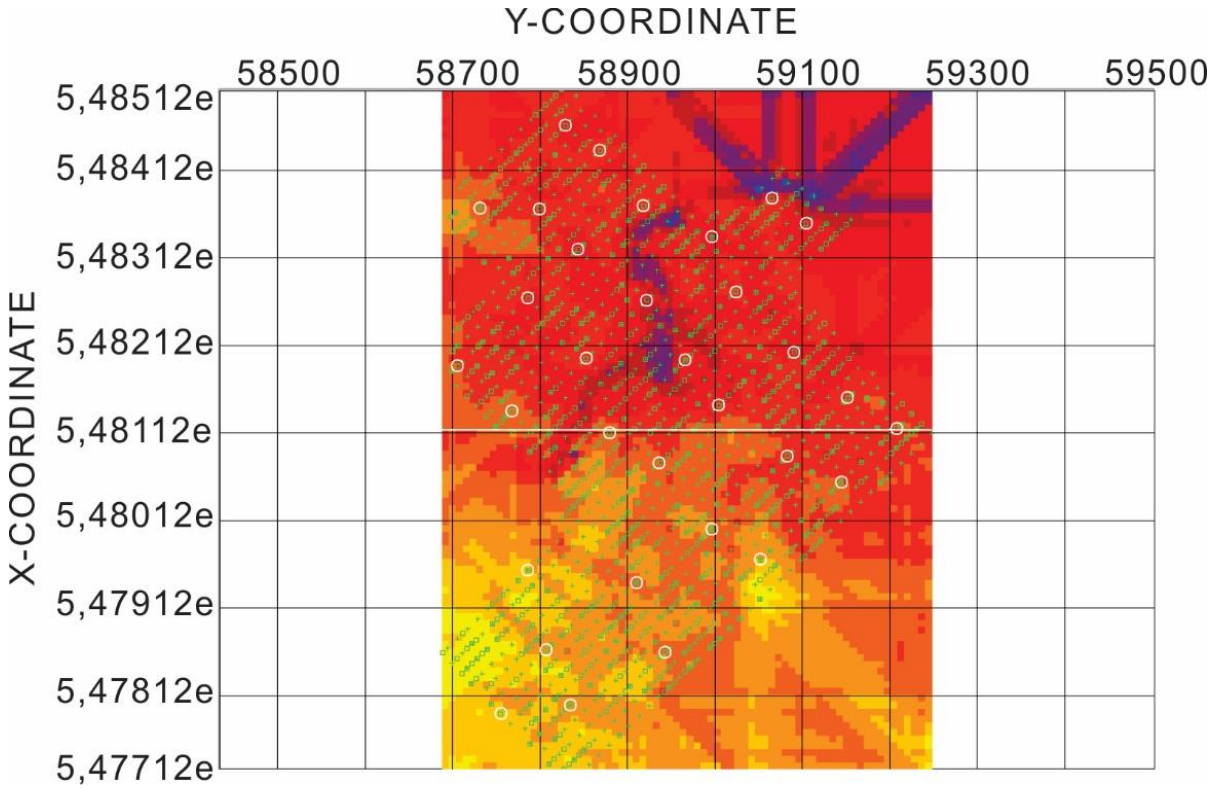

Figure 2.13. Control points for GLI initial model (white circles). Green squares and crosses are shots and receivers, respectively.

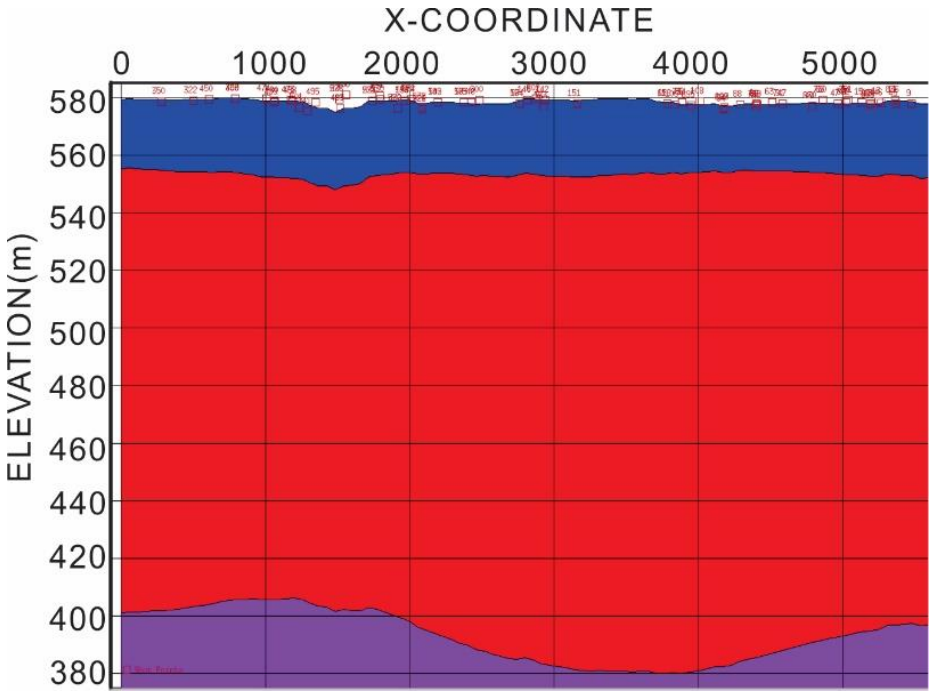

Figure 2.14. GLI3D velocity model. Squares above the top of the model correspond to the control points in Figure 2.13.

CHAPTER 3

TIME-LAPSE ANALYSIS OF 3-C/3-D SEISMIC DATA

When interpreting the *P*- and *S*-wave reflection amplitudes of the reservoir, my primary goals are 1) to measure the amplitude variations between the baseline and monitor datasets and 2) to relate these variations to the *in situ* pressure and CO_2 saturation within the reservoir. These two goals are addressed in this Chapter. After careful pre-stack calibration (Chapter 2), small time-lapse variations in the AVO/AVA attributes and seismic impedances can be measured. For a relatively thin Weyburn reservoir, these attributes need to be modeled by taking into account the specific layering and seismic wavelet. This modeling is described in section 3.1 and leads to recommendations about the types of AVO attributes that can be sensitive to CO_2 pressure and saturation variations. Application of these attributes is described in section 3.2, and the key observations are summarized in section 3.3.

The presentation in this Chapter is based on the following papers:

*Baharvand Ahmadi, A., **Gao, L**., Ma, J. and Morozov, I., 2011, CO_2 saturation vs. pressure effects from time-lapse 3-D P-S surface and VSP seismic data: Final report as part of IEA GHG Weyburn-Midale CO_2 Monitoring and Storage Project. CA, 102 pp.http://seisweb.usask.ca/Reports/Weyburn_USask_Report_Apr2011.pdf, last accessed 20 Oct 2016*

My contributions to this report were explained at the beginning of Chapter 2. The introductory section 3.1 of this Chapter (fluid substitution models) uses sections from this

report, with some revisions and reformatting.

***Gao, L.**, and Morozov, I.B., 2011, AVO analysis of 3-D/3-C datasets form Weyburn CO_2 storage and monitoring project, Proceedings of 2011 CSPG/CSEG/CWLS Convention, p. 1-3 May 2011, Calgary, AB, Canada, http://cseg.ca/assets/files/resources/abstracts/2011/097-AVO_Analysis_of_3D_3C_Datasets.pdf, last accessed 20 Oct 2016*

This paper was modified and expanded and reformatted for this Dissertation. Copyrights for the above publications belong to the authors.

3.1 Models and methods

3.1.1 Fluid substitution model

Quantitative interpretation of reflections from a reservoir undergoing fluid injection depends on the ability to model the effects of pore fluids in the reservoir. The effect of the injected fluid on seismic properties is principally determined by the variations of bulk modulus of the rock. When oil or brine is replaced with CO_2 in the reservoir's pores, the average bulk modulus of the rock changes as described by the so-called fluid substitution model.

Because of several specific properties of CO_2, such as its high compressibility, the fluid substitution model requires utilization of additional theoretical and laboratory results (Batzle and Wang, 1992; Xu, 2006). The fluid substitution model of Wang *et al*. (1998) is based on Gassmann's equation estimating the effect of fluid saturation on the elastic moduli within and near the reservoir. The relation between the bulk modulus of fluid-saturated porous rock (K_{sat}),the porous dry frame (K_{dry}) and matrix (K_{matr}) moduli is:

$$K_{sat} = K_{dry} + K_{matr} \frac{\left(1 - \frac{K_{dry}}{K_{matr}}\right)^2}{(1-\phi) + \phi \frac{K_{matr}}{K_f} - \frac{K_{dry}}{K_{matr}}}, \tag{3.1}$$

where ϕ is the porosity and K_f is the bulk modulus of mixed reservoir fluid. The shear modulus $\mu_{sat} = \mu_{dry}$ is considered to be independent of fluid saturation. Assuming that K_{matr} is constant within the Marly and Vuggy zones, Baharvand Ahmadi et al. (2002) inverted eq. (3.1) to obtain the value of K_{dry} at the current reservoir pressure.

The quality of Gassmann's fluid substitution (3.1) is highly dependent on the accuracy of fluid parameters and physical parameters of reservoir rocks. Laboratory studies and several selections of the most appropriate models are required in order to construct an adequate fluid-substitution model (Morozov and Ma, 2010; Baharvand Ahmadi et al., 2011). Brown (2002) developed a fluid-substitution model and normal-incidence synthetic seismograms for the Weyburn reservoir by using reservoir fluid parameters shown in Table 3.1. However, more recently, Xu (2006) modified these equations to provide more accurate estimates of the CO_2 properties (Figure 3.1). Note the significant difference in the bulk moduli predicted by these methods, Baharvand Ahmadi et al. (2011) extended this analysis to oblique incidence and focused on the fluid-substitution effects on AVA attributes during CO_2 flooding. The main question in this Chapter is whether and how pressure and CO_2- saturation effects can be separated in AVA intercept-gradient measurements.

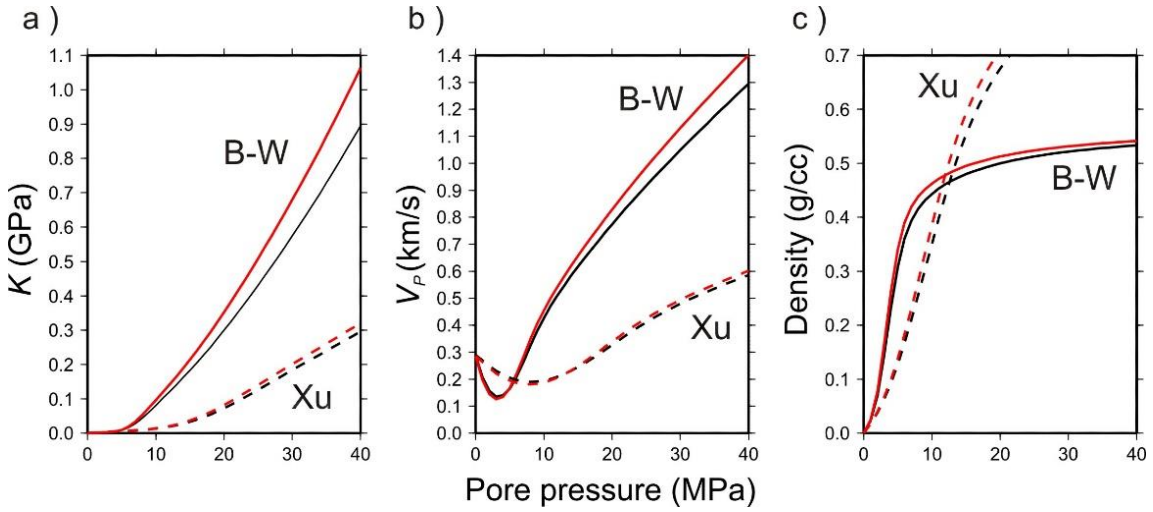

Figure 3.1. CO_2 properties calculated by using Xu's equations (dashed lines), and by using Batzle-Wang's equation (B-W: solid lines). Red lines are for temperature 56°C, black – for 63°C. (From Baharvand Ahmadi et al., 2011)

Further, Brown (2002) approximated the pressure-dependence of the bulk and shear moduli of the dry rock the Midale zones from the results of ultrasonic lab testing. Differential-pressure related trends $K_{dry}(p)$ and $\mu_{dry}(p)$ were measured under confining pressure 23 MPa and pore pressure 15 MPa (Brown, 2002). This confining pressure of 23 MPa was taken as the average of the vertical stress of 32–33 MPa and horizontal stress of 18–22 MPa. Brown (2002) derived a polynomial increase of K_{dry} with differential pressure, which we denote $K_B(p)$, and a similar dependence for μ_{dry}. Denoting the *in situ* differential pressure at baseline conditions as p_0, the pressure-corrected dry bulk modulus then is

$$K_{dry}(z, p) = K_{dry}(z) + K_B(p) - K_B(p_0), \tag{3.2}$$

and a similar equation for the shear modulus. Here, K^*_{dry} is estimated from eq. (3.1), p is the differential pressure. In our calculations (Baharvand Ahmadi et al., 2011), we took

the vertical stress of 32.5 MPa as the confining pressure, which allowed relating the differential pressure in eq. (3.2) to pore pressure in fluid-substitution estimates.

The key part of the model was in using the Gassmann's equation to estimate the matrix (K_{matr}) and dry (K_{dry}) moduli of the reservoir and the surrounding host rocks. To achieve a meaningful solution, we first assumed that K_{matr} was constant within each unit, and then applied corrections for volume fractions of clay in it. Further, the observed K was derived at each depth level from the seismic logs and density as $K = \rho\left(V_P^2 - \frac{4}{3}V_S^2\right)$, and K_{dry} was inverted from this value by using the Gassmann's equation (3.1). Several constraints were imposed to guarantee physically meaningful results (such as positive porosity, $K_{dry} < K_{matr}$, and other).

Porosity ϕ is an important parameter of eq. (3.1) that needs to be carefully measured. Total rock porosity includes isolated pores and the volume occupied by clay-bound water. These volumes cannot be filled by the injected CO_2 and water. By contrast, effective porosity represents the interconnected pore volume into which fluid substitution can occur, and therefore it (and not the total porosity) should be used as parameter ϕ in eq. (3.1). Because the effective porosity is lower than total porosity, its use leads to smaller changes in the elastic parameters. Therefore, time-lapse velocity, travel-time, and reflectivity variations estimated by using the effective porosity should be smaller than those derived from total porosity.

Further, because the values of the in situ K_{matr} are poorly known, Baharvand Ahmadi et al. (2011) tried estimating them by using an optimization procedure. It was noted that rewriting the Gassmann's equation (3.1) in terms of compressibility, K_{dry}^{-1} becomes a

linear function of ϕ. Therefore, in each of the two (Marly and Vuggy) units, K_{matr} was adjusted so that the dependence of K_{dry}^{-1} on the effective porosity was closest to linearity (Figure 3.2). Finally, to adjust the log to any point within the study area, we stretched and shifted the obtained synthetic logs so that the reflections from the top of Marly and bottom of Vuggy corresponded to the markers observed in the stacked seismic sections.

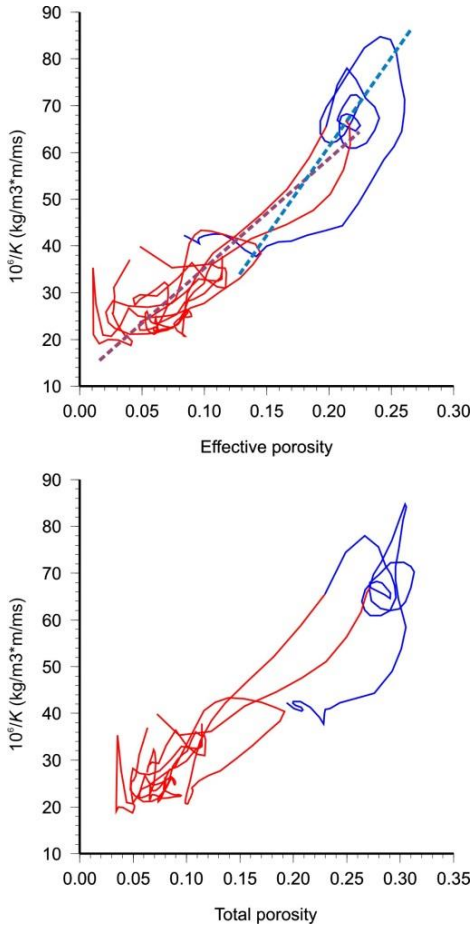

Figure 3.2. Cross-plots of $106/K_{dry}$ in optimal model versus the total and effective porosity for Marly (blue) and Vuggy (red) units. Dashed lines indicate the optimized trends of K_{dry}^{-1}(effective porosity). (From Baharvand Ahmadi et al., 2011).

From the edited and inverted logs (Baharvand Ahmadi et al., 2012), it now became possible to simulate realistic seismic AVA responses from Weyburn reservoir.

Table 3.1. Reservoir parameters

Parameters	Baseline	Monitor
Temperature	63°C	56°C (52–58°C)
Oil API gravity	29 (25~34)	29 (25~34)
Gas gravity	1.22	unchanged
CO_2 gravity	1.5249	unchanged
Gas/Oil ratio (GOR)	30 L/L	unchanged
Salinity	85,000 ppm NaCl	79,000 ppm NaCl
Water resistivity	0.149 ± 0.023 (ohm m)	0.104 ± 0.014 (ohm m)
Oil saturation in Marly zone	Average 53%	Average 30%
Oil saturation in Vuggy zone	Average 35%	Average 28%
Pore pressure	15 MPa	23 MPa near injector 8 MPa near producer
Confining pressure	32~33 MPa	unchanged
Mineral bulk modulus (Brown, 2002)	83 GPa (Marly zone) 72 GPa (Vuggy zone)	unchanged
Mineral shear bulk modulus (Brown, 2002)	48 GPa (Marly zone) 33.5 GPa (Vuggy zone)	unchanged
Clay (shale) moduli	21 GPa (bulk) 7 GPa (shear)	unchanged

3.1.2 AVO attributes

The AVA/AVO is a group of techniques by which geophysicists attempt to determine the porosity, density, velocity, lithology and fluid/gas content of in situ rocks by looking at the variations of P-wave reflectivity with variable source-receiver offsets. The AVO analysis could investigate the S-wave properties and image S-wave on horizontal component. In addition, there is no S-wave source for acquisition which make

AVO to be the most promising technique for S-wave study. The relationship between the offset (incidence angle) and reflection/transmission amplitudes at an impedance interface is descrbed by the Zoeppritz equations (Zoeppritz, 1919). For an incident P wave (Figure 3.3), the amplitude variations of these amplitudes with incidence angle can be obtained from the following matrix inverse (Aki and Richards, 2002):

$$\begin{bmatrix} R_{\mathrm{P}} \\ R_{\mathrm{S}} \\ T_{\mathrm{P}} \\ T_{\mathrm{S}} \end{bmatrix} = \begin{bmatrix} -\sin\theta_1 & -\cos\phi_1 & \sin\theta_2 & \cos\phi_2 \\ \cos\theta_1 & -\sin\phi_1 & \cos\theta_2 & -\sin\phi_2 \\ \sin 2\theta_1 & \frac{V_{\mathrm{P1}}}{V_{\mathrm{S1}}}\cos 2\phi_1 & \frac{\rho_2 V_{\mathrm{S2}}^2 V_{\mathrm{P1}}}{\rho_1 V_{\mathrm{S1}}^2 V_{\mathrm{P2}}}\cos 2\phi_1 & \frac{\rho_2 V_{\mathrm{S2}} V_{\mathrm{P1}}}{\rho_1 V_{\mathrm{S1}}^2}\cos 2\phi_2 \\ -\cos 2\phi_1 & \frac{V_{\mathrm{S1}}}{V_{\mathrm{P1}}}\sin 2\phi_1 & \frac{\rho_2 V_{P2}}{\rho_1 V_{P1}}\cos 2\phi_2 & \frac{\rho_2 V_{S2}}{\rho_1 V_{P1}}\sin 2\phi_2 \end{bmatrix}^{-1} \begin{bmatrix} \sin\theta_1 \\ \cos\theta_1 \\ \sin 2\theta_1 \\ \cos 2\phi_1 \end{bmatrix} \quad (3.3)$$

where R_{P} and R_{S} is the reflected amplitude of P and S-waves and T_{P} and T_{S} is the transmitted amplitudes of P and S waves, respectively,

Figure 3.3 further explains the notation used in eq. (3.3).

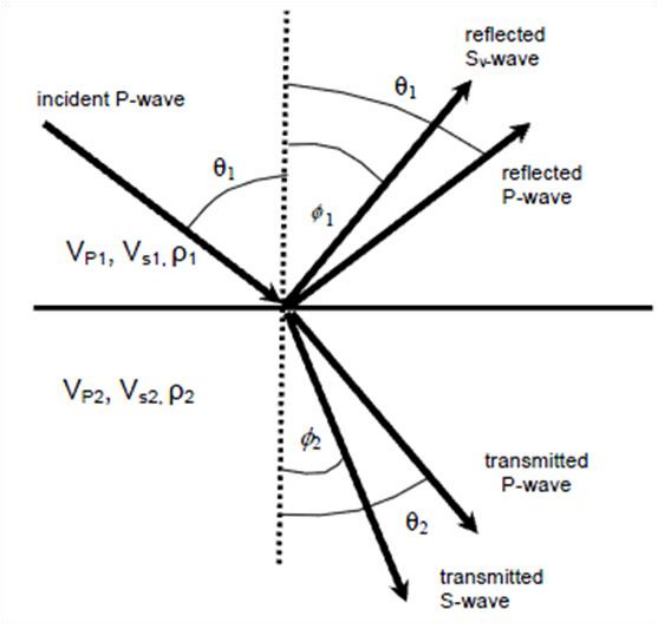

Figure 3.3. P-wave mode conversion at a planar interface

Based on the general matrix expression (3.3), several types of simplified AVO equations were established for practical use in interpretation (Bortfeld, 1961; Aki and Richards, 1980; Shuey, 1985). The well-known Aki and Richards' approximation assumes small contrasts of the P-wave, S-wave velocities and density across an interface and predicts the dependence of the P-P reflection coefficient, *R*, on the incidence angle, θ, as a linear combination of the contributions from the relative contrasts in these physical properties:

$$R(\theta) = a\frac{\Delta V_P}{V_P} + b\frac{\Delta V_S}{V_S} + c\frac{\Delta \rho}{\rho}, \tag{3.4}$$

$$\text{where: } a = \frac{1+\tan^2\theta}{2}, \tag{3.5}$$

$$b = 0.5 - \left(\frac{V_S}{V_P}\right)^2 \sin^2\theta, \tag{3.6}$$

$$\text{and } c = 4\left(\frac{V_S}{V_P}\right)^2 \sin^2\theta. \tag{3.7}$$

Equation (3.4) can also be rearranged by isolating the different forms of dependences on the incidence angle (Russell, 1988):

$$\begin{aligned} R(\theta) = {} & \frac{1}{2}\left(\frac{\Delta V_P}{V_P} + \frac{\Delta \rho}{\rho}\right) \\ & + \left(\frac{1}{2}\frac{\Delta V_P}{V_P} - 4\frac{V_S^2}{V_P^2}\frac{\Delta V_S}{V_S} - 2\frac{V_S^2}{V_P^2}\frac{\Delta \rho}{\rho}\right)\sin^2\theta \\ & + \frac{1}{2}\frac{\Delta V_P}{V_P}\left(\tan^2\theta - \sin^2\theta\right). \end{aligned} \tag{3.8}$$

In this equation, the first term is zero-offset reflectivity dependent on P-wave velocity and density. The second term is sensitive to the contrasts in P- and S-wave velocities and density.

Shuey (1985) proposed another popular representation of these relations in terms of the variations of the Poisson's ratio and density across the boundary:

$$R(\theta) = R_0 + \left(A_0 R_0 + \frac{\Delta\sigma}{(1-\sigma)^2} \right) \sin^2\theta + \frac{1}{2}\frac{\Delta V_P}{V_P}\left(\tan^2\theta - \sin^2\theta\right), \tag{3.9}$$

where:

$$R_0 = \frac{1}{2}\left(\frac{\Delta V_P}{V_P} + \frac{\Delta\rho}{\rho} \right), \tag{3.10}$$

$$A_0 = B - 2(1+B)\frac{1-2\sigma}{1-\sigma}, \tag{3.11}$$

$$B = \frac{\Delta V_P / V_P}{\Delta V_P / V_P + \Delta\rho / \rho}. \tag{3.12}$$

In Aki and Richards' and Shuey's approximations (3.4) and (3.9), the third terms are nonlinear with respect to $\sin^2\theta$ (these terms are often called "curvature"). These terms are often difficult to measure and dropped during practical data analysis. For incident angles θ below about 30°, the reflected amplitude $R(\theta)$ is close to a linear function of $\sin^2\theta$. This allows defining the concepts of AVO intercept (I) and gradient (G) through the following relation:

$$R(\theta) = I + G\sin^2\theta, \tag{3.13}$$

and the AVO dependence in this angle range is called "linear".

From equation (3.13), the intercept I gives an accurate value (more accurate than the conventional stack) of the normal-incidence P-wave reflectivity:

$$R_P(0) = I. \tag{3.14}$$

The relative values of I and G serve as the principal keys to AVO classification. Figure 3.4 shows four resulting AVO classes and an (I, G) crossplot based on Castagna's et al. (1998) and Rutherford-Williams classifications (1989).

Class I: High-impedance contrast with decreasing AVO;

Class II: Near-zero impedance;

Class IIp: Near-zero impedance with polarity change;

Class III: Low impedance with increasing AVO;

Class IV: Low impedance with decreasing AVO.

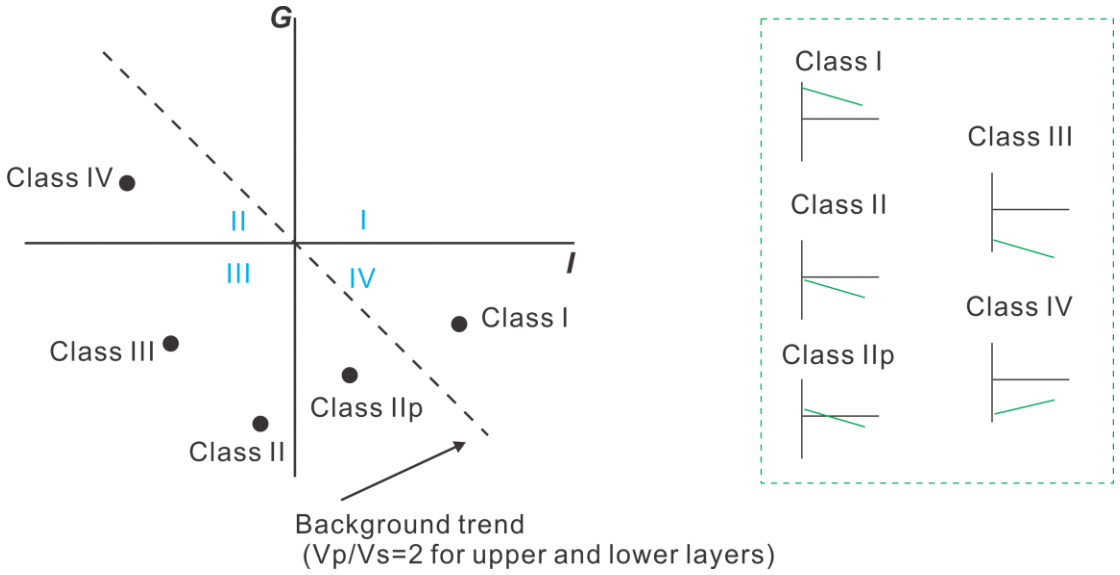

Figure 3.4. AVO cross-plot showing the AVO classes. Inset schematically shows the dependences of reflection amplitude, R, on $\sin^2\theta$ for different AVO classes.

Based on the values of I and G, several additional useful AVO attributes can be constructed. In particular, by approximating the "background" velocity ratio as $V_P/V_S = 2$, the S-wave reflectivity at normal incidence can be derived as a combination of I and G (Rutherford and Williams, 1989):

$$R_S(0) \approx \frac{1}{2}(I - G). \tag{3.15}$$

This attribute is used in the interpretation of time-lapse seismic data in Section 3.2. Another key pair of derivative attributes developed for Weyburn 3-C/3-D datasets (Baharvand Ahmadi et al., 2011) and used is based on projecting the observed values of (I, G) onto an empirical trend observed in the data, analogously to the "mud line" in Figure 3.4. These attributes will also be used in Section 3.2. Treating the statistical scatter in my AVO measurements empirically, I construct a pair of normalized deviations ("principal components") of (I, G) along and across this interpreted trend line (Figure 3.5):

$$\delta P_1 = \frac{G_0 - G_C}{|I_C|\cos\phi}, \text{ and } \delta P_2 = \frac{I - I_0}{|I_C|\cos\phi}, \tag{3.16}$$

where (I, G) is the measured AVO point, (I_0, G_0) is its projection onto the trend, and (I_C, G_C) is the center of the distribution of all (I, G) points. As shown in the following section, the attribute δP_1 should be most sensitive to the variations of CO_2 saturation within the reservoir, and the variations of δP_2 should mostly be due to variable pore

pressure.

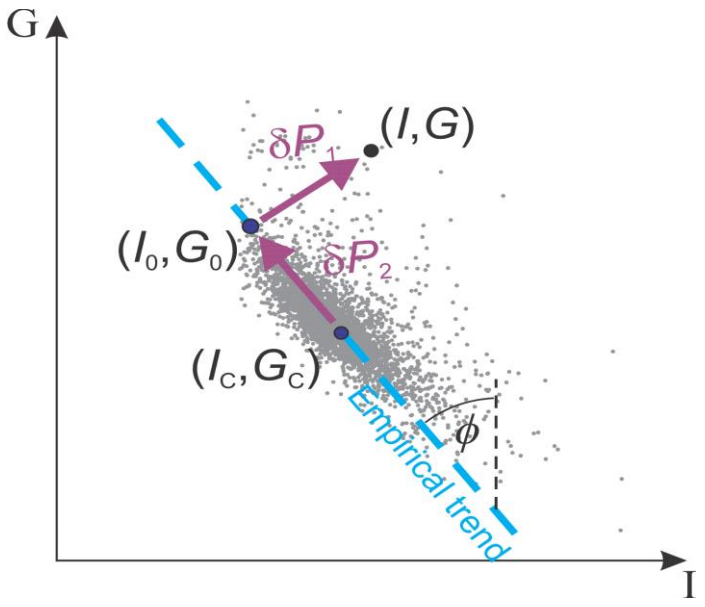

Figure 3.5. Empirical proxy attributes derived from reflections in the baseline Weyburn 3-C/3-D dataset (grey dots). The scatter of observations delineate an empirical trend (dashed cyan line). The new attributes emphasize the deviations of AVO parameters along (δP_1) and across the trend line (δP_2). (From Baharvand Ahmadi et al., 2011).

3.1.3 Modeling of AVO effects for Weyburn reservoir

The association of the empirical trend (dashed cyan line in Figure 3.5) with pressure variations of injection fluids within the reservoir was based on modeling the effects of fluid substitution on AVO responses of the reservoir (Baharvand Ahmadi et al., 2011). A significant difficulty of this modeling consists in the low thickness of the Weyburn reservoir, which is below the dominant wavelength. Therefore, the reflections from the caprock and top and bottoms of the Marly and Vuggy zones overlap, leading to overlapping and frequency-dependent AVO responses. A detailed modeling of AVO attributes using the detailed reservoir structure was conducted by Morozov and Ma (2010)

and in our Weyburn project report (Baharvand Ahmadi et al., 2011). The fluid-substitution model was incorporated in a layered structure based on well-log measurements made at 0.5-foot intervals throughout the entire zone of interest. This allowed detailed calculation of the reservoir response to the finite-bandwidth seismic wavelet. While using the exact expressions (3.3) for modeling reflection responses, the traditional intercept (*I*) and gradient (*G*) attributes were utilized for interpreting the results and comparing them to the reflection 3-C/3-D data.

To produce the AVA synthetics, Morozov and Ma (2010) and Baharvand Ahmadi et al. (2011) derived the oblique-incidence reflectivity for each ray parameter of the incident wave by using the exact expressions (3.3) for reflection and mode conversion amplitudes. This resulted in "synthetic logs" of reflection amplitudes. Next, these "logs" were converted into the two-way reflection travel-time domain and convolved with the selected 50-Hz zero-phase Ricker wavelet. Finally, three-term AVA analysis was performed on these synthetics, producing additional "logs" of *I*, *G*, and "AVA curvature" values. As expected, curvature values were insignificant within the offset (ray parameter) range of this study. Figure 3.6 shows such a wavelet-filtered AVA synthetic for the same (unstretched) well.

The AVA intercept and gradient values were measured from ray-tracing synthetics over a range of incidence angles from 0 to 30°. Depth-to-time conversion of well logs was performed at all individual depth log readings, which allowed bypassing typical problems related to log and seismic record resampling. In the following, AVA attributes and CO_2 discriminator are estimated by using different approaches, and a simple CO_2-saturation – pore-pressure discriminator is proposed and tested.

Table 3.2. Parameters of two-layer AVO models

Type of rock	V_P(m/s)	V_S(m/s)	Density (g/cc)	Total porosity	Effective porosity
Anhydrite	5900.0	3250.0	2.90	0	0
Marly dolomite	3600.0	2000.0	2.31	0.29	0.20
Vuggy limestone	5100.0	2900.0	2.56	0.10	0.10

Another important difference of Weyburn reservoir from the simplified AVO models considered in the preceding section is in large reflectivity values that do not accurately satisfy the conventional small-contrast approximation. Figure 3.7 compares the accuracy of small-contrast computations obtained by using Shuey's equation to the exact solution in two-layered models corresponding to the ranges of elastic parameters encountered in the reservoir (Baharvand Ahmadi et al., 2011). The first of these models (Table 3.2) represents an anhydrite/Marly interface, which is the upper boundary of the reservoir. For larger ray parameters, there are about 10% differences in the reflectivities, which correspond to almost double AVO gradients in the exact solution (Figure 3.7). Considering that the Marly zone is relatively thin compared to the dominant wavelength (Figure 3.6), the second end-member model was constructed by removing the Marly zone and placing the anhydrite layer directly above the Vuggy zone (Table 3.2).

The strong difference in AVO gradients (Figure 3.7) shows that Shuey's approximation would lead to incorrect representation of the AVO responses. Therefore, the full Zoeppritz reflectivity equations (such as eq. (3.3)) were used for accurate modeling (Baharvand Ahmadi et al,. 2011). Using the resulting synthetic seismograms,

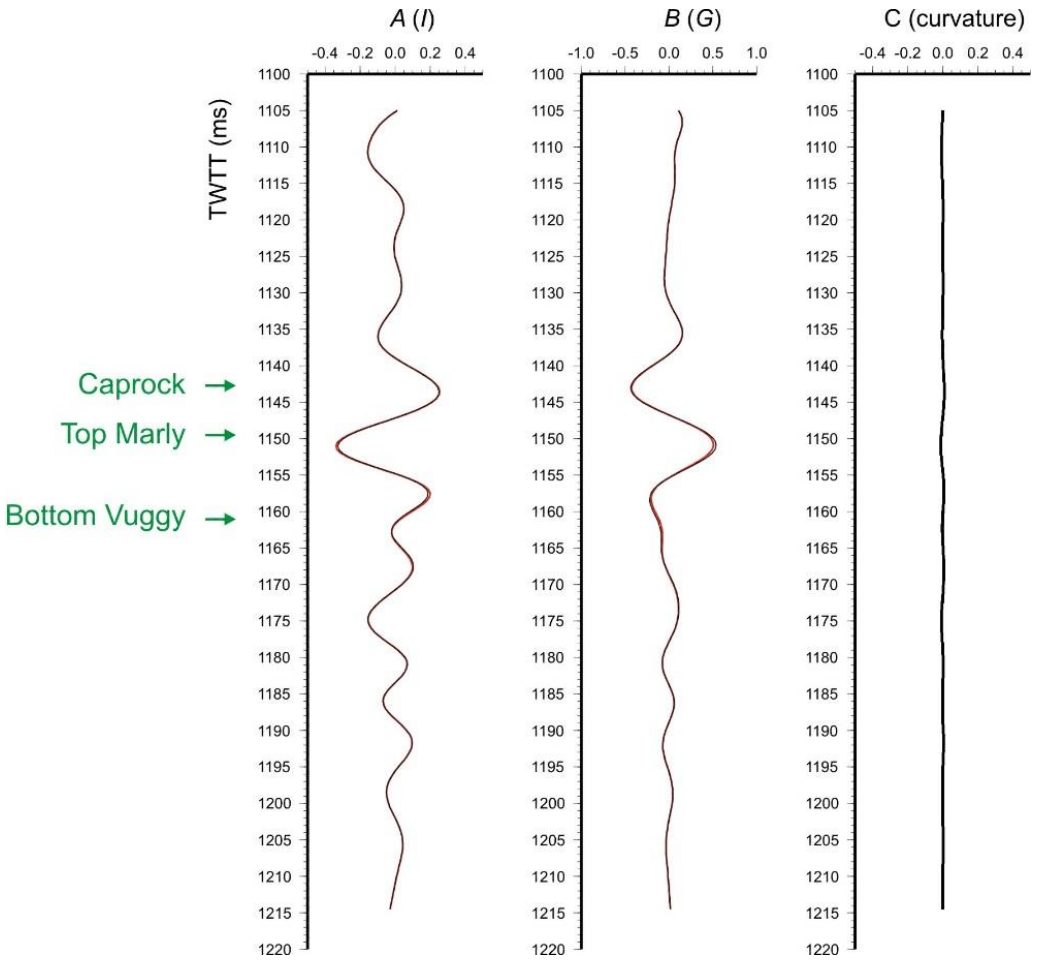

Figure 3.6. Three-term 50-Hz Ricker-wavelet AVA synthetics derived from logs within the study area (Baharvand Ahmadi et al., 2011). *A* is the intercept (denoted *I* in this Dissertation), *B* is the gradient (*G*), and *C* is the third AVA term (curvature), plotted using comparable amplitude scales. Black curve corresponds to brine only, and red curve – to brine with 20% CO_2 within the reservoir. At 1150 ms, the differences between these curves are about 6%. Note that the absolute values of *G* are about twice those of *I*, and that the curvature effect is small. (From Baharvand Ahmadi et al., 2011).

the intercept (*I*) and gradient (*G*) parameters were further extracted for interpreting the AVO anomalies. The exact solutions are near-linear with respect to ray parameter and show no significant curvature terms (Figure 3.7). Consequently, my analysis of the time-lapse data was based on the attributes *I* and *G*, as well as their derivative attributes

described in the preceding section.

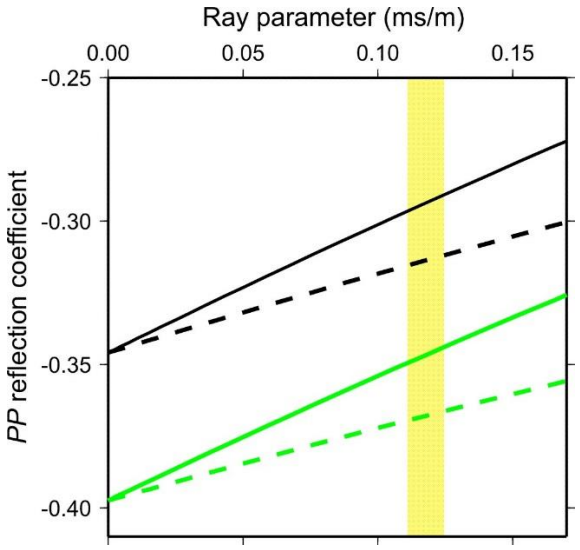

Figure 3.7. AVA curves in anhydrite/Marly model (Table 3.2 by using the exact solution (solid lines) and Shuey's approximation (dashed lines) (Baharvand Ahmadi et al., 2011). Black lines correspond to a mixture of 30% oil and 70% water, green lines – for 18% oil, 72% water, and 10% CO_2. Yellow bar shows the upper limit of ray parameter-values for reflections from Weyburn reservoir. (From Baharvand Ahmadi et al., 2011)

3.1.3 Effects of CO_2 pressure and saturation on reflection AVO

AVA attributes in models with realistic depth variations of reflectivity can be significantly different from those of the conventional two-layered models (Figure 3.7) Interestingly, in the AVA cross-plots, the (*I*,*G*) points computed by using the realistic depth-dependent parameters (eq. 1) are located between those of the anhydrite/Marly and anhydrite/Vuggy end-member models (Figure 3.8a). This effect occurs because of the half-length of the incident wavelet (~50 m at 40 Hz) exceeding the thickness of the reservoir, and particularly of its Marly zone. When the dominant frequency of the wavelet is increased, a separate reflection from the anhydrite/Marly contact becomes

observed, and therefore the (*I*,*G*) values approach those of the anhydrite/Marly model. Conversely, when the dominant frequency of the wavelet is decreased, the reflectivity from Marly zone becomes relatively insignificant, and the (*I*,*G*) response approaches that of the anhydrite/Vuggy model (Figure 3.7).

By using the well-log based models, Baharvand Ahmadi et al. (2011) simulated fluid saturations ranging from 100% water to 100% oil and to 100% CO_2. In the example presented here (Figure 3.7), the saturation of CO_2 (denoted S_{CO2}) in the mixture was varied from 0 to 100%, and the relative saturations of oil and water were maintained at the ratio of 1:4. This allowed examining the effect of CO_2, which is dominant compared to the relative composition of the liquid oil/water mixture. Pore pressures were varied from 7 to 23 MPa, which corresponded to the estimated variation of the pressure from the production to injection wells (Figure 3.8).

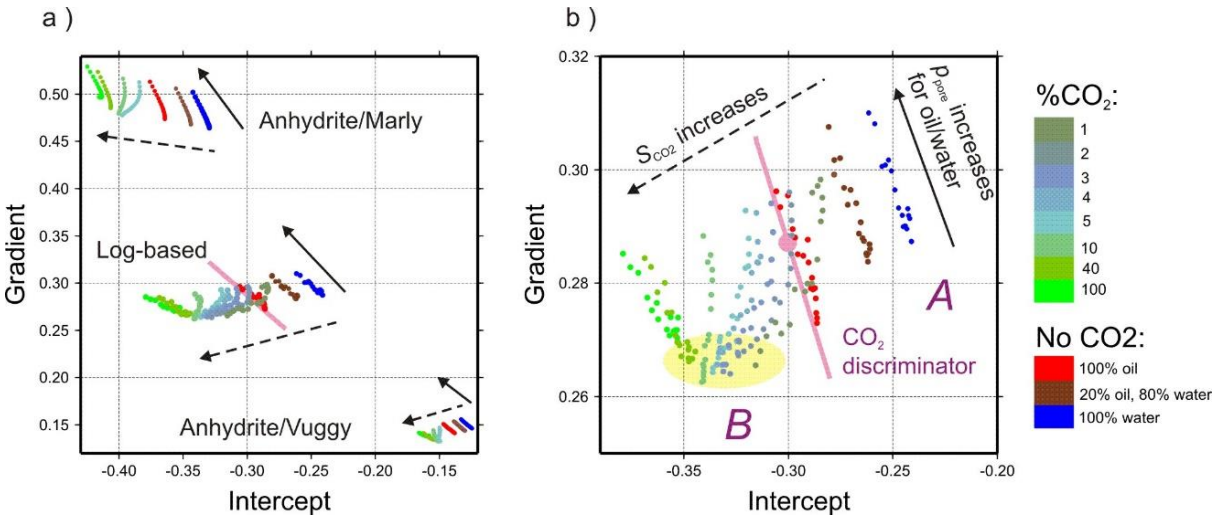

Figure 3.8. Modelled AVO cross-plots: a) from two-layered models and well-log based models; b) details of the well-log model. Solid and dashed arrows indicate the pore pressure and CO_2 saturation increasing direction respectively. Yellow ellipse indicates the area of (*I*, *G*) values converging at low pore pressure. Pink lines and large dot show the CO_2 discriminator. (From Baharvand Ahmadi et al., 2011).

When fluids contain even small amounts of CO_2, their bulk moduli are strongly affected by the pore pressure (subsection 3.1.1). For relatively low pore pressures (about 7 MPa) and s_{CO2} changing from 0 to 1%, the (*I*,*G*) values of the reservoir rapidly move into the area indicated by the yellow ellipse in Figure 3.8b. Note that the amount of this shift is comparable to the total distance between the 100%-oil and 100%-water cases (Figure 3.8b). From this area, (*I*,*G*) values move with increasing pressure in a fan-like pattern, generally opposite to the general CO_2-saturation trend for $S_{CO2} \approx 1– 5\%$ (*i.e.*, to the dashed arrow in Figure 3.8b) and in the direction of the oil/water pore-pressure trend when $S_{CO2} \approx 10–100\%$ (solid arrow). By contrast, changes in the oil/water mixture cause sub-parallel (*I*,*G*) trends that are consistently different from those caused by pore-pressure variations (brown and blue circles in Figure 3.8b).

Ma and Morozov (2010) built the AVO model in terms of two-layer model and well-log measurements by considering the thin and high-contrast Weyburn reservoir. The fluid saturation ranges from 100% water to 100% oil and to 100% CO_2. The saturation of CO_2 in the mixture was varied from 0 to 100% and the relative saturation of oil and water were maintained at the ratio of 1:4. The pore pressure could be strongly influenced when small amount of CO_2 is contained. Figure 3.8 shows the modelled AVO cross-plots (Ma and Morozov 2010).

As mentioned above, AVO technique could yield a most valuable discriminator (Gao and Morozov, 2011) to measure pore-pressure and saturation effects due to CO_2 injection. The AVO modeling is based on the properties of the primary P/P reflection. Similarly, the same conclusions also apply to the amplitude of S-wave reflection. On the

basis of fluid substitution modelling of the reservoir, $I - G$ and $I+G$ should be sensitive to pore-pressure and CO_2 saturation respectively. The time-lapse AVO attributes indicate areas of pore-pressure and potentially CO_2 saturation variations between the horizontal injection wells. The results indicate that the AVO method allows estimating reservoir pressure and fluid saturation variations from time-lapse. Assuming that the trend is due to the variations of pore pressure within the reservoir, positive values of δP_1 and δP_2 correspond to the directions of increasing pressure and decreasing CO_2 saturation, respectively.

3.1.4 Acoustic impedance

The acoustic impedance (AI), denoted Z here, is among the primary tools for extracting lithological information from reflection seismic data. In practical applications, the AI is defined is the product of density and seismic velocity:

$$Z = \rho V \, . \tag{3.17}$$

At a reflection boundary, this property undergoes a sharp contrast. The resulting reflectivity is a function of the ratio of impedances Z_1 and Z_2 of the upper and lower layers:

$$r_{12} = \frac{Z_2 - Z_1}{Z_2 + Z_1} = \frac{Z_2 / Z_1 - 1}{Z_2 / Z_1 + 1} \, . \tag{3.18}$$

For small impedance contrasts, eq. (3.18) can be approximated as:

$$r_{12} = \frac{\Delta Z}{2Z} = \frac{1}{2} \Delta \ln Z \, , \tag{3.19}$$

where $\Delta Z = Z_2 - Z_1$ indicates the impedance contrast at the boundary. At any depth level or reflection time t_i within a seismic trace, the impedance can therefore be derived from the reflectivity series by summation:

$$Z_i = Z_0 \exp\left(2\sum_{j=1}^{i} r_{i-1,i} \right). \tag{3.20}$$

In seismic inversion software, eq. (3.20) is usually used to evaluate $Z(t)$ recursively, starting from small values of time t and proceeding to larger times. However, due to discrete sampling, limited bandwidth of seismic records and data noise, an unconstrained, slowly-varying multiplicative factor is always present in the impedance values evaluated by eq. (3.20). This unconstrained scaling results in instabilities when comparing the impedance between the baseline and monitoring vintages of a time-lapse dataset.

In order to resolve this problem of slowly-drifting and unconstrained scaling, in the next section, I equalize the relative impedance variations measured between the target and reference horizons (above the caprock), and also between the monitor and baseline datasets. Let use denote the two reflectivities picked at the caprock in the baseline and monitor datasets by R_C^{Base} and R_C^{Mon}, and the reflectivities from the top of Marly by R_M^{Base} and R_M^{Mon} respectively. Then, taking the AI for the reference level $Z_0 = 1$, the scaled variation of AI below Marly reflector equals:

$$\frac{1}{2}\frac{\Delta \ln Z^D}{R_{ref}^D} = \frac{R_C^D + R_M^D}{R_{ref}^D}, \tag{3.21}$$

Where superscripts '^{D}' denote either the baseline (with $D = Base$) or monitor ($D = Mon$)

datasets, and $R_{ref}^{D} > 0$ is the calibration amplitude picked at the reference horizon. When monitoring time-lapse impedance variations, I subtract eqs. (3.21) for the monitor and baseline datasets and thus obtain a scale-invariant, impedance-type time-lapse attribute:

$$\frac{1}{2}\Delta \ln \zeta \equiv \left(\frac{\Delta \ln Z^{Mon}}{R_{ref}^{Mon}} - \frac{\Delta \ln Z^{Base}}{R_{ref}^{Base}} \right) = \frac{R_C^{Mon} + R_M^{Mon}}{R_{ref}^{Mon}} - \frac{R_C^{Base} + R_M^{Base}}{R_{ref}^{Base}}. \qquad (3.22)$$

This scaled impedance variation should equal zero when the impedance is unchanged between the baseline and monitoring datasets. This quantity is also insensitive to any residual variations in the amplitude of reflectivity at the reference horizon.

3.2 Time, amplitude, AVO and acoustic-impedance variations

The reflection amplitude measurements in this section are focused on two reflectors: 1) the reservoir caprock, which is a strong, consistent and positive-polarity reflector, and 2) the interpreted Marly horizon, which is a thin reflection of negative polarity immediately beneath the caprock (Figure 3.9). Due to Marly rock having high permeability, the dominant fluid effect caused by CO_2 flow is expected to occur at this level. However, considering that the thickness of Marly is below or comparable to one quarter of the seismic wavelength, it is also possible that the caprock reflection is also affected by fluid-related reflectivity changes within the Marly.

To compare the three vintages of seismic data, the stacked amplitudes must be equalized further since the pre-stack calibration described above appears to be still insufficient. This equalization will apply to the conventional stacked P-wave amplitudes and AVO attributes, such as intercept, gradient, or S-wave reflectivity. The following procedure was applied for this calibration:

a) Picking of reference horizons above the caprock. The horizons were selected according to their continuity, consistency and strong reflection.

b) Amplitude measurement on the picked reference horizons.

Three horizons were chosen to meet the sensitivity requirement (Figure 3.9): horizon R1 representing a negative-polarity reflection at ~750 ms two-way travel time, R2 representing positive reflection near ~1050 ms (Lower Shaunavon Formation, denoted Lshaun), and R3 containing a negative reflection immediately above the positive caprock reflection (Figure 3.10). I assumed that these reference horizons would not be significantly affected by the injection and used their amplitudes for normalizing the amplitude and AVO parameters (*I* and *G*). The following ratio was formed for any attributes that were proportional to the recorded amplitudes:

$$\tilde{A} = \left(\frac{A_{\text{monitor}}}{R_{\text{monitor}}} \right) \Big/ \left(\frac{A_{\text{baseline}}}{R_{\text{baseline}}} \right), \tag{3.23}$$

where A is the attribute being calibrated and taken for either the baseline or the appropriate monitor dataset, and R is the stacked amplitude at the reference horizon (also taken in the corresponding dataset). Both A and R are typically measured as the root-mean square (R.M.S.) values of the samples between the two zero crossings adjacent to the picked reflection event (green lines in Figure 3.9). The resulting dimensionless quantity (3.23) is independent of amplitude scaling in each of the datasets, and it equals one when no variations relative to the baseline is observed.

In the following subsections, I report the results for the reflection-time differences, scaled amplitudes, AVO attributes, and acoustic-impedance anomalies observed by applying the above procedures to the time-lapse datasets.

3.2.1 Time-difference variations

Before measuring the amplitude and AVO attributes, I examined the differences in the two-way travel times for several horizons. The time differences between the monitor (2001 or 2002) and baseline (1999) datasets were measured by computing cross-correlations of the stacked waveforms within narrow time windows (20 ms) and picking their maxima. The travel-time deviation of the reflection is expected within one sampling interval. Figure 3.11 shows a map of the variation for the reference reflector R1 (Figure 3.9). Time differences between the reflectors are even smaller, generally within ±0.5ms which is interpolated within the study area (Figure 3.12). Figure 3.12 shows some correlation of the positive differential travel-times for the caprock reflector with the positions of injector wells, particularly for 2002 monitor in the southeastern part of the survey area. The average velocity in these areas should reduce by about 0.05% if there is of about 0.25-ms time delay. From this observation, it is possible that some of the CO_2 penetrates the caprock. Taking a ~2% P-wave velocity reduction as an estimate for the effect of CO_2, this would mean that at 10–12-m above the reservoir might be affected by the CO_2 in the areas shown by pink colour in Figure 3.11. According to Prof. Chris Hawkes (personal communication), during the early CO_2 injection, the caprock was not sealed, and the capture of CO_2 was performed at the Watrous formation at the depth of approximately 1401 m. A zone of CO_2 above the reservoir might also be indicated by an amplitude anomaly in a P-wave reflection dataset (White, 2013).

Figure 3.13 shows the change in the reflection-time interval between the caprock and Bakken (about 150 ms below the reservoir). The two-way travel time variation is ~1 ms, and positive time anomalies are correlated with the injection wells, particularly for 2002 monitor in the SE part of the survey area (Figure 3.13). Taking an about 5% P-wave velocity reduction as an estimate for the effect of CO_2, this would mean that 20 to 30 meters below the caprock might be affected by the CO_2 after two years of injection, in the areas shown by red colour in Figure 3.13.

3.2.2 Time-lapse amplitude anomalies

Since the time-difference shows the possible CO_2 impact on caprock level, it is worthwhile to examine the amplitude of not only for reservoir but also for the caprock. For the caprock reflector, stacked reflection amplitudes for the two monitor datasets according to eq. (3.23) are shown in Figure 3.14. To verify whether these variations depend on the choice of the reference reflectors, I created similar maps by using other reference horizons. Figure 3.15 shows such a map using the reference reflector R1. With both types of normalization, the resulting amplitude maps show similar variations, which appear to have no clear correlation with injection wells (Figure 3.14).

A similarly scaled Marly reflection (Figure 3.16) shows a somewhat better correlation of the amplitude anomalies with injection wells. The patterns of anomalies appear to be better aligned with the injection wells, along which we observe a relative increase in reflection amplitudes. These anomalies also appear to generally strengthen with increasing injection time (Figure 3.16).

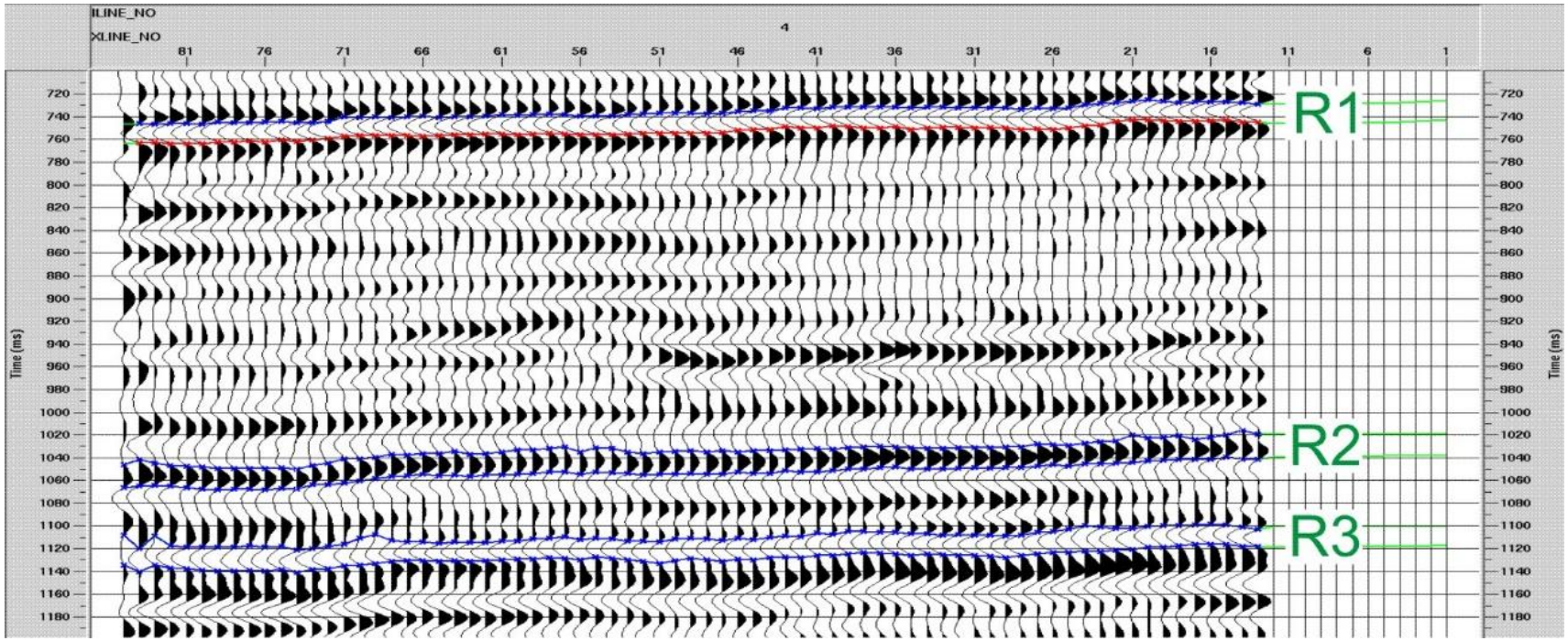

Figure 3.9. Reference horizons (green labels) used for calibration of reflection and AVA responses.

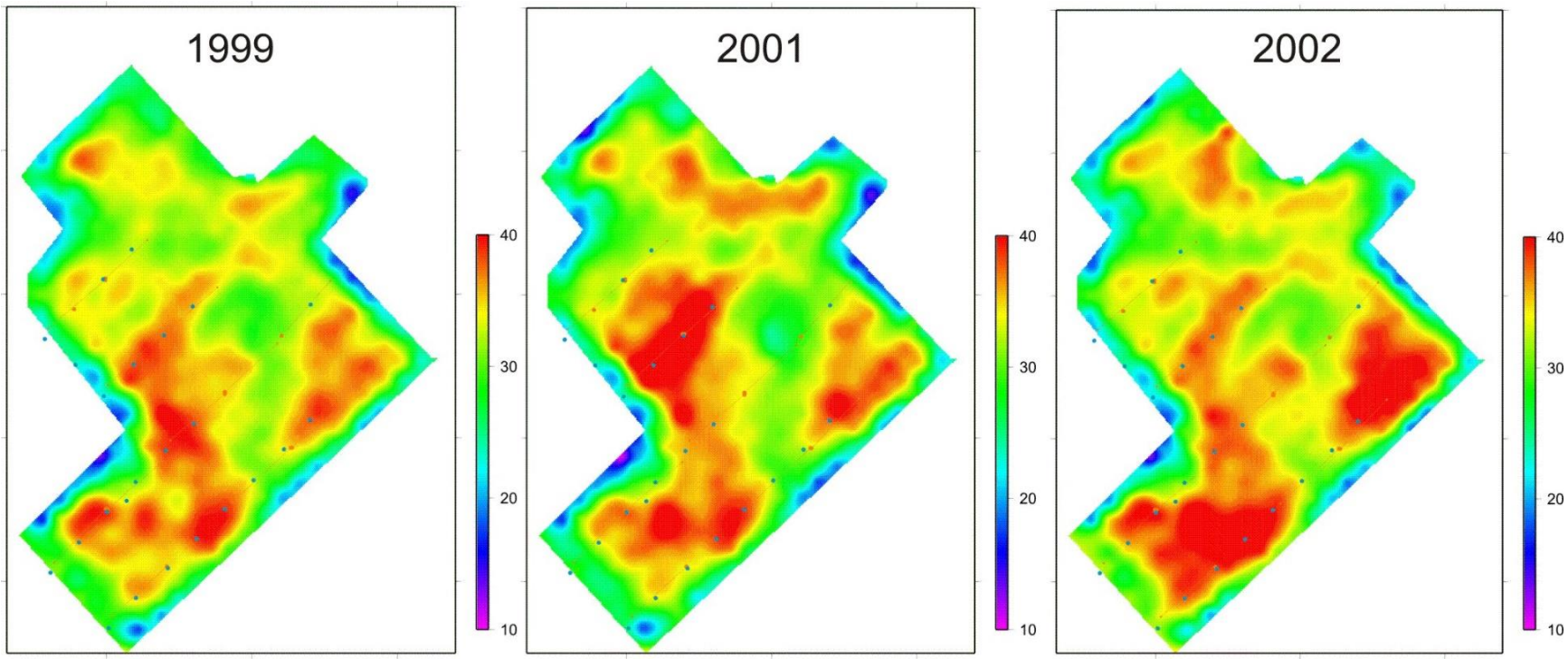

Figure 3.10. R.M.S. reflection amplitude at reference horizon R3. The amplitudes are shown in relative units resulting from seismic processing.

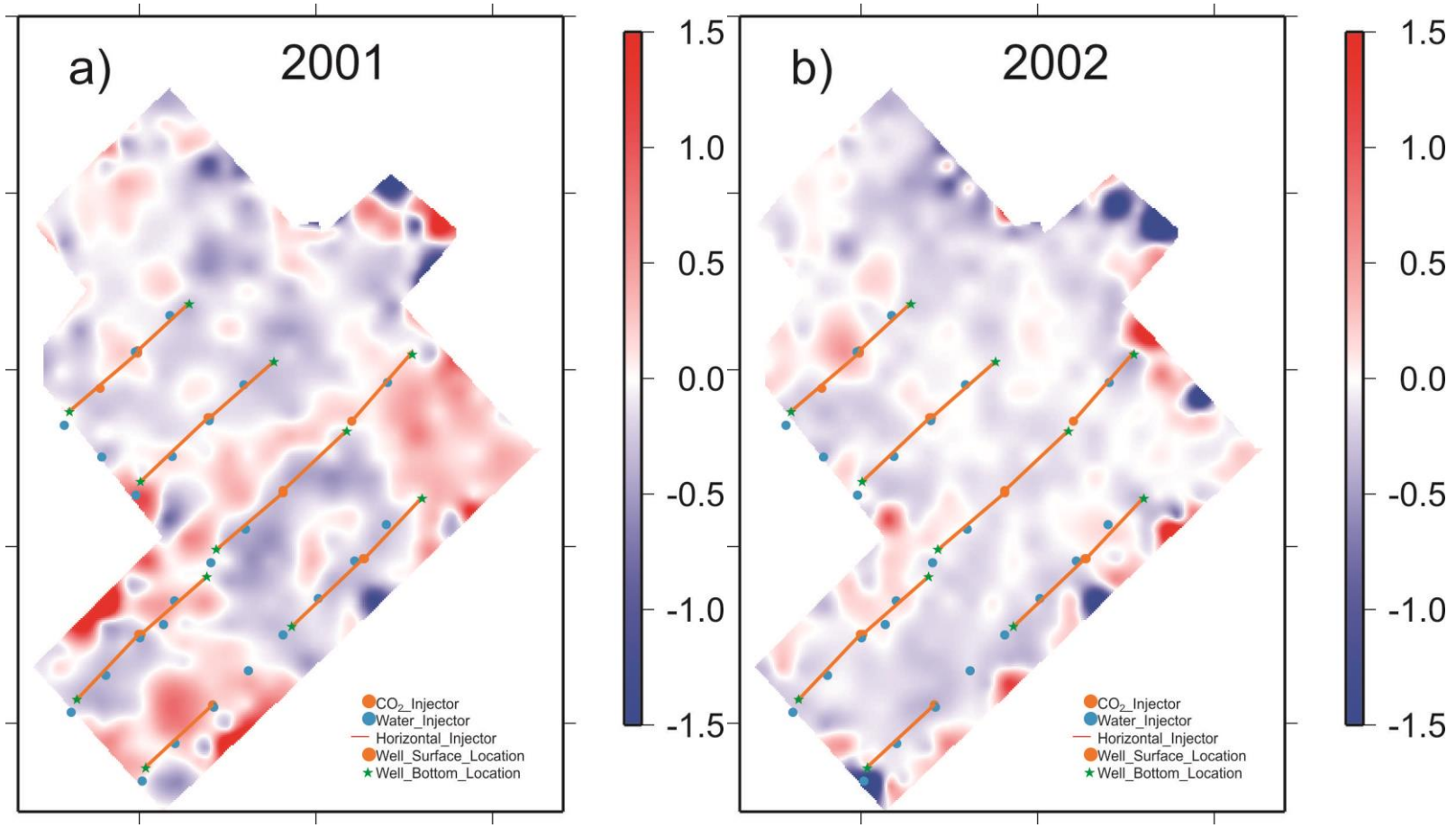

Figure 3.11. Residual time shifts of reference reflector R1 after pre-stack calibration: a) 2001 relative to 1999; b) 2002 relative to 1999. Horizontal CO_2 injection wells are shown by orange colour.

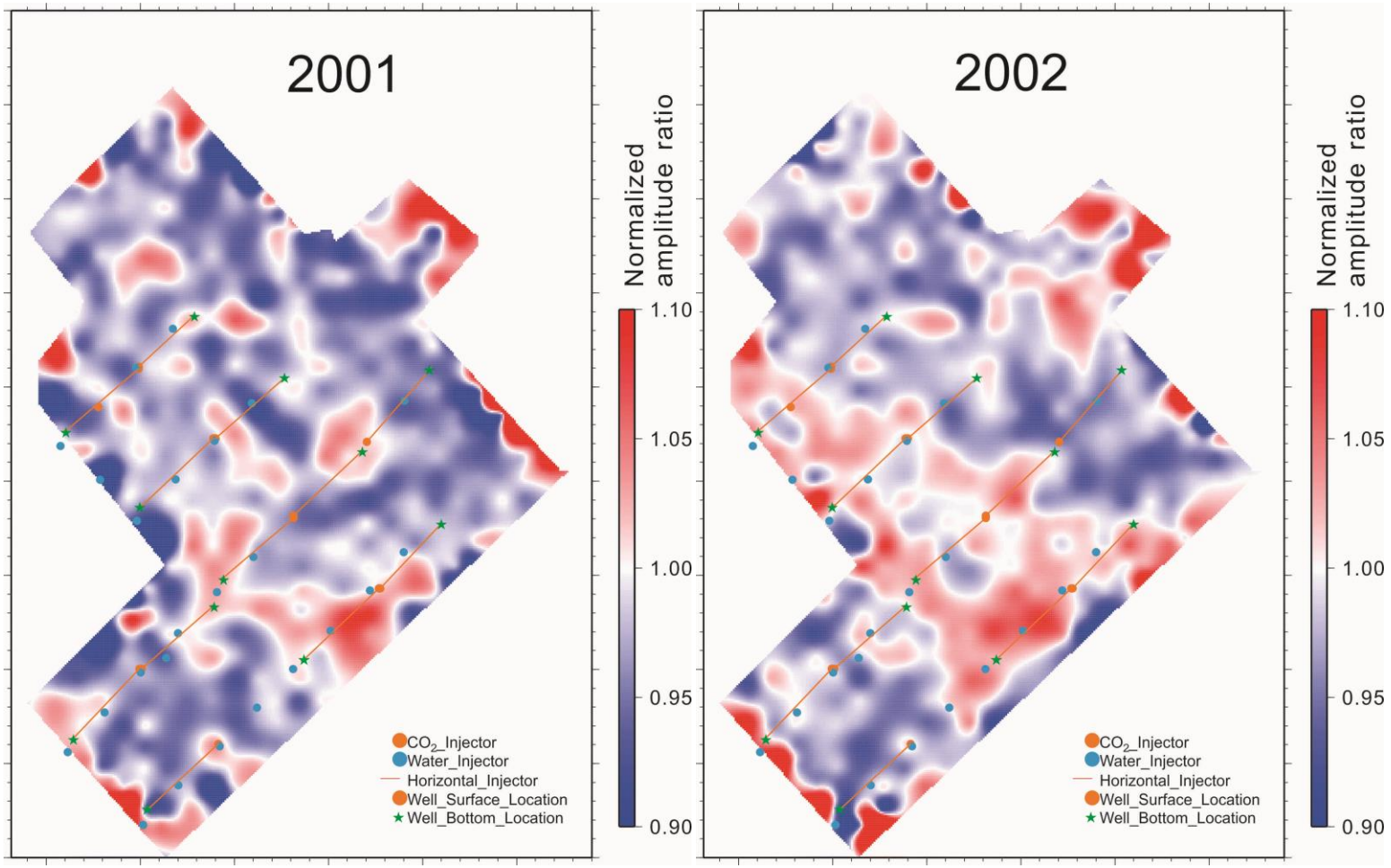

Figure 3.12. Variations of the calibrated (normalized by baseline) amplitudes at the time of caprock reflection for two monitor datasets (labelled). Normalization was performed at reference reflector R3.

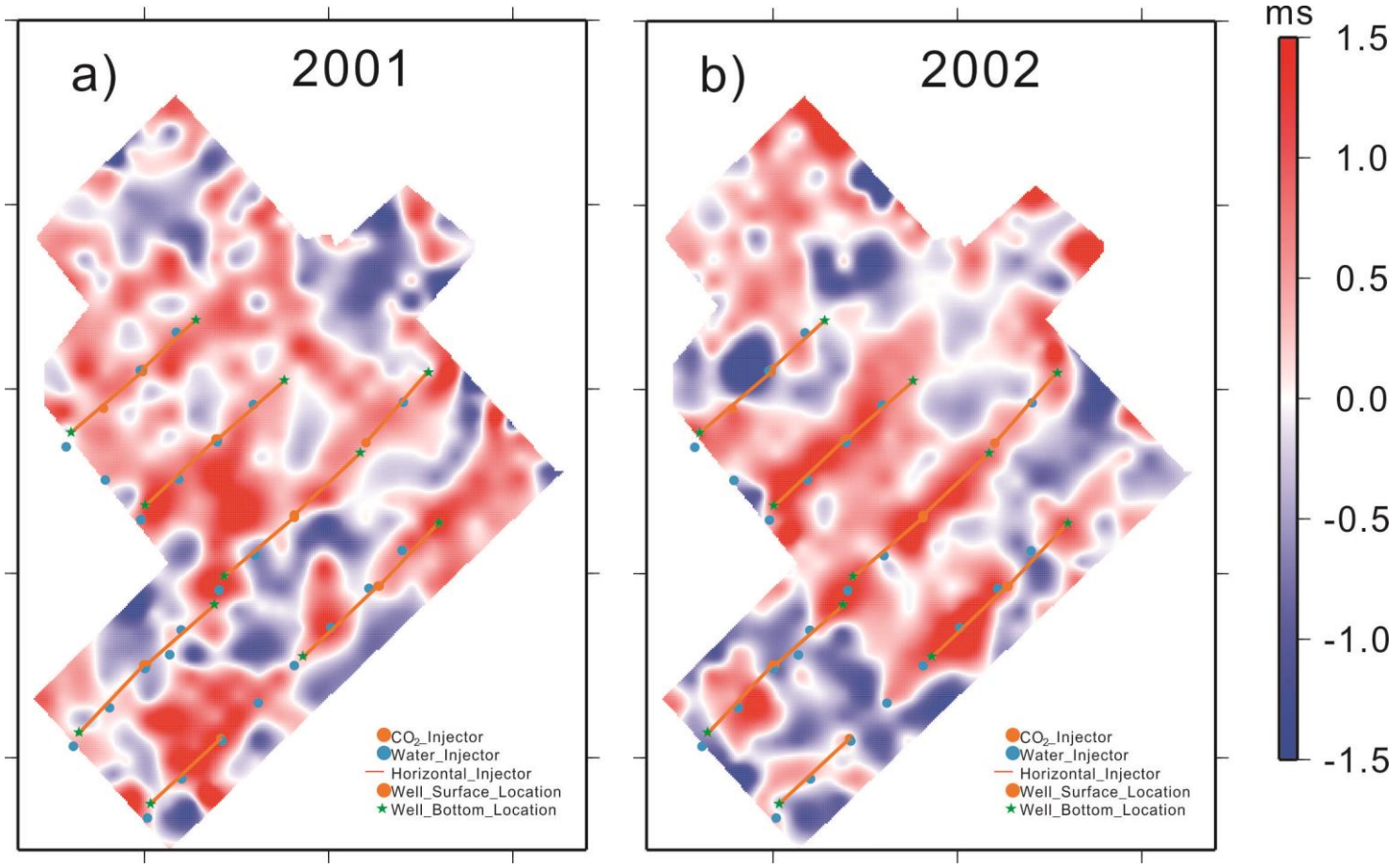

Figure 3.13. Variations of time differences between the caprock reflector and Bakken (~200ms below caprock): a) 2001 relative to 1999; b) 2002 relative to 1999. The colour bar on the right gives the estimated thickness of the fluid-affected zone below the caprock. Horizontal CO_2 injection wells are shown by orange colour.

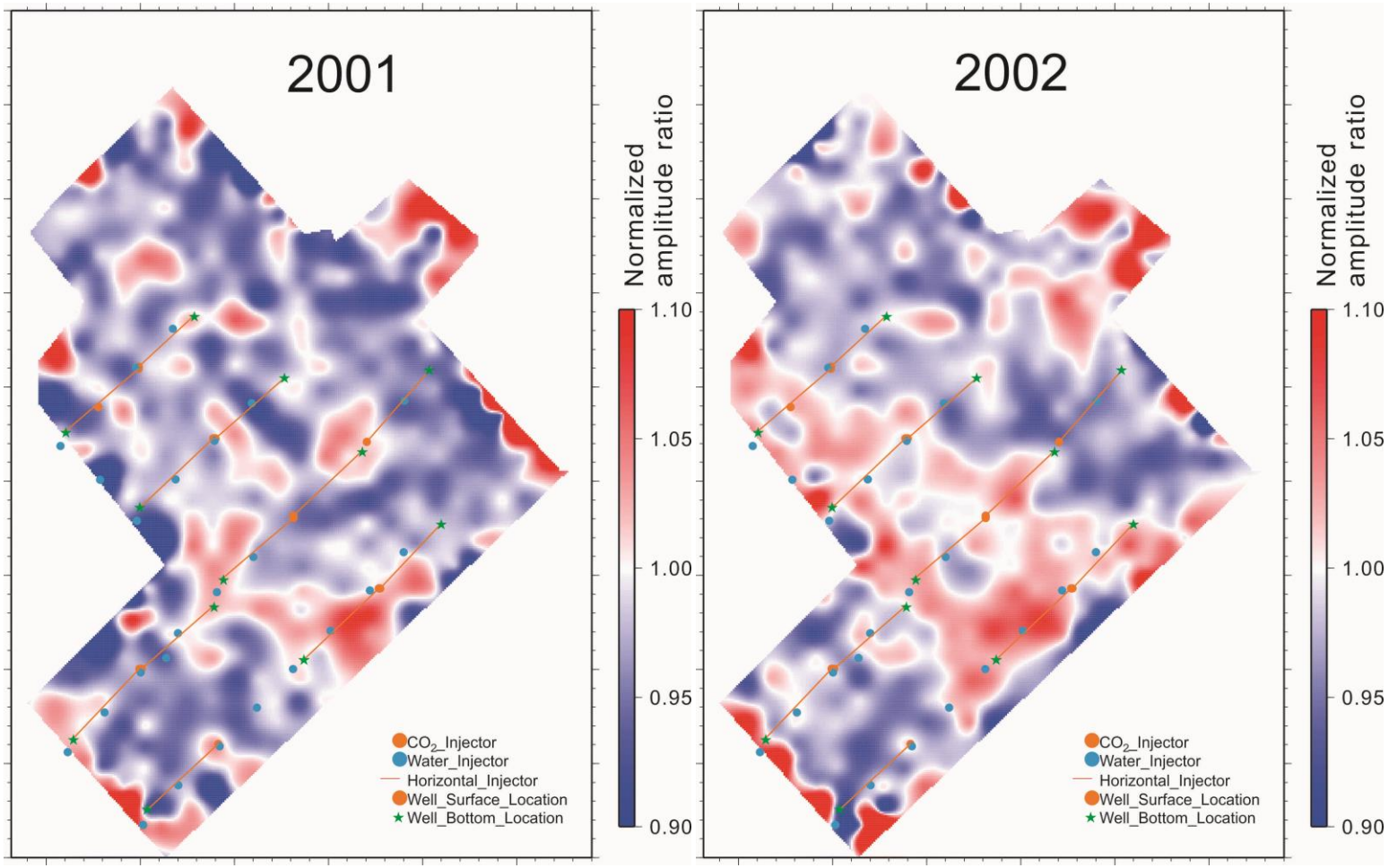

Figure 3.14. Variations of the calibrated (normalized by baseline) amplitudes at the time of caprock reflection for two monitor datasets (labelled). Normalization was performed at reference reflector R3. Horizontal CO_2 injection wells are shown by orange colour

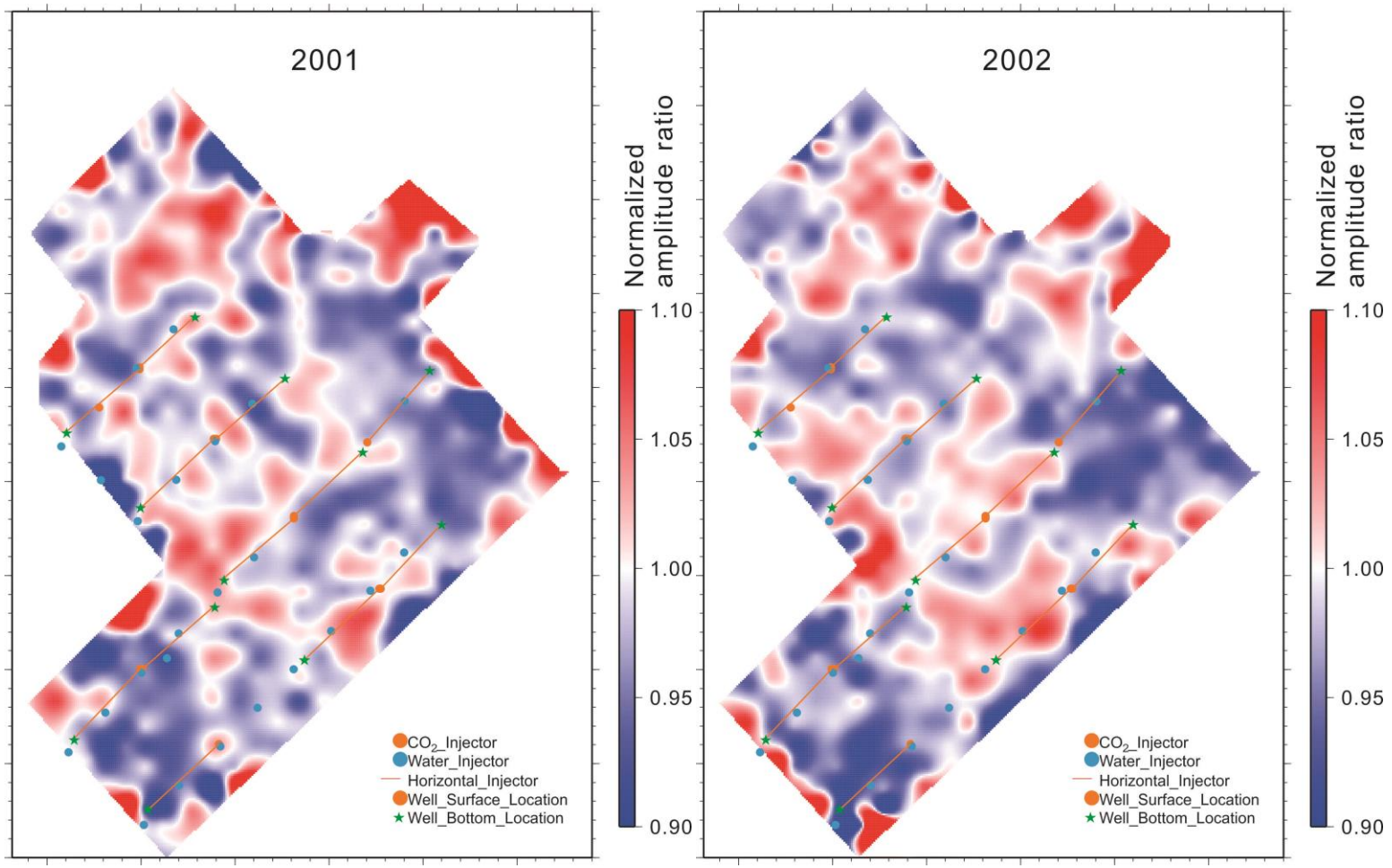

Figure 3.15. Variations of the calibrated (normalized by baseline) amplitudes at the time of caprock reflection for two monitor datasets (labelled). Normalization was performed at reference reflector R1.

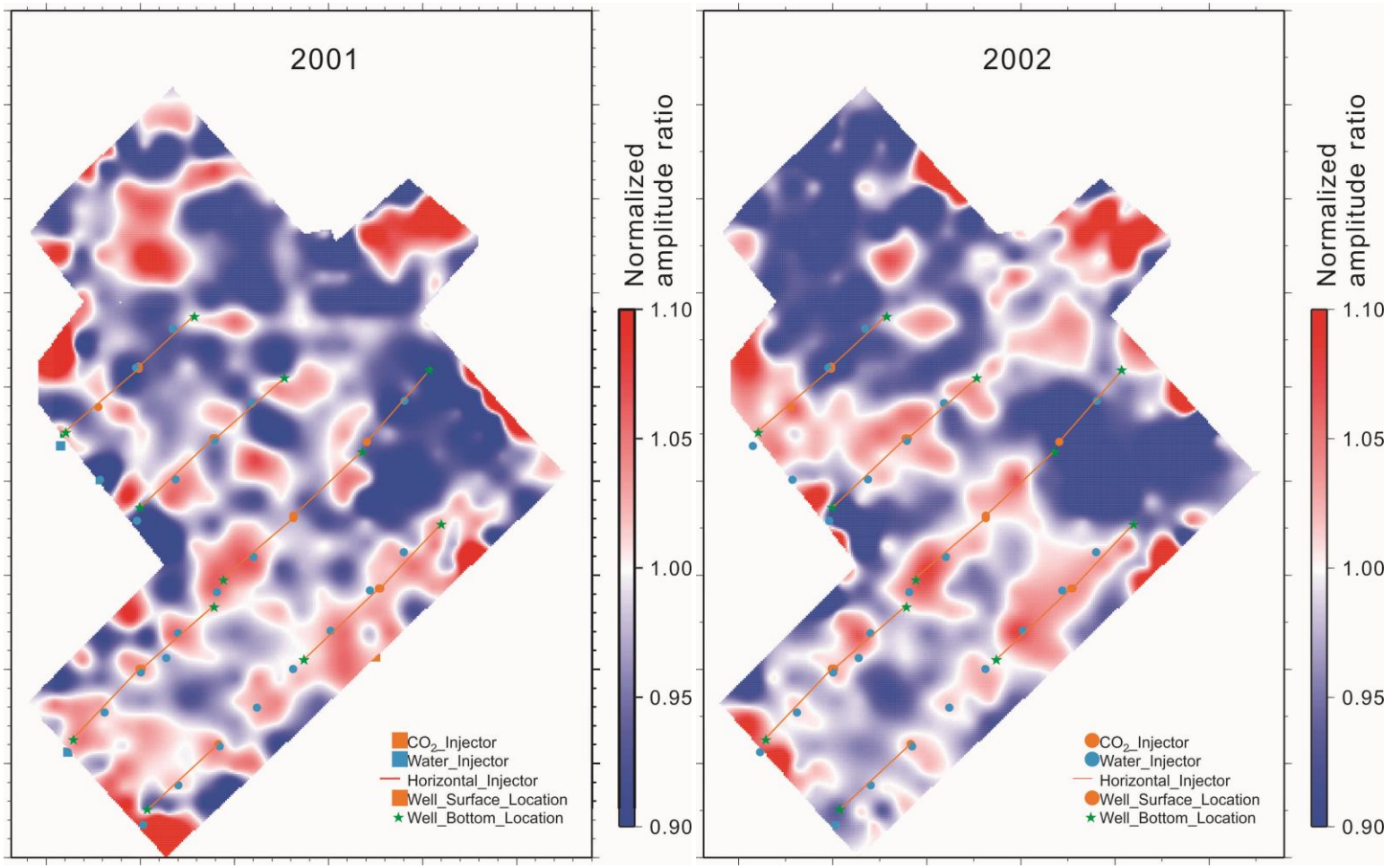

Figure 3.16. Variations of the calibrated (normalized by baseline at reference level R3) amplitudes at the time of Marly reflection for two monitor datasets (labelled). Horizontal CO_2 injection wells are shown by orange colour

3.2.3 Time-lapse variations of AVO attributes

Since approximate two-term equations are used for AVO analysis, angles up to 30° were used for measuring the AVA intercept (*I*) and gradient (*G*) attributes from seismic reflection data. The inversion for these attributes was performed by using Hampson-Russel software based on the AVA expressions given in section 3.1. The principal step of this inversion consisted in transforming the seismic data from offset and angle domain. The intercept and gradient volumes were derived independently in the Hampson-Russell software which was followed by time-lapse calibration using eq. (3.23). After this calibration, differential attributes were computed for *I*, *G*, and also secondary attributes derived from them.

The AVO attributes from the caprock show some spatial variations, which appear to correlate with injection wells, although this correlation is not definitive (Figure 3.17 and Figure 3.18). At the Marly reflection, the same correlation is present but becomes less certain (Figure 3.19 and Figure 3.20), compared with the stacked amplitudes at Marly (Figure 3.16). This loss of correlation is likely due to structural (such as thickness) variability of the reservoir, which could make the AVO inversion less stable.

Figure 3.21 shows a cross-plot of *I* and *G* for caprock and Marly reflectors. A different attribute, which may be more accurate for constraining the variations in fluid saturation, is called the "CO_2 proxy" in the "1999 Marly" panel of Figure 3.21. In the AVO measurements of real data, the observed gradient values were significantly stronger than predicted by the fluid substitution model. The resulting (*I*,*G*) points form distributions which are similar to the pressure-related AVO trends in Figure 3.7, but

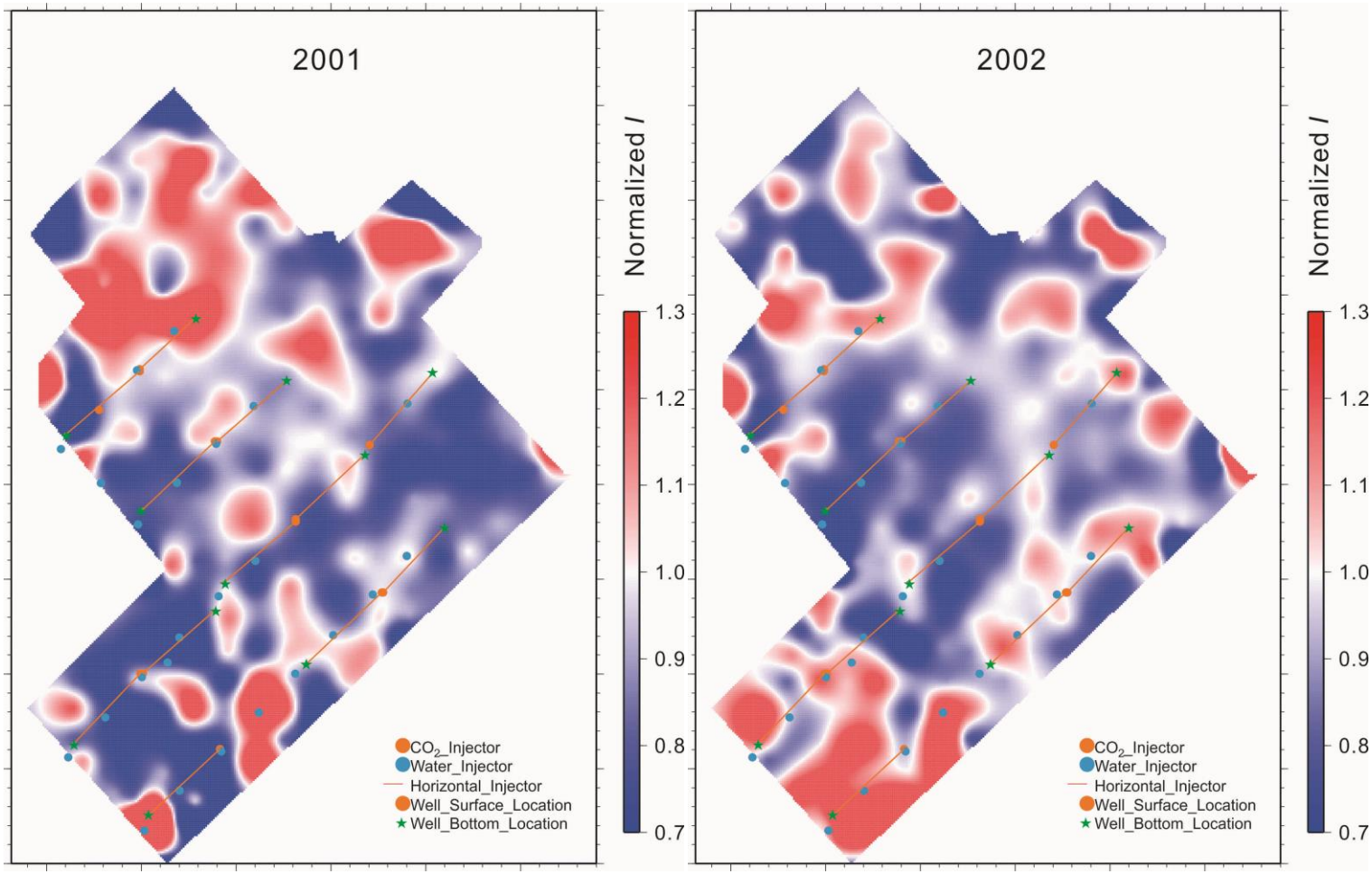

Figure 3.17. Variations of the calibrated (normalized by baseline at level R3) AVO intercepts at the caprock reflection for two monitor datasets (labelled).

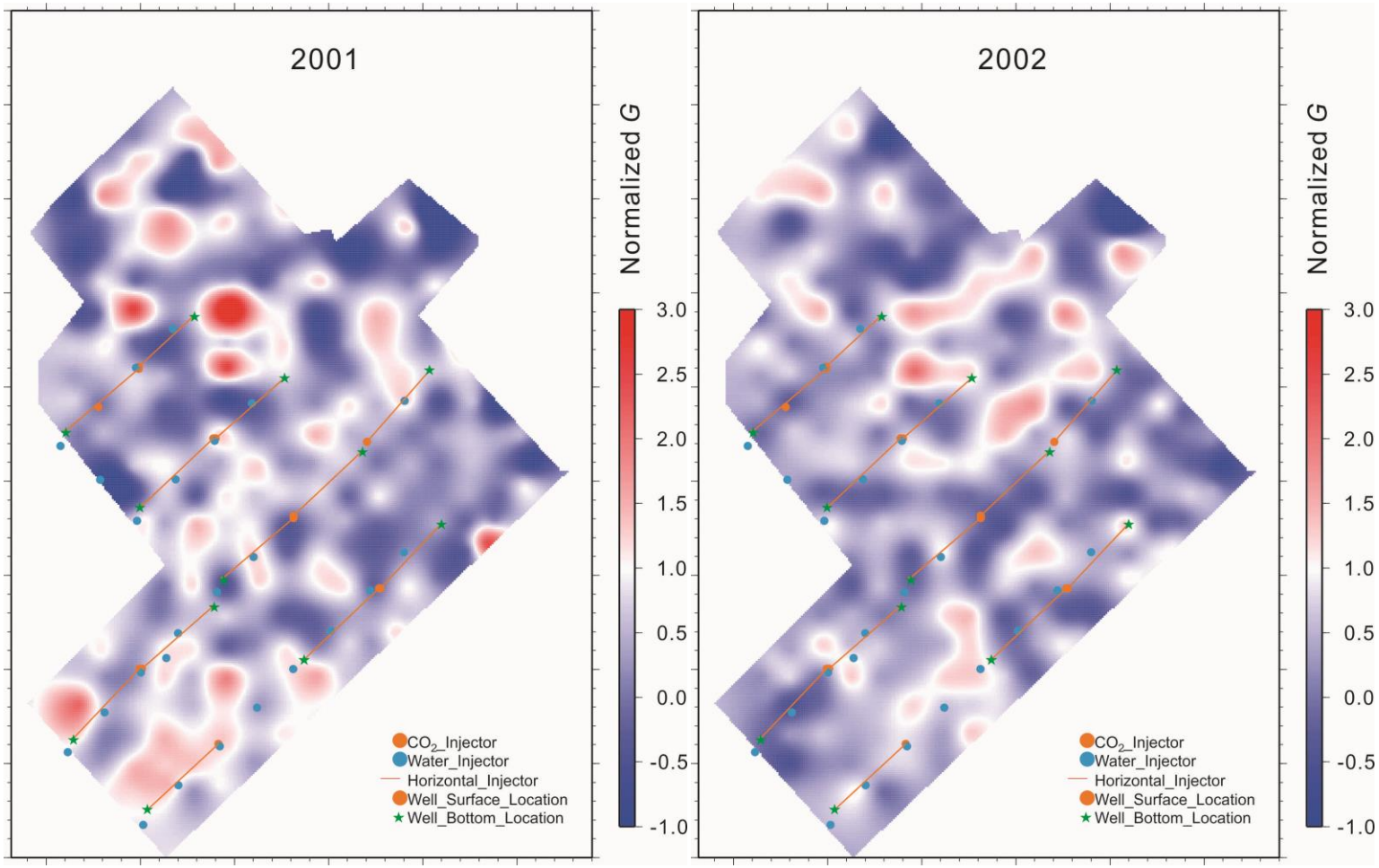

Figure 3.18. Variations of the AVO gradients calibrated (normalized by baseline at level R3) at the caprock reflection for two monitor datasets (labelled).

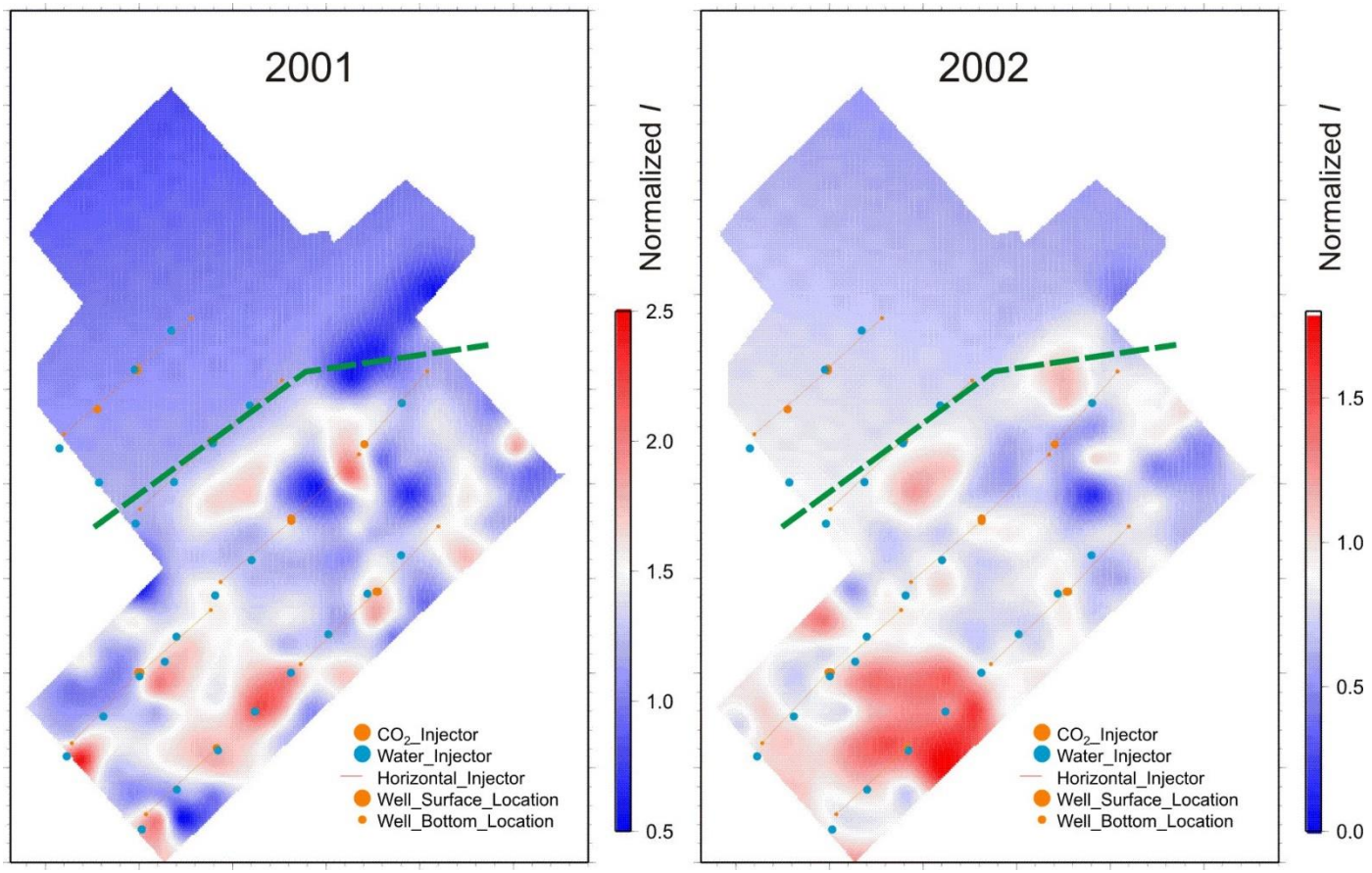

Figure 3.19. Variations of the AVO intercepts calibrated (normalized by baseline at level R3) at Marly reflection for two monitor datasets (labelled). Green dashed line indicates the approximate extent of picked Marly reflection.

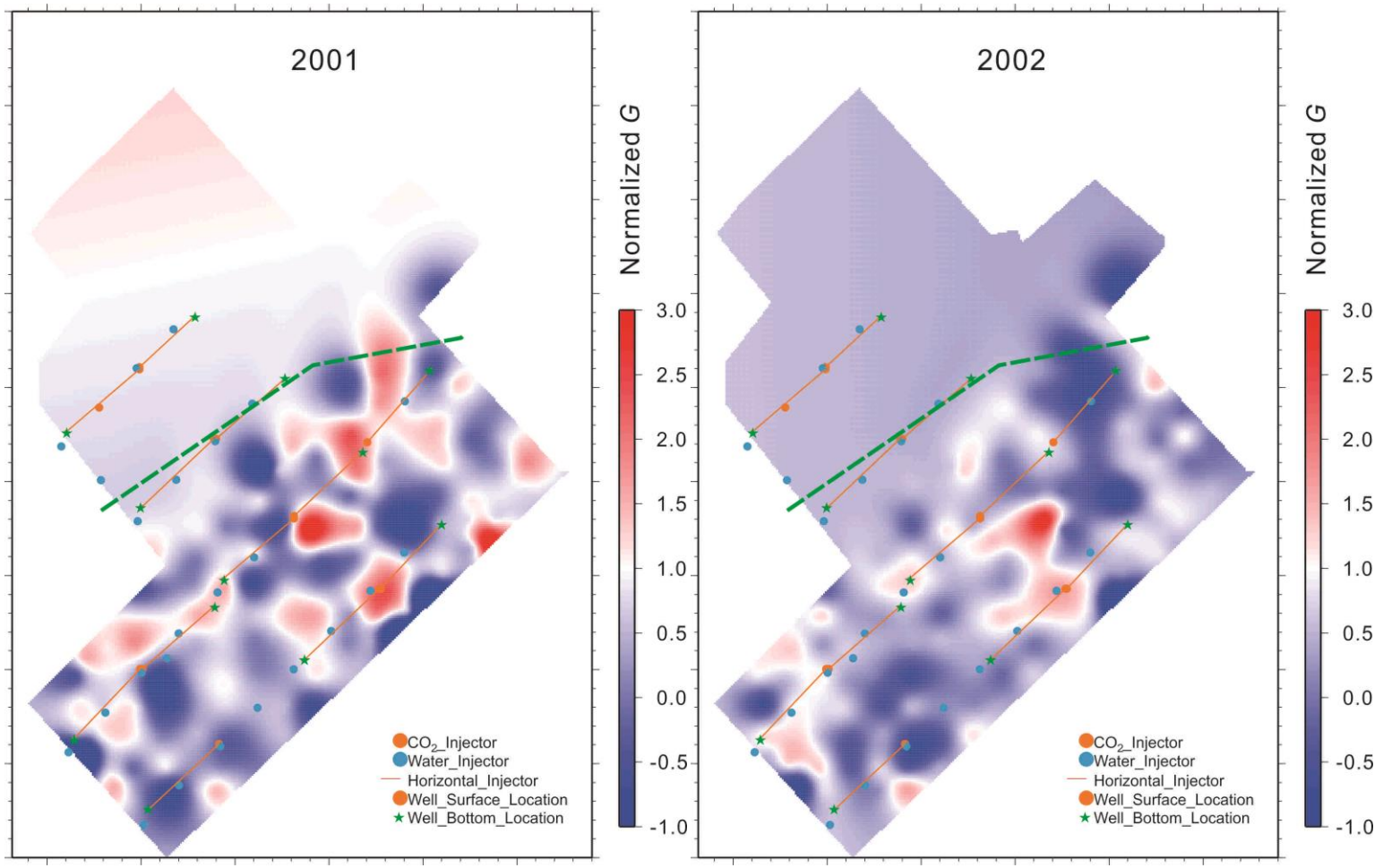

Figure 3.20. Variations of the AVO gradients calibrated (normalized by baseline at level R3) at Marly reflection for two monitor datasets (labelled). Green dashed line indicates the approximate extent of picked Marly reflection.

with characteristic G/I ratios of about 2 to 3 instead of the expected theoretical ~1 (Figure 3.21). This trend should be caused by the variations of fluid saturation as well as the structure and lithology of the reservoir. From eq. (3.15), the S-wave reflectivity can be estimated by subtracting the AVA gradient from the intercept. As mentioned in section 3.1, this parameter is more sensitive to the reservoir pore pressure and more stable than I and G alone. Figure 3.22 and Figure 3.23 indicate the S-wave reflectivity for caprock and Marly respectively. In particular, Figure 3.23 shows a good correlation of positive anomalies with the injection wells. A complementary attribute ($I+G$) should be more sensitive to the effects of CO_2 saturation (Figure 3.24 and Figure 3.25).

The attributes δP_1 and δP_2 derived from eq. (3.16), for Marly horizon are shown in Figure 3.26 and Figure 3.27 respectively. A differential attribute comparing the values of δP_2 in the monitor to baseline dataset (eq. (3.23)) is shown in Figure 3.28. Both attributes could resolve the target pressure-saturation variations to some extent and indicate similar explanation with the S-wave reflectivity and $I+G$ attributes.

Compared to Figure 3.23 and Figure 3.26, the images of year 2001 in Figure 3.27 show positive values (red zone in the dashed green lines), which could be related to the increased pressure. Such zones are absent in the R_S (S-wave reflectivity) images of the caprock (Figure 3.22), which indicates that they may be related to pressure variations within the reservoir. Considering other positive-polarity anomalies in the δP_1 images, these zones appear to be near the horizontal injection wells in which the pressure should presumably be increased. The image from year 2002 (Figure 3.26) also shows a similar pattern of variations located close to the water injection wells. However, these variations

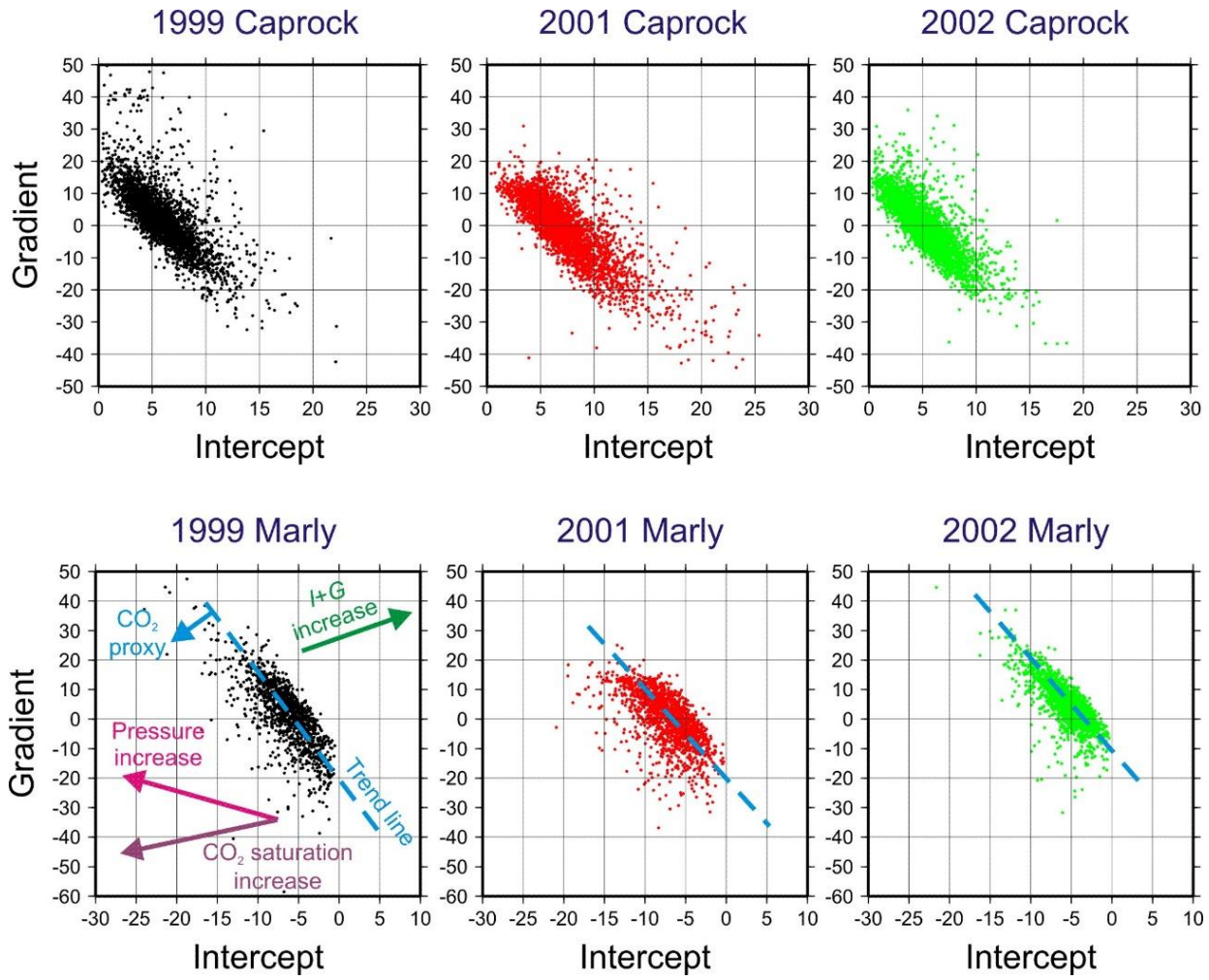

Figure 3.21. Cross-plots of normalized AVA parameters *I* and *G* for caprock and Marly reflectors within the study area. Amplitude scaling is arbitrary, as produced by Hampson-Russell STRATA program. In the plot for 1999 Marly, the pressure and CO_2 saturation trends from Figure 3.5 are shown with pink and purple arrows. Green arrow shows the direction of increasing combination (*I*+*G*). Cyan lines indicate the empirical trend and an orthogonal direction used as a proxy CO_2-saturation attribute. Similar empirical trend lines are also indicated in two other Marly plots.

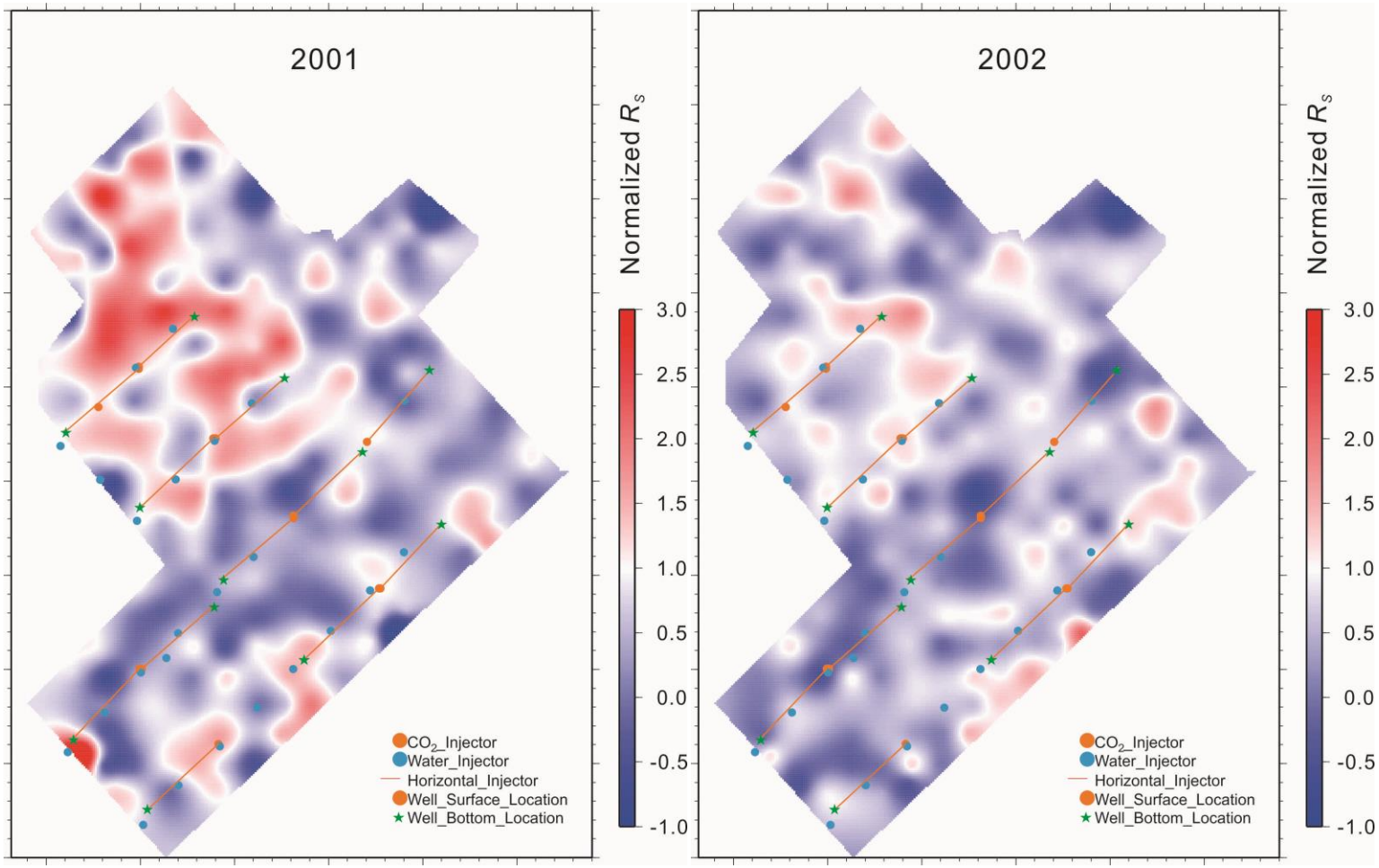

Figure 3.22. Variations of the calibrated S-wave reflectivity (*I*–*G*) at caprock normalized by baseline at level R3 for two monitor datasets (labelled).

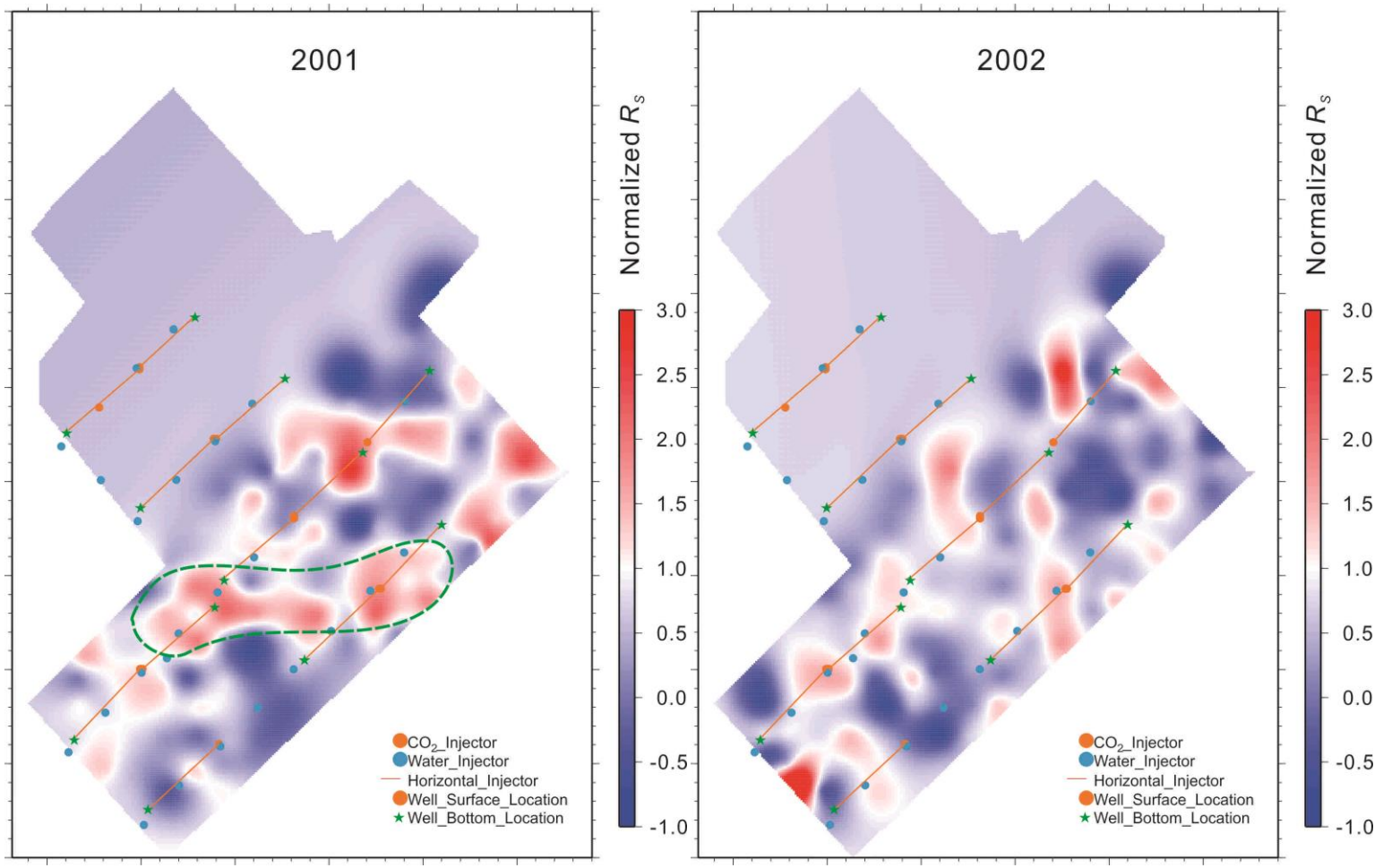

Figure 3.23. Variations of the calibrated (normalized by baseline at level R3) S-wave reflectivity (*I*–*G*) at Marly for two monitor datasets (labelled). Dashed green line indicates the interpreted area of increased pore pressure

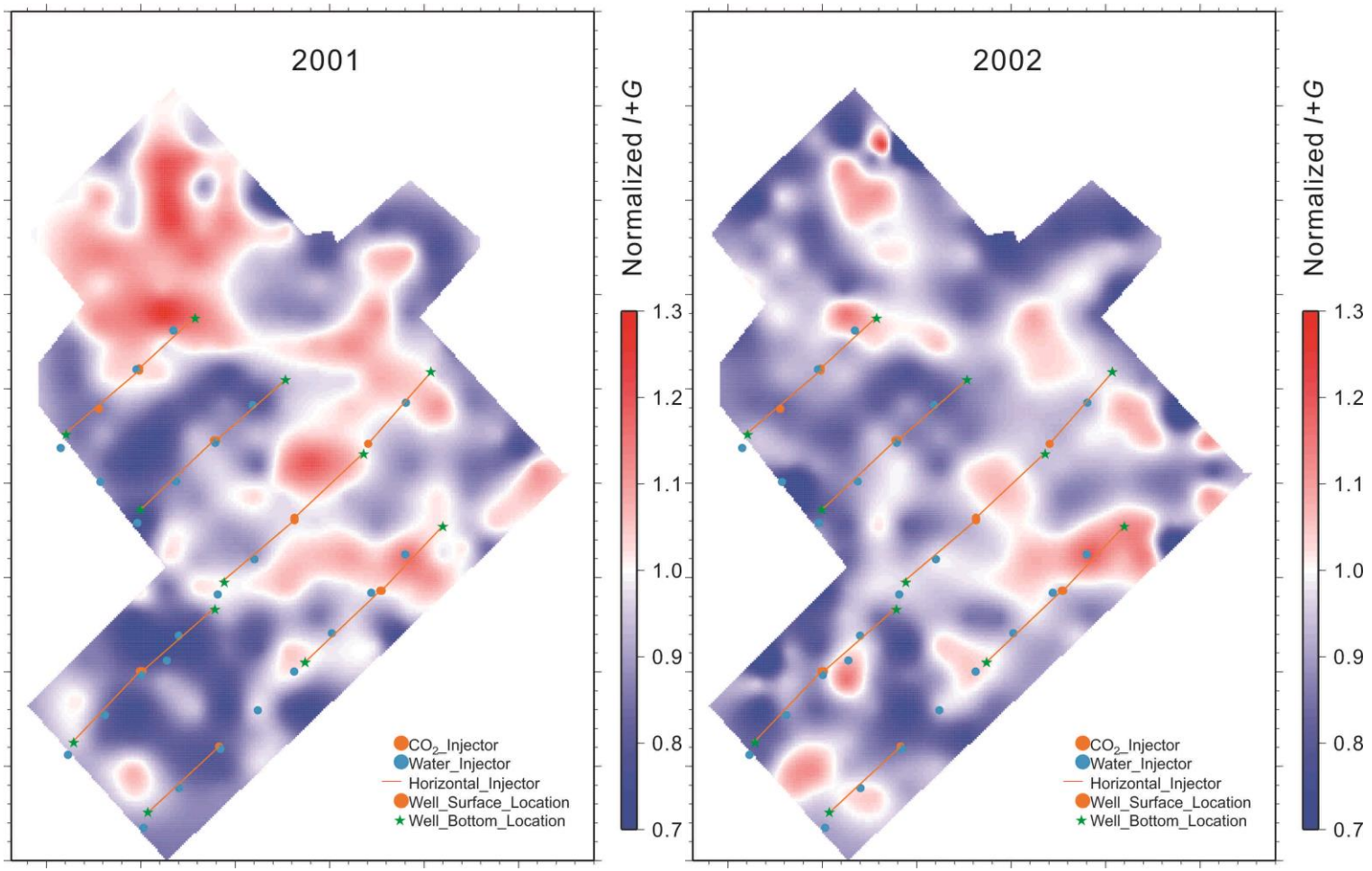

Figure 3.24. Combination of AVA attributes *I+G* (normalized at level R3 in baseline dataset) for caprock reflection.

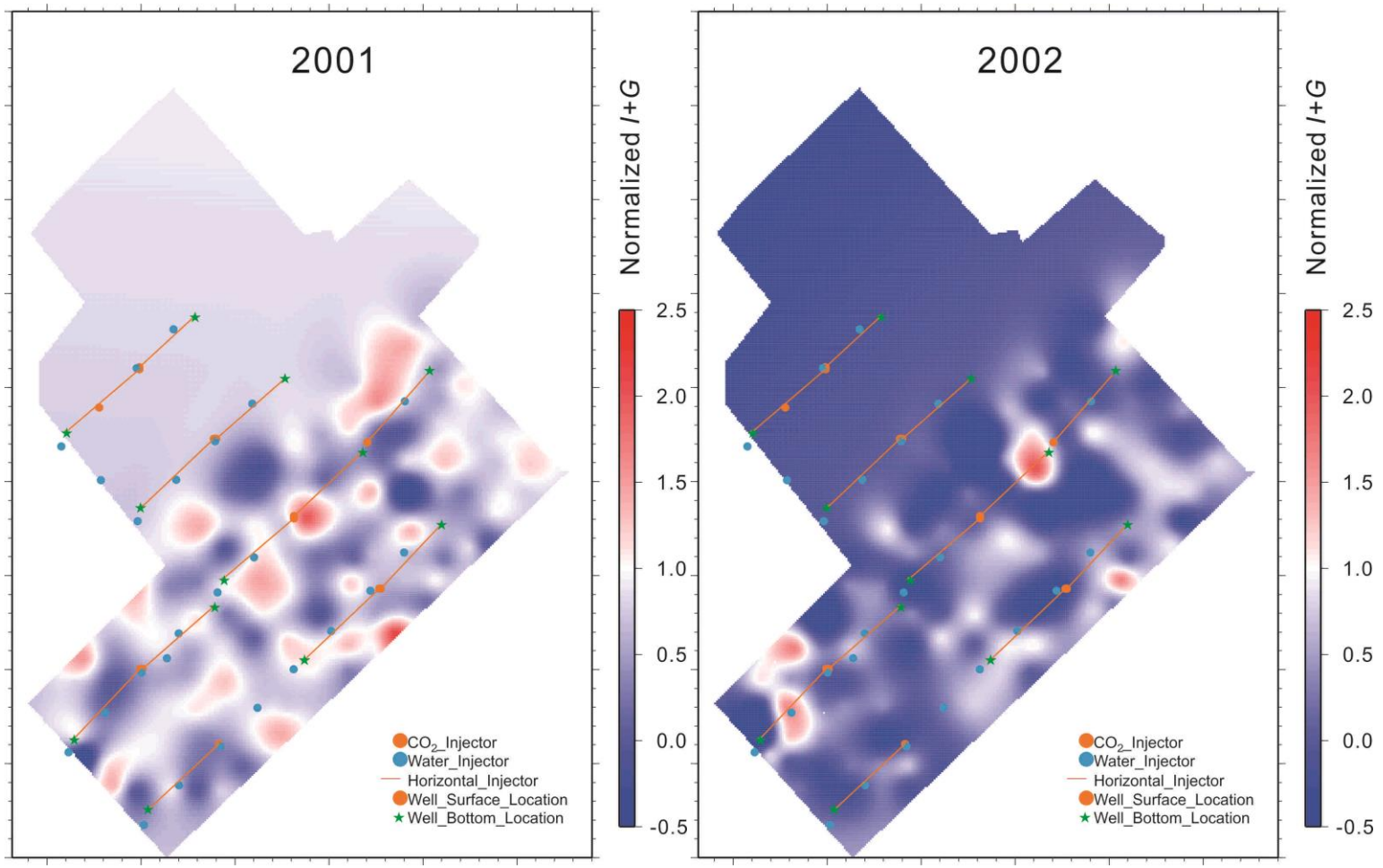

Figure 3.25. Combination of AVA attributes *I+G* for Marly reflection, normalized at level R3 in baseline dataset. This combination should be sensitive to CO_2 saturation (see Figure 3.5)

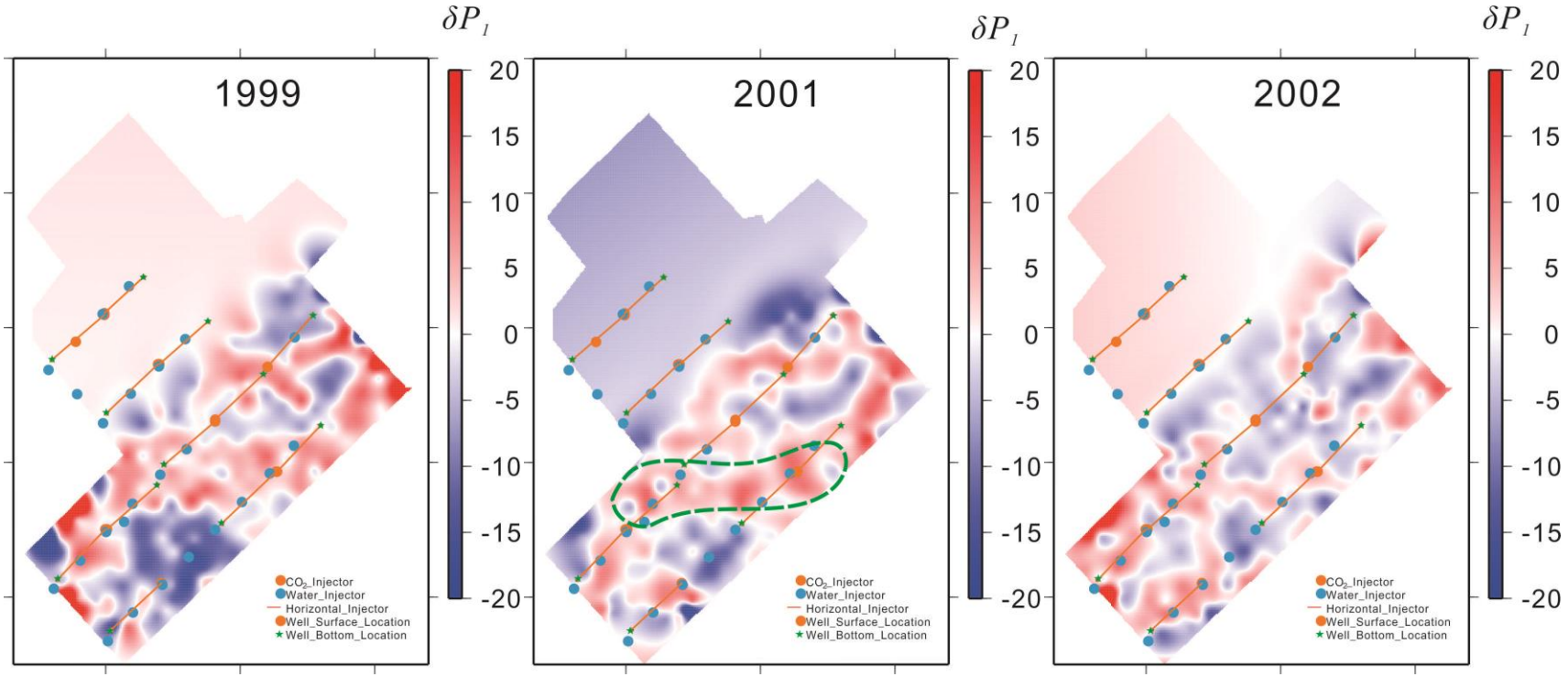

Figure 3.26. Attribute δP_1 for Marly reflection, for each of the three vintages of the dataset. Dashed green line in the image for 2001 indicates the interpreted area of increased pore pressure, as in Figure 3.23

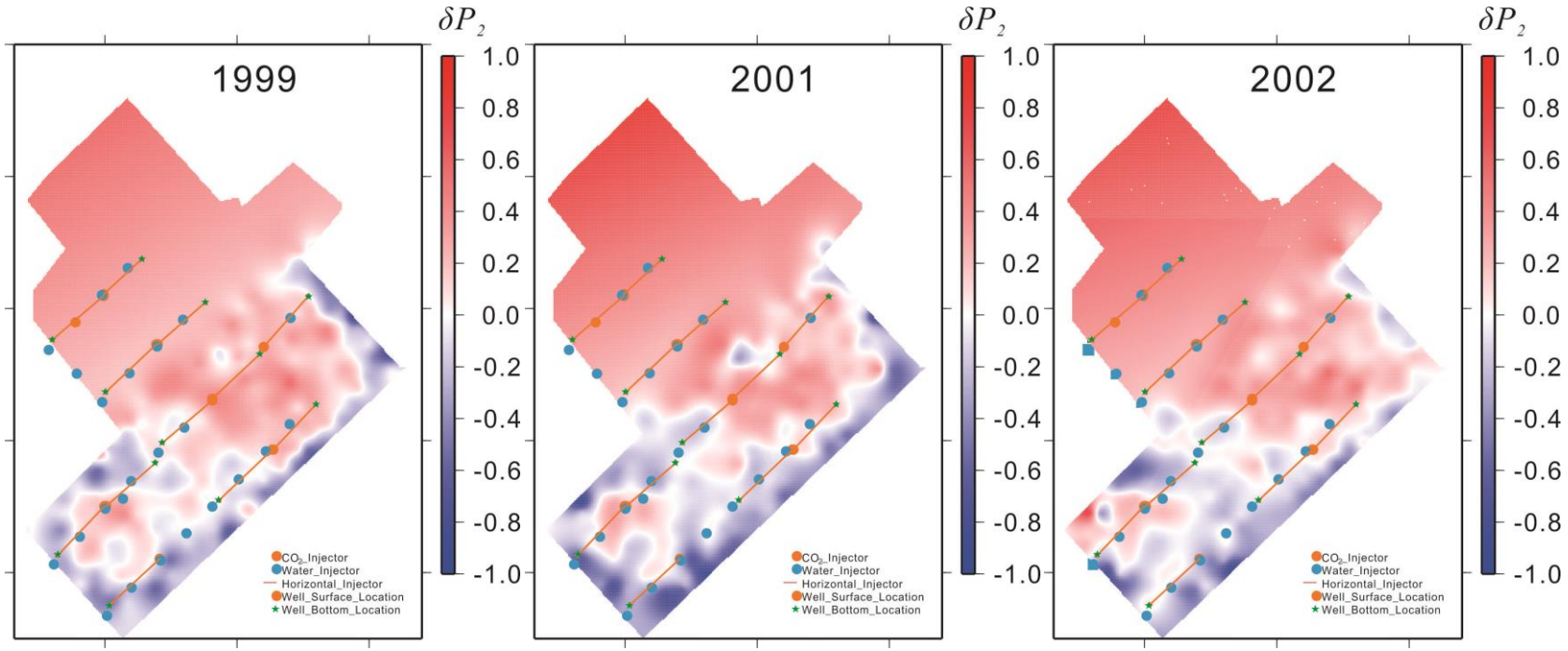

Figure 3.27. Attribute δP_2 for Marly reflection, for each of the three vintages of the dataset.

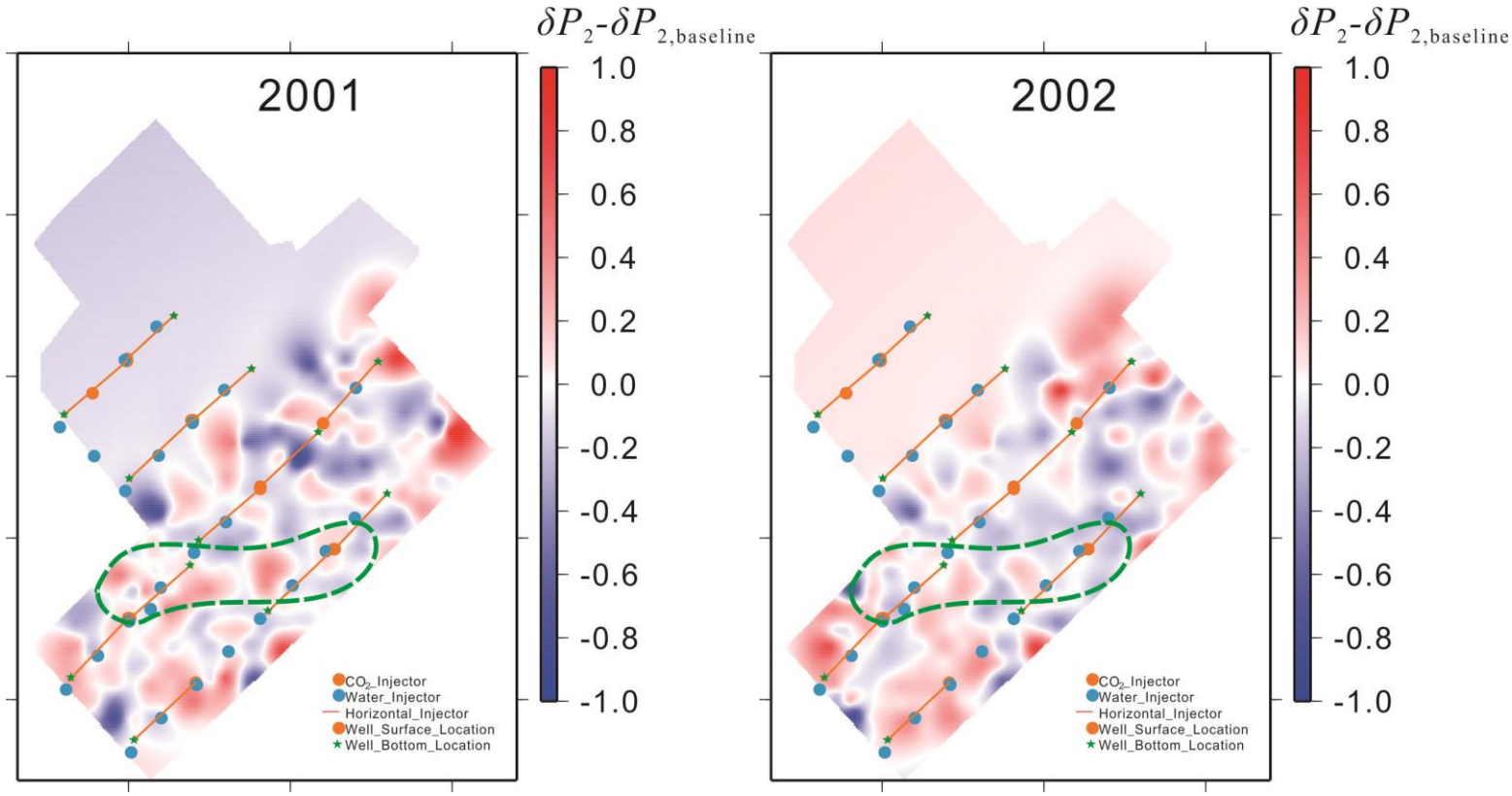

Figure 3.28. Differential attribute δP_2 for Marly reflection for monitor datasets relative to baseline. Dashed green lines indicate the interpreted area of increased pore pressure (Figure 3.20).

show weaker responses relative to the 2001 results and appear to migrate to the southeastern area.

Thus, it appears that positive-polarity anomalies in R_S and δP_1 attributes can be correlated with increased pressure within the reservoir. By contrast, negative values in the images of attribute (I+G) (blue in Figure 3.25) and δP_2 (blue in Figure 3.27 and Figure 3.28) could likely be related to increased CO_2 saturation. Thus-obtained maps of saturation variation have patchy patterns. Most anomalies are distributed along the two southern CO_2 injection wells and become more extensive in the area of interpreted pressure increase (dashed green lines in Figure 3.28).

3.2.4 Time-lapse variations of acoustic impedance

Figure 3.29 and Figure 3.30 show maps of the scaled-impedance $\frac{1}{2}\Delta \ln \zeta$ in eq. (3.22) for P-waves and S-waves, respectively. The S-wave impedance was derived from the measured AVO intercept and gradient by using the relation $R_S = (I - G)/2$ for S-wave reflectivity. In the differential P-wave impedance image (Figure 3.29), the negative anomalies (blue) show good correlation with the locations of CO_2 injection wells, particularly in the vicinities of water injectors. These anomalies are likely due to increased pore pressure similarly to the observations on the map of δP_1. However, the pressure-related pattern seen in the Figure 3.26 appears absent in the P-wave impedance map (Figure 3.29). By contrast, the S-wave impedance (Figure 3.30) shows a more pronounced pattern. Note that the scaling of this image is different from that of Figure

3.29 and corresponds to AVO attributes produced by Hampson-Russell STRATA program.

3.3 Conclusions

In this Chapter, several Amplitude Variation with Offset (AVO) attributes and acoustic impedances of the reservoir are examined by using pre-stack 3-C/3-D surface data from Weyburn CO_2 sequestration project. Among the seismic techniques for monitoring CO_2 injection, which also include P- and P/S-wave reflection imaging and inversion for P- and S-wave impedances, the AVO appears to be the most general and best for assessing the seismic effects of pore pressure and CO_2 saturation of Weyburn reservoir. In the present study, all of the above seismic attributes are derived from AVO analysis of P-wave reflections.

The resulting amplitudes and AVO attributes show several temporal trends expected from pore-pressure variations within the reservoir. However, CO_2-saturation variations could not be confidently established from the available data. The following specific observations are made from time-lapse analysis of the Weyburn datasets:

1) Analysis of differential travel times in surface-reflection records suggests about 0.5-ms delays accumulated in both monitor datasets over the areas of injection. This could mean that estimated ~10–12 m of the caprock may have been penetrated by CO_2.

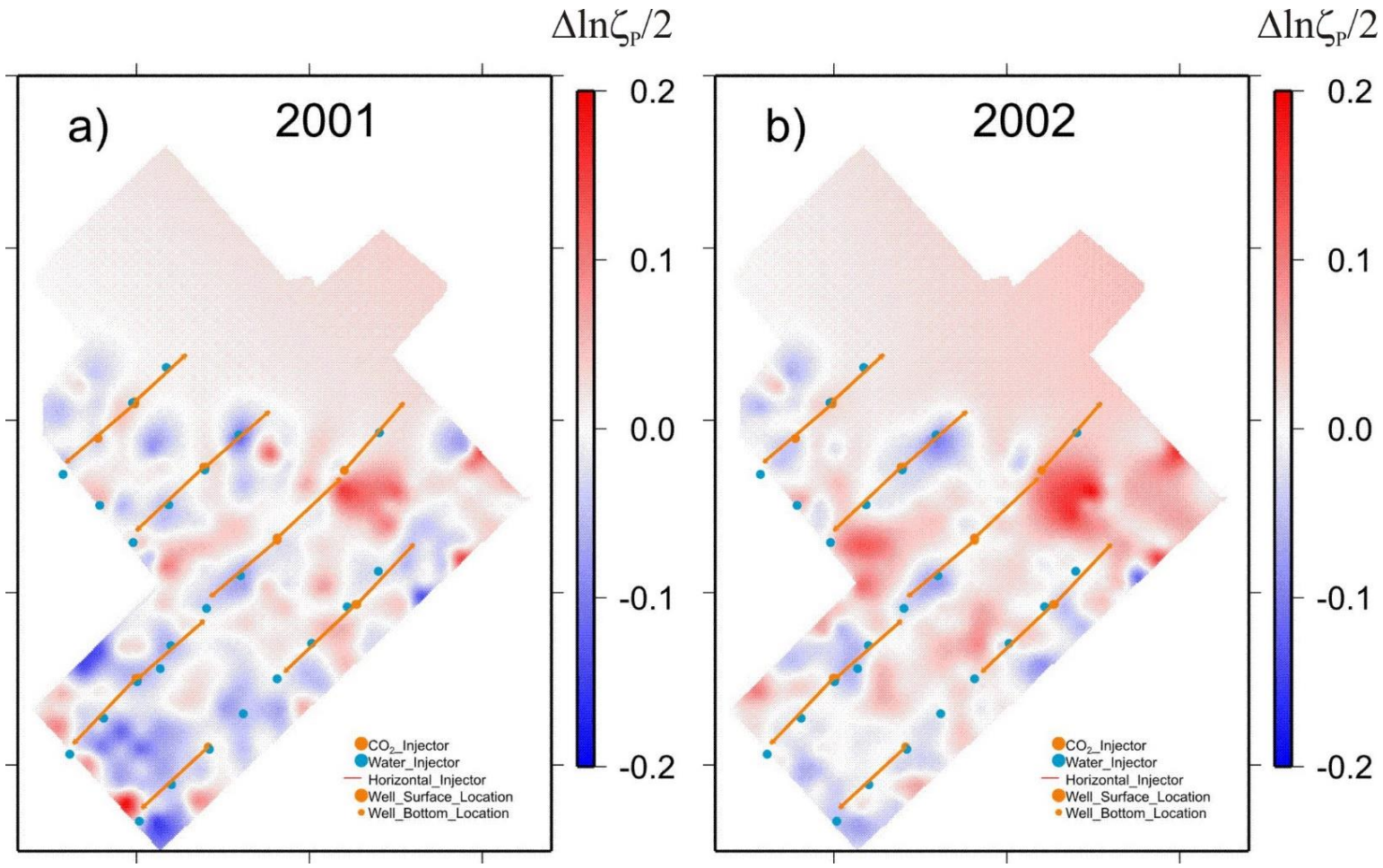

Figure 3.29. Normalized P-wave acoustic impedance variation (eq. (3.22)) at Marly level: a) 2001 monitor relative to baseline, b) 2002 monitor relative to baseline.

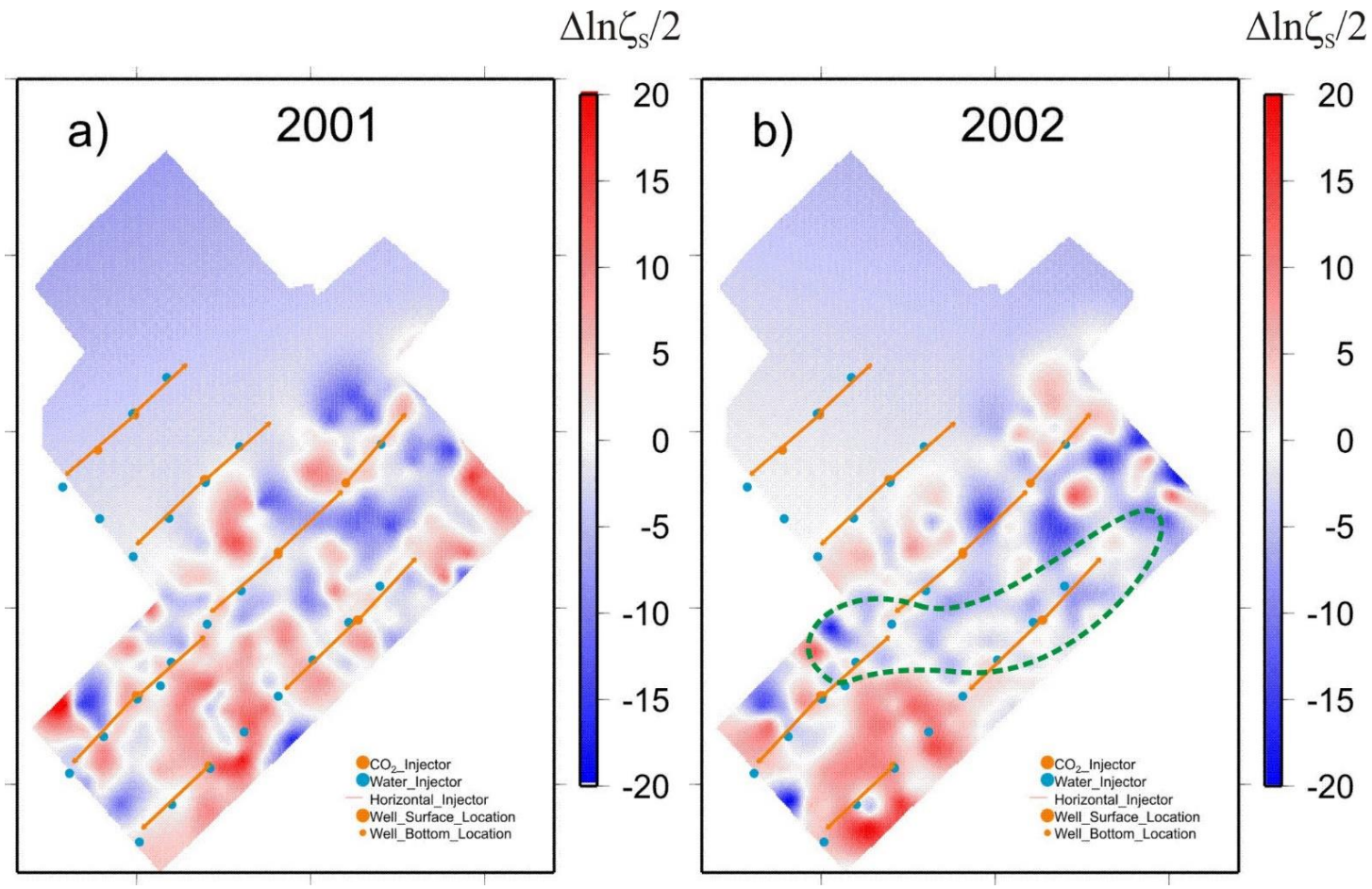

Figure 3.30. Normalized S-wave impedance variation (eq. (3.22)) at Marly level: a) 2001 monitor relative to baseline, b) 2002 monitor relative to baseline. Dashed green lines indicate the interpreted area of increased pore pressure (Figure 3.23).

2) In terms of seismic attributes that can help distinguish the CO_2 saturation from pressure-related effects, combinations of the AVO intercept (I) and gradient (G) can be used. The monitoring procedure could be similar to the identification of Class III AVO anomalies:

    a) An increase in pore pressure generally decreases I and increases G, *i.e.*, it decreases ($aG–I$), with some $a > 0$. The same variation affects the S-wave reflectivity.

    b) An increase in CO_2 saturation decreases both I and G, *i.e.*, it should be sensitive to combinations like ($I+aG$).

CO_2 produces the strongest effect on seismic properties when its saturation is low (below about 3%; Morozov and Ma, 2010). This means that seismic monitoring should be most effective at the early stages of CO_2 injection. Perhaps it would be advisable to conduct two "baseline" surveys prior to CO_2 injection, so that the variability outside of the CO_2 effects (such as due to pore pressure) can be studied. This may be particularly important if CO_2 injection follows a history of water injection, as with the Weyburn reservoir.

CHAPTER 4

RECEIVER FUNCTION ANALYSIS

In this Chapter, I describe an application of the Receiver Function (RF) method to constrain the shallow S-wave structure in the area of Weyburn 3-D/3-C study. The RF method is one of the principal tools of earthquake seismology, but in controlled-source studies, its applications are very rare. To my knowledge, the results described in this Chapter represent the only extensive application of the RF method to a 3-D/3-C seismic dataset on land.

This chapter is based on the following papers, which are directly relevant to the subject of this Dissertation:

***Gao, L**., and Morozov, I.B., 2014, Receiver function analysis of time-lapse 3-C/3-D seismic reflection data, Canadian Journal of Exploration Geophysics, 39, 30-36.*

*Morozov, I. B., and **Gao, L**., 2016, Receiver functions with artificial sources in: Thybo, H. (Ed.), Encyclopedia of Earthquake Engineering, Springer. Springer-Verlag Berlin Heidelberg 2016, p. 1-25, DOI 10.1007/978-3-642-36197-5_375-1*

My contribution to this online reference publication consisted in the sections about land 3-D receiver functions in seismic reflection data and S-wave statics (pages 18-23) and parts of the Introduction and Conclusions. I estimate my contribution to this paper as

25%. Copyright for this publication belongs to Springer-Verlag, who allows its use in the authors' theses.

The texts and figures of the above papers were merged, modified and reformatted for inclusion in this Dissertation.

4.1 Introduction

The RF method is widely used for studying and mapping the velocity structure and layer thickness within the crust and upper mantle of the earth by using permanent and temporary 3-C seismic station (Langston, 1979; Ammon, 1991). The first application of the RF method in earthquake seismology was given by Vinnik (1977), who identified the compressional (P-) to shear- (S-) wave (P/S) conversion on the 410-km and 660-km discontinuities within the mantle. Early RF studies focused on the crustal structure and investigated the PS conversion and S-wave reverberations caused by velocity discontinuities, whereas more recent research contributes to image the S-wave velocity structure of the shallow or near subsurface.

The shallow subsurface usually contains low and strongly variable seismic velocities. Low velocities tend to correlate with the spatial changes of travel-time perturbation (statics), which also affect deeper reflections. Therefore, for reflection seismic studies on land, it is most important to understand the characteristics of the shallow subsurface.

In reflection data processing and imaging, the shallow subsurface is usually described by means of statics. Accurate evaluation of source and receiver statics is critical for obtaining accurate and true images of the subsurface. Compared with conventional single-component seismic data, multi-component data contain more

information about the shallow subsurface. In the Weyburn-Midale project, in order to monitor CO_2 injection more precisely and effectively, it is critical to utilize the S-wave or converted- (PS) wave information along with P-wave information (Gao et al., 2009). With respect to the importance of S-wave information, calculation of accurate S-wave statics represents the greatest challenge of converted-wave imaging, because compared to the P- wave velocity, the S-wave velocity is much lower and not influenced by the water table and the values of S-wave static shifts can be 2-10 times larger than P-wave statics (Li et al., 2012).

In this Dissertation, I attempt to use the RF technique for mapping the near-surface S-wave velocity structure and inverting for the S-wave statics. The RF method is among the most reliable and high-resolution approaches for constraining the S-wave velocity structure of the near subsurface, particularly in combination with surface-wave inversion (Moreira et al, 2013; Lawrence and Wiens, 2004).

The controlled-source RF approach takes advantage of dense receiver coverage, three-component (3-C) recordings, and numerous shots conducted from different azimuths. As mentioned above, the principle of RF imaging of the shallow S-wave structure consists in identifying the P- to S-wave (P/S) mode conversions trailing the direct and/or reflected P waves. This method has been applied to shallow portions of wide-angle, controlled-source studies, in which it allowed mapping of 200-m to 15-km thick sedimentary covers (Morozov et al., 1998; Morozov and Din, 2008). In reflection seismic exploration, the first applications of the RF method were used to constrain the S-wave statics by Li (2002) and van Manen et al. (2003).

When computing the RFs, the source signature is deconvolved from the horizontal-component recordings for removing the converted S-wave waveforms from the vertical component of reflectivity which could improve the fidelity of reflection P-wave imaging. van Manen (2003) tested the RF technique for deriving S-wave statics from seabed seismic data, and it appears helpful to apply RF analysis to 3-D/3-C reflection seismic data on land. However, this processing is rare and few suitable tools for it are available in the conventional seismic processing procedures.

In the following sections, I extend RF analysis to Weyburn time-lapse 3-C/3-D datasets. The procedure for extraction of receiver functions from seismic exploration profiles is presented in section 4.2, from which I also infer the shear-wave velocity variations to the depths of 10 to 100 m (section 4.3). In addition, by combining with velocities and P-wave refraction model, I derive detailed 2-D maps of the near-surface S-wave velocity and statics.

4.2 Method

4.2.1 Receiver functions

In the convolutional earth model, the seismic record is given by a convolution of the source wavelet, reflected and/or converted P- and S-wave signals, and receiver response. For a 3-C signal, the corresponding 3-C RFs can be obtained by applying a common inverse filter, W^{-1}, to each component of the records (Morozov and Gao, 2016):

$$\begin{pmatrix} R_Z \\ R_R \\ R_T \end{pmatrix} \equiv \begin{pmatrix} W^{-1}u_Z \\ W^{-1}u_R \\ W^{-1}u_T \end{pmatrix}, \tag{4.1}$$

where R_Z, R_R, R_T are the vertical, radial (horizontal and directed away from the source) and transverse RFs respectively, and u_Z, u_R, and u_T are the corresponding components of the seismic record at the receiver. The role of the filter W^{-1} is in removing the effect of the source and receiver coupling, and also of the P-wave multiples (Ammon, 1991). Generally, this filter can be constructed by spiking the direct P-wave arrival in the vertical component, which will remove the source/receiver signature and isolate the converted-wave responses in the horizontal components. After the removal of the source effect, the resulting 3-C RFs in equation (4.1) represent the effects of the subsurface structure beneath the receiver station. In particular the peaks in the horizontal components of the RFs correspond P/S mode conversions (Ammon, 1991). The time lags of these conversions correspond to the differences between the primary P- and secondary P/S-wave travel times above the converting boundary.

4.2.2 Deconvolution

The role of deconvolution in seismic data processing consists in compressing the wavelet, removing source reverberations, and also reducing various kinds of multiple reflections. As a result of such signal transformations, deconvolution improves the temporal resolution and ideally leaves only the primary reflections in the records. Three types of deconvolution are commonly used in RF analysis, which are briefly summarized below.

i. Optimal Wiener deconvolution

Wiener deconvolution is also known as least-squares or optimum filtering which converts the seismic wavelet into any desired shape and has a wide range of applications.

Depending on the criteria for such "desired shape", there are several types of deconvolution methods, such as spiking deconvolution, spectral whitening, shaping filters, and predictive deconvolution (Yilmaz, 2001). The seismic wavelet converted into a spike would give a perfect seismic resolution. In real applications, due to the effects of noise, prediction-error filters may be needed to remove multiples. These approaches are optimal in the least-squares sense for the inverse W^{-1} by using different approximations for the primary wavelet.

Wiener filters can be evaluated in the time and frequency domains. The simplest form of a band-limited spiking filter for a waveform $w(t)$ in the frequency domain is:

$$w_{\text{Wiener}}^{-1}(\omega) = \frac{w^*(\omega)}{|w(\omega)|^2 + \varepsilon \langle |w|^2 \rangle}, \tag{4.2}$$

where $w(\omega)$ is the spectral amplitude, $w^*(\omega)$ is its complex conjugate, $|w(\omega)|^2$ is the spectral power, $\langle |w|^2 \rangle$ is its average, and ε is a small parameter regularizing the division in the vicinity of "spectral holes" in which $|w(\omega)|^2 \ll \langle |w|^2 \rangle$.

ii. Water-level deconvolution

In "water-level" (gain-limited) deconvolution, the denominator in equation (4.2) is regularized in the spectral holes (frequencies at which $|w(\omega)|^2$ is small) differently, by introducing a "water-level" parameter (Ammon, 1991)

$$w_{\text{WL}}^{-1}(\omega) = \frac{w^*(\omega)}{\max\left[|w(\omega)|^2, \beta \langle |w|^2 \rangle \right]} G(\omega). \tag{4.3}$$

Compared to the filter (4.2), the water-level filter does not distort the amplitudes of the inverse outside of the spectral holes. In addition, in order to suppress high-frequency noise, the result in (4.3) is convolved with a low-pass Gaussian filter $G(\omega)$. Smaller values of the water-level parameter β lead to better lower distortion of the receiver function. Similarly to parameter ε in filter (4.2) parameter β and the width of the Gaussian filter $G(\omega)$ are selected empirically, based on the quality of the deconvolved RFs in eq. (4.1).

iii. Iterative time-domain deconvolution

In receiver function calculations, iterative deconvolution is commonly used. This method was proposed by Kikuchi and Kanamori (1982) and further developed by Ligorria and Ammon (1991) to perform the deconvolution iteratively. Morozov et al. (Geophysics, in revision) proposed an application of this method to performing *Q*-compensation of reflection records. This deconvolution relies on the cross-correlation function, and the inverse filter W^{-1} is not needed. The procedure of this method consists in: 1) cross-correlating the vertical and horizontal components, 2) identifying the largest amplitudes in the cross-correlation, which are interpreted as pulses in the output seismogram (e.g., P/S mode converting boundaries), 3) convolving this output with the vertical component, producing a prediction for the horizontal component, and 4) subtracting this prediction from the horizontal component being deconvolved. This process is repeated iteratively until the horizontal-component waveform is reproduced sufficiently accurately. This deconvolution procedure does not require construction of an inverse filter and produces remarkable improvements of reflection seismic sections (Morozov et al., Geophysics, in revision). However, this procedure would be complex

and requires additional analysis if multicomponent RFs are desired (Morozov and Gao, 2016).

4.2.3 Interpretation

In contrast to the typical case in earthquake seismology, the primary P-wave in exploration cases represent refractions travelling subhorizontally and approaching the receivers at oblique angles. Figure 4.1a shows the receiver end of a refracted P-wave ray in a layered model with two possible secondary rays corresponding to a P/S mode conversion and a P-wave multiple reflection from the free surface. The principle of RF imaging consists in picking the time lag between the primary P wave and the following peak in the deconvolved horizontal components (Figure 4.1b).

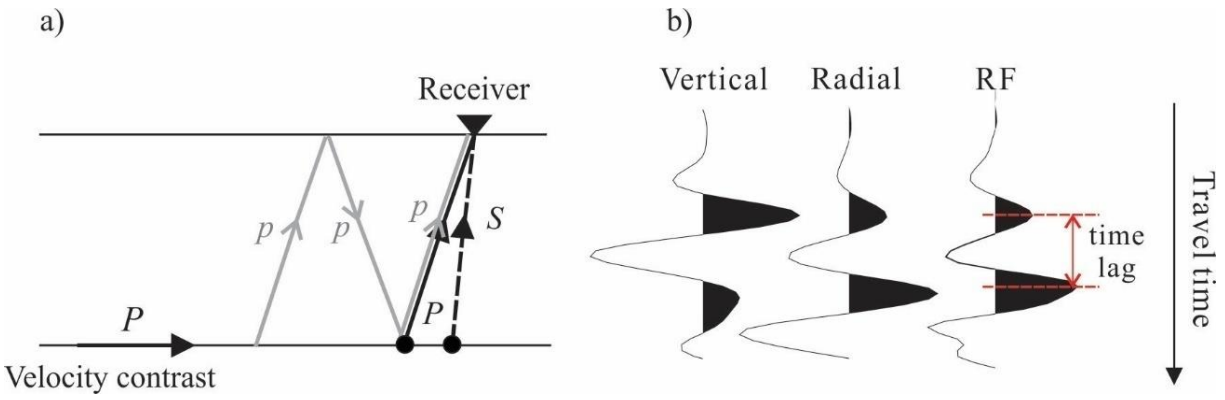

Figure 4.1. Schematic diagram for the receiver-function method using shallow refracted arrivals. a) A layered model with two secondary-wave ray paths approaching a receiver station: P-wave multiple (grey, with lower-case labels *p*) and converted S wave (dashed). Black dots show the converted points for P, p or S wave to arrive at the receiver. b) Sample waveforms of the vertical and radial components and a receiver function (RF).

For a consistent secondary arrival identified in the RF, it is necessary to verify the certainty of the P/S versus P-wave multiple interpretation (Figure 4.1a). Theoretically, at near-vertical incidence, P-wave multiples are cancelled by RF deconvolution (Ammon, 1991). However, in controlled-source RF recordings, and particularly at large incidence angles, this cancellation may be incomplete and complicated by the local structure (Gao and Morozov, 2014; Morozov and Gao, 2016). Therefore, we need to consider whether the Ppp multiple may still "leak" into the resulting RFs (Morozov and Din, 2008). To answer this question, I consider whether the RF peak can be due to the time lag δt_{PS} between the primary P-wave and converted S-wave arrivals (dashed line in Figure 4.1a).

By approximating the converted S wave as traveling near vertically, its time lag relative to the refracted P wave can be estimated as (Morozov and Din, 2008):

$$\delta t_{\mathrm{PS}} = h\left(\frac{1}{V_{\mathrm{S}}} - \frac{\cos\theta_{\mathrm{P}}}{V_{\mathrm{P}}}\right), \tag{4.2}$$

where V_{P} and V_{S} are the P- and S-wave velocities, respectively, h is the thickness of the low-velocity overburden, and $\theta_{\mathrm{P}}$is the critical angle for P waves. The time lag δt_{Ppp} between the primary P and Ppp waves can be expressed as:

$$\delta t_{\mathrm{Ppp}} = \frac{2h\cos\theta_{\mathrm{P}}}{V_{\mathrm{P}}}. \tag{4.3}$$

As shown in the next section and also in Morozov and Gao (2016), these two interpretations can be distinguished based on the travel-time moveouts with variable ray parameter, and also on the amplitudes.

Finally, if the observed RF lags correspond to P/S conversions (as in the next section), the S-wave statics ($\overline{t_S}$) relative to the refracting interface can be derived based on the P- and S-wave velocities, P-wave static ($\overline{t_P}$) and the measured RF lag:

$$\overline{t_S} = \overline{t_P} + \delta t_{PS} - h\left(\frac{\cos\theta_S}{V_S} - \frac{\cos\theta_P}{V_P}\right). \quad (4.4)$$

4.3 Application to Weyburn 3-D/3-C dataset

4.3.1 Near-surface layering

The refraction statics model derived for the baseline dataset (Chapter 2) shows that the average depth of the shallow subsurface is near 26 m and the average P-wave velocities above and below the refractor are about 1966 m/s and 2300 m/s respectively. From these estimated velocities, the impedance contrast for this boundary is about 18%. This is a significant contrast from which the P/S conversions and Ppp multiples can occur. In the subsequent interpretation of the RFs, I refer to this velocity contrast as a possible source of P/S model conversions, and attempt deriving the S-wave velocity variations above this boundary.

4.3.2 Receiver-function deconvolution

In order to compute the RFs, the data were sorted into common-receiver gathers and the first-arrivals times were aligned for all records. For convenience of the display, the first breaks were aligned at constant time of 50 ms (Figure 4.2). By using the aligned first arrivals in each vintage of the data, minimum-phase spiking filters were constructed for each trace in the vertical-component receiver gathers using ProMAX. The operator length

for this spiking filter is 20 ms in order to avoid contaminating the refractions. These filters were subsequently used as inverse filters W^{-1} in equation (4.1) to deconvolve the vertical, radial, and transverse common-receiver gathers from the corresponding vintages of the dataset. Because the high-frequency noise becomes boosted by deconvolution, I applied low-pass filtering to the resulting RFs. Finally, by inspecting the common-receiver RF profiles and determining the ranges of records containing the optimal RF data quality, the RF sections were stacked to produce a single RF for each receiver.

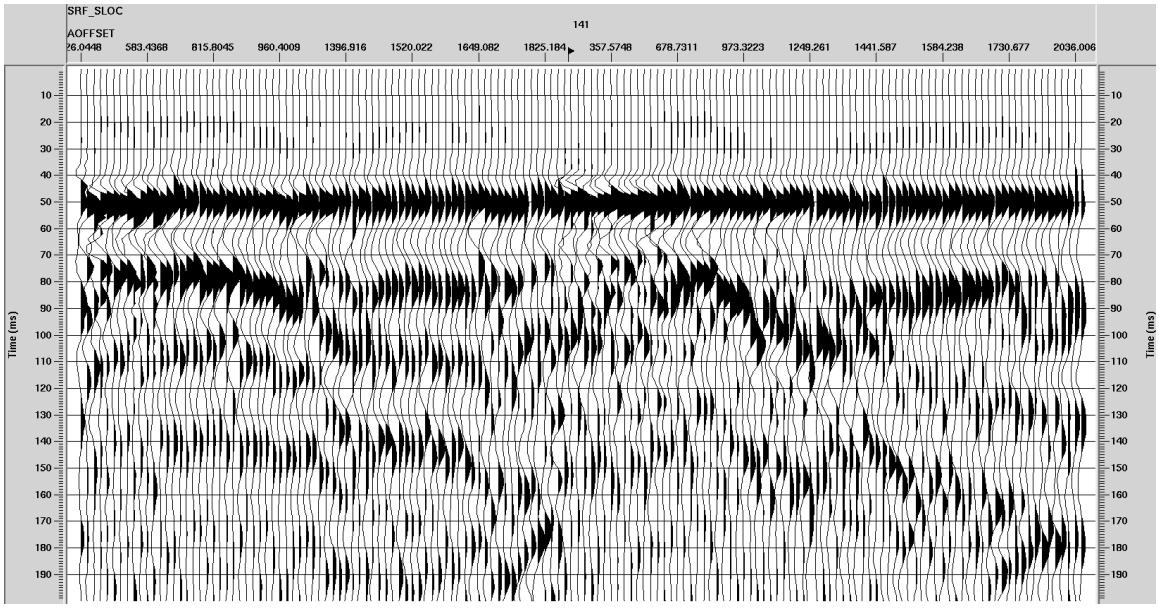

Figure 4.2. An example of a vertical-component common receiver record at surface location SRF_SLOC=141. The first breaks are aligned at 50 ms.

A sample RF gather from one receiver is shown in Figure 4.3. As an input to the minimum-phase spiking deconvolution, the first arrivals in these records were aligned at 50ms. The deconvolved vertical-component records should generally contain a single

pulse within the deconvolution operator length, which can be used for quality control (Figure 4.3a). In the deconvolved radial RFs, the primary P-wave pulse is also the largest peak, followed by a peak caused by the interpreted P- to S-wave conversion. The records show consistent time lags at each common-receiver RFs between the S- and P-wave arrivals (blue and red lines in Figure 4.3). Due to the effects of noise and likely near-surface heterogeneity, there is a scatter in the values of times for different receivers of about ±5 ms.

The observed travel-time RF lags agree with the interpretation of their being caused by P/S conversions in the near surface. To investigate the alternate interpretation of RF lags (Figure 4.3) as caused by a P-wave multiple, I used the predictions for the time lags in equations 4.2 and 4.3. Based on the refraction model parameters above and the S-wave

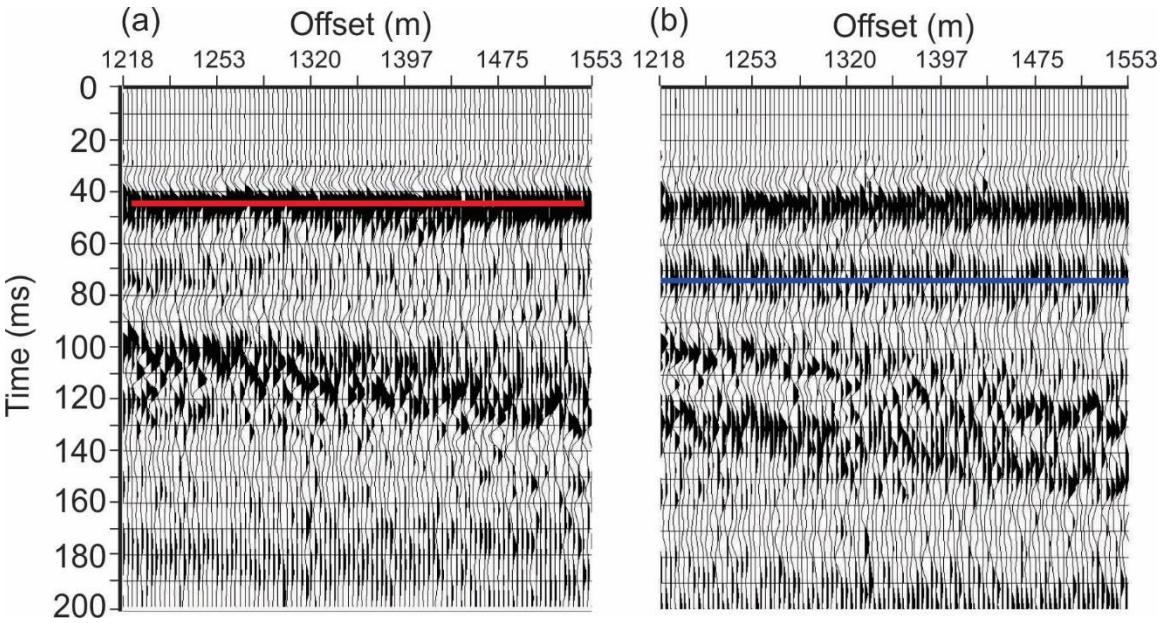

Figure 4.3. Application of RF to common-receiver gather from receiver #181:

(a) Vertical RF and interpreted P-wave arrival times (red);

(b) Radial RF and interpreted S-wave arrive times (blue)

velocity of 600 m/s, the time lag for the converted P/S mode should be $\delta t_{PS} \approx 35$ ms, and for a P-wave multiple, are and $\delta t_{Ppp} \approx 12.7$ ms in the forward modeling. The first of these values is close to the time lags observed in the data (Figure 4.3). Therefore, I conclude that these arrivals are associated with P/S mode conversion (as expected from a RF; Ammon, 1991). In addition, this interpretation is consistent with observing this arrival in the radial-component records. Several additional examples of the RFs are shown in Figure 4.4.

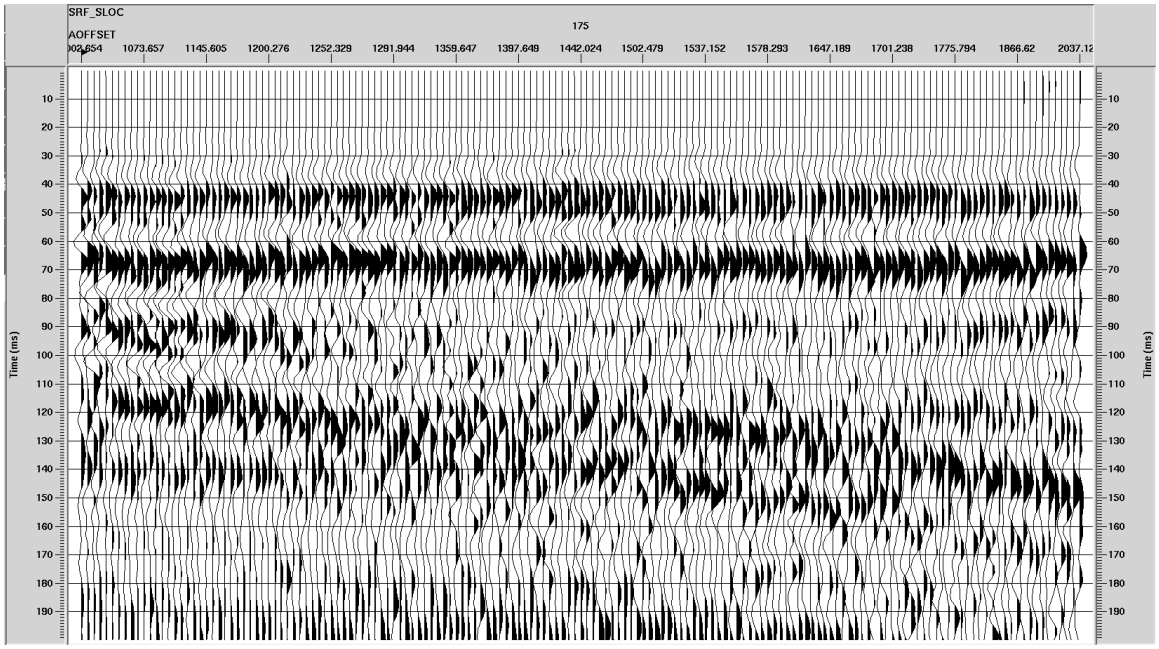

Figure 4.4. Several examples of receiver-functions sections derived from 3-component first-arrival waveforms.

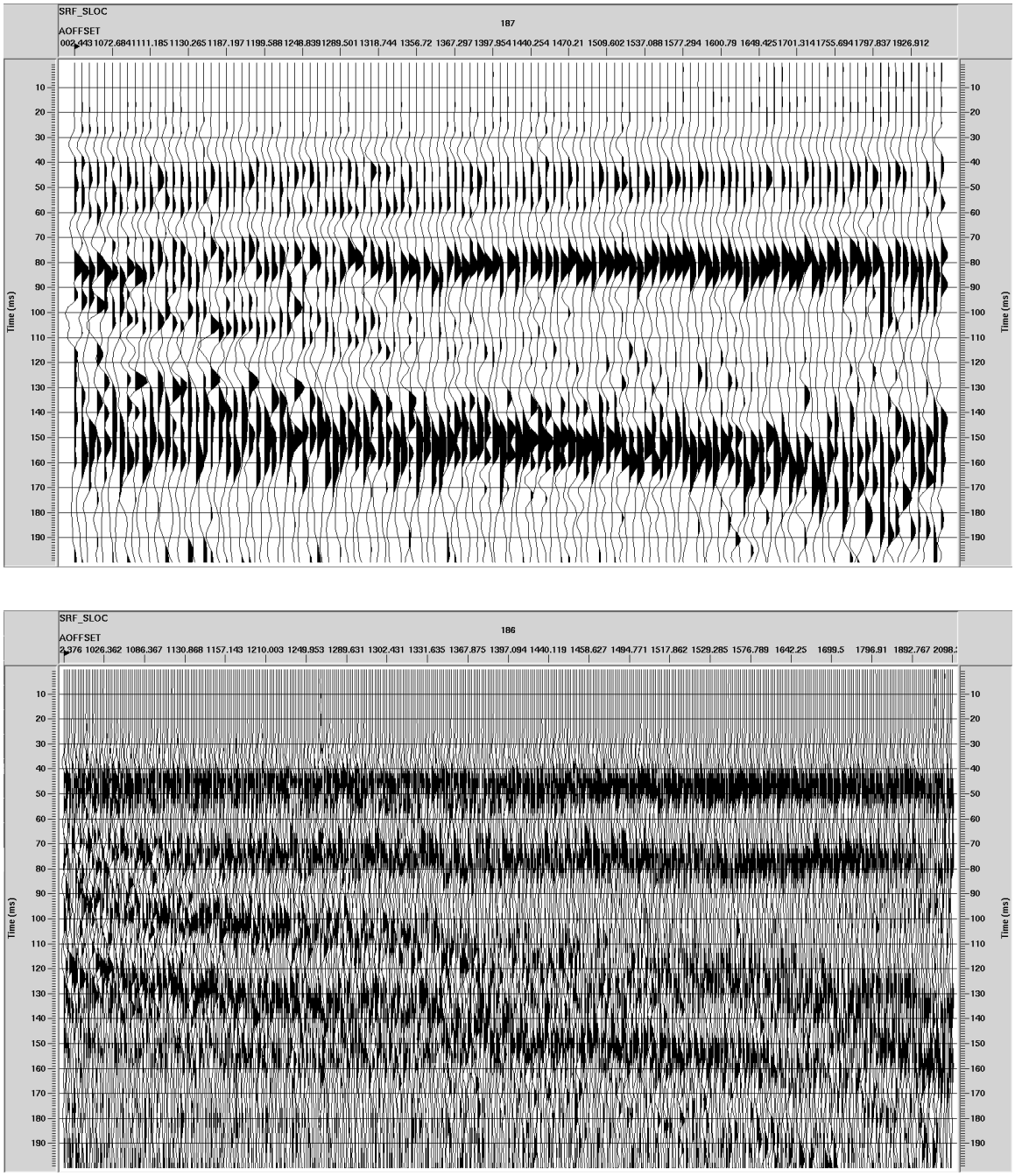

Figure 4.4 (continued).

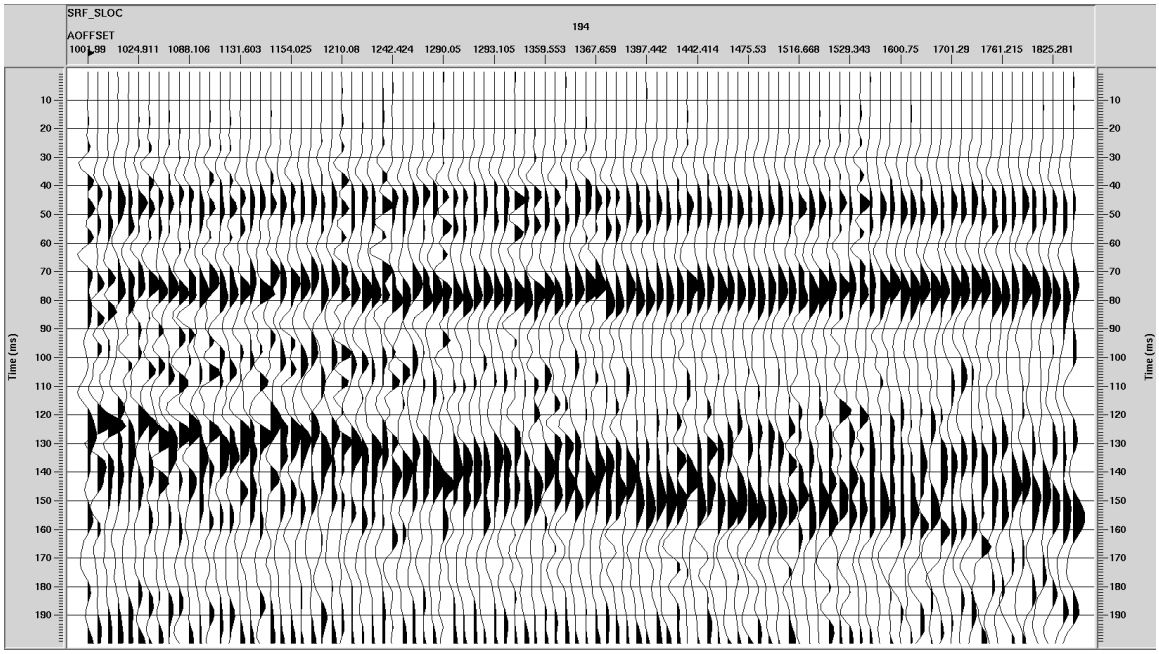

Figure 4.4 (continued).

After stacking the RFs for each receiver, I picked the time lags and spatially interpolated them to obtain P/S lag-time maps (Figure 4.5). The P/S time lags range from 25 ms to 60 ms and show a general decrease from the northeast to southwest of the study area during each of the acquisition years, and especially in 2002. In 2002, the variation of the P/S lags is substantially larger than in the preceding surveys. From the histogram of the time difference picks (Figure 4.6), one can see that compared with 1999, larger time lags were present in 2002, which were also mostly distributed within the eastern part of the survey area (Figure 4.5).

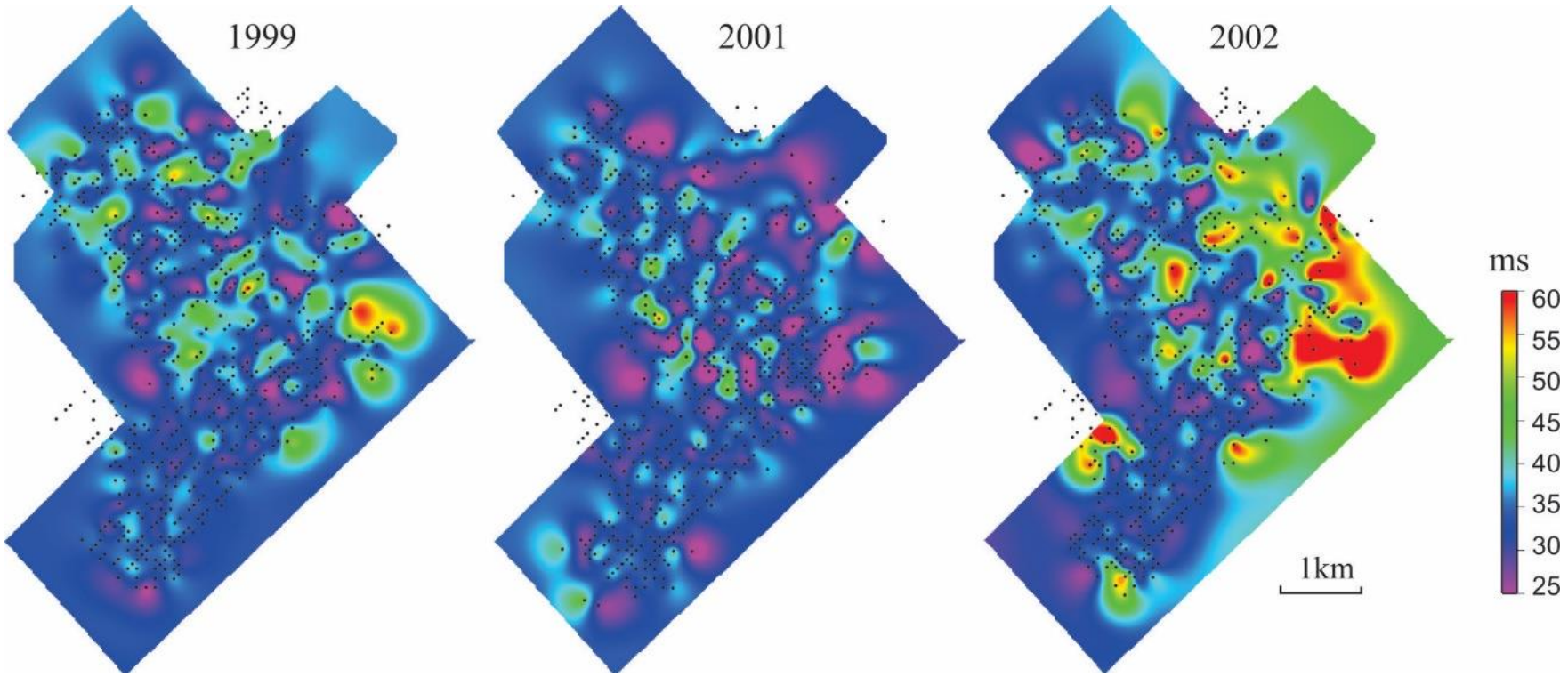

Figure 4.5. Time differences between P- and S-wave arrivals calculated by RF method in each year.

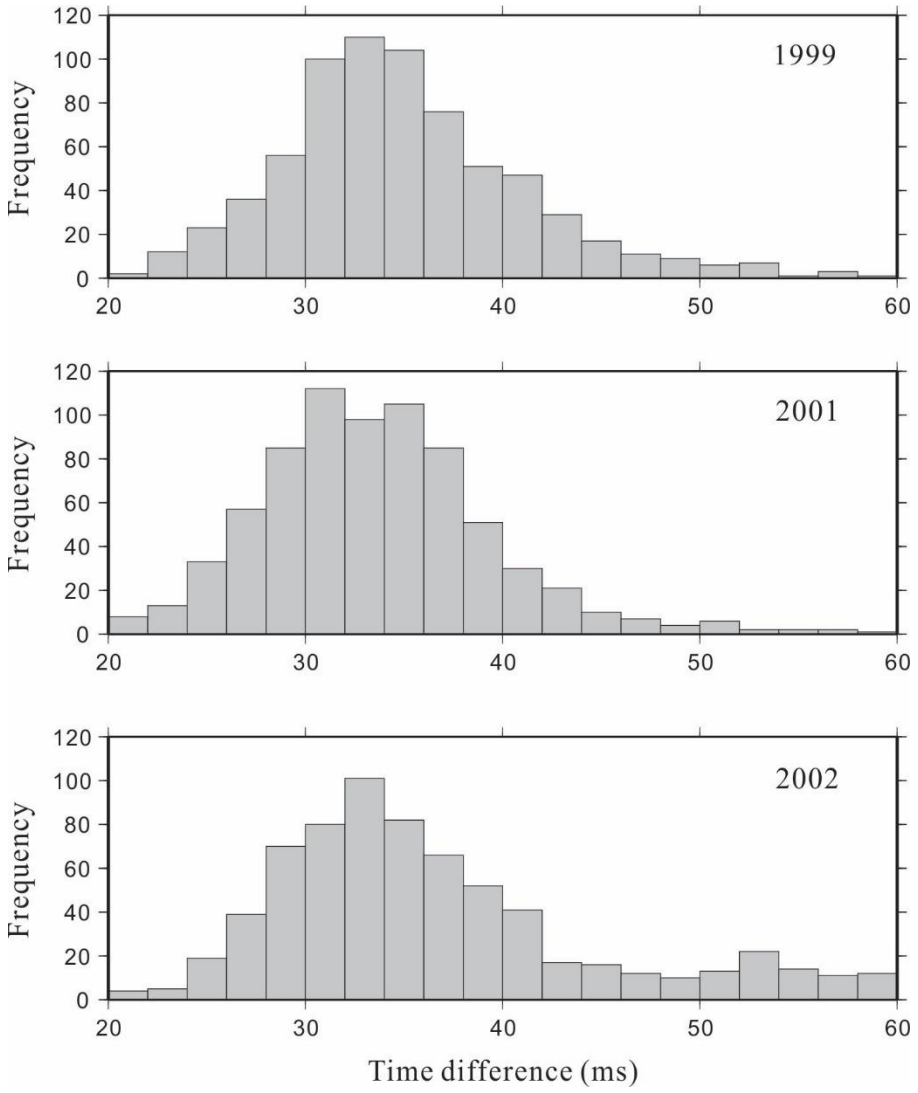

Figure 4.6. Histograms of reflection time differences for the three years of data.

4.3.3 Time-lapse variations of receiver functions

The P/S lag-time maps from the monitor datasets were further compared with the baseline survey (Figure 4.7). The total variations of the time lags between the surveys range from about -8 ms to 8 ms. The time lags of the monitor datasets in most of the

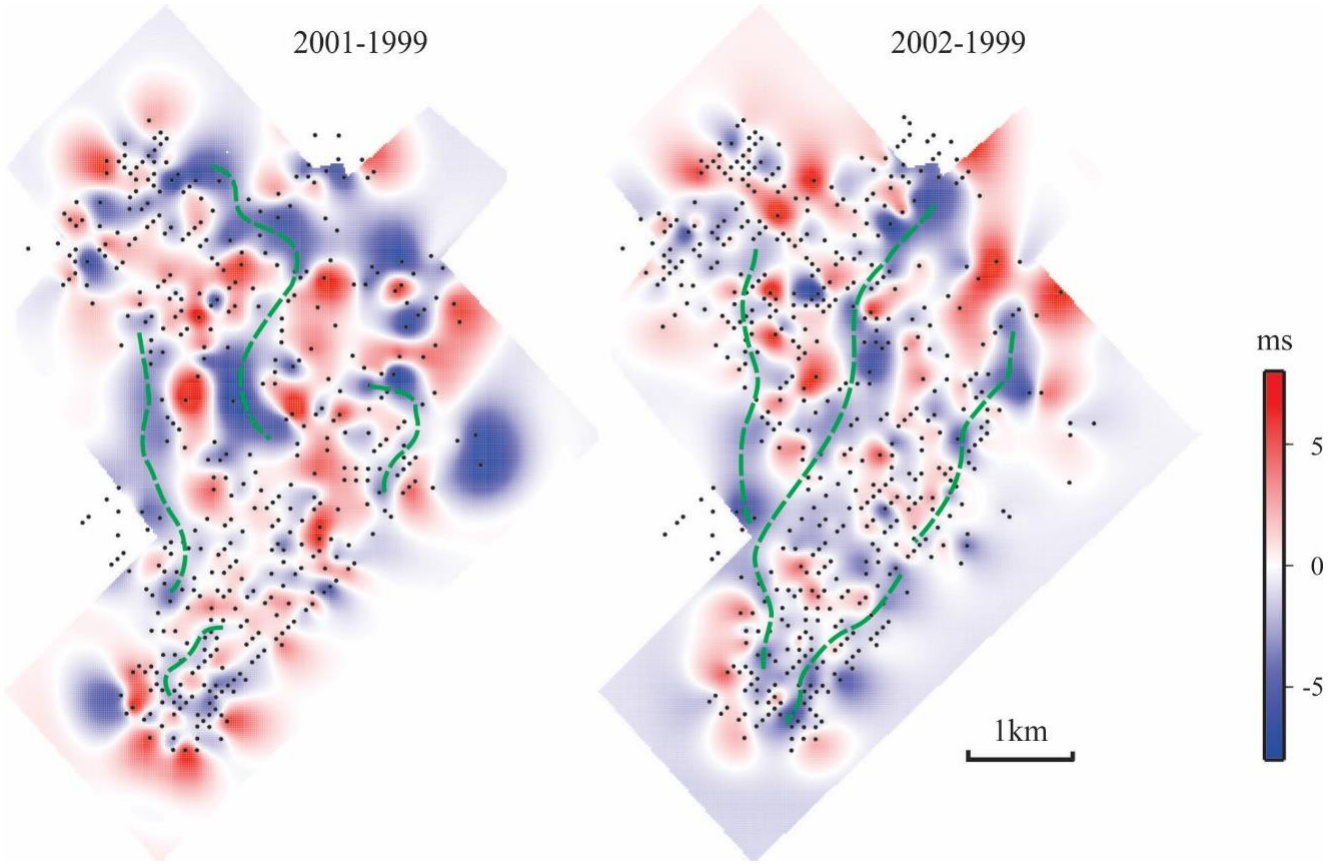

Figure 4.7. RF time-lag differences between monitor and baseline surveys (labelled). The green dashed lines indicate the interpreted channel-like shallow structures. The black dots are the actual picks on common receiver gathers.

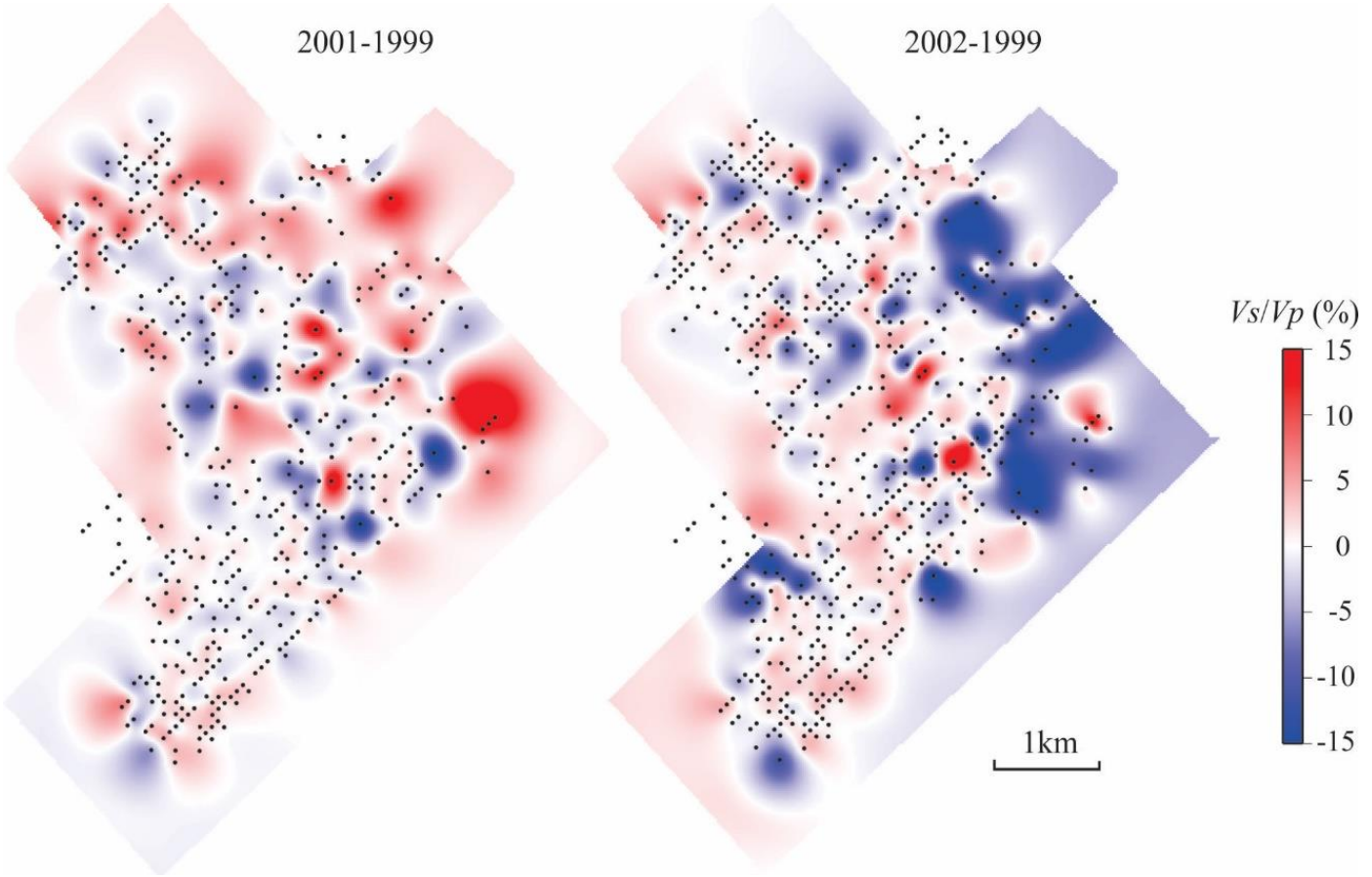

Figure 4.8. Relative V_S/V_P ratio variations between the baseline and monitor surveys (labelled). The black dots are the actual picks on common receiver gathers.

survey area are slightly reduced (by around 2 ms) relative to the baseline survey. These two maps also suggest several channel-like structures within the shallow subsurface (green dashed lines in Figure 4.7) with P/S lag times decreasing from the northwest to southwest. These structures appear especially prominent in the comparison of monitor 2002 to the baseline (Figure 4.7b).

Based on the time differences between the P- and S-wave arrivals and the known P-wave velocity (V_P) in the refraction model, I tried estimating the S-wave velocity (V_S) variations above the refractor. By inverting equation (4.2) for V_S, the estimated average S-wave velocity in the near surface is about 550 m/s. Because the temporal variations of V_P between the baseline and monitor datasets are corrected in the pre-stack calibration procedure (Chapter 2), I only present the variations of the V_S/V_P ratio between the baseline and monitors (Figure 4.8). From these maps, the V_S/V_P ratio varies by about ±15% between the different years of acquisition, with relatively increased ratios within the channels interpreted in Figure 4.7. This variation can likely be explained by variations of water content and the depth of the water table in the different years of acquisition.

The relation of V_S/V_P to the depth of the water table and generally water content within the subsurface is difficult to ascertain. On one hand, the shear-wave velocity is generally insensitive to water saturation, and therefore the observed variation of V_S/V_P could be caused by the variations of V_P. On the other hand, pore- and wave-induced fluid flows affect the attenuation of S waves. This attenuation should be strong in the near surface, and consequently it can cause wave dispersion and variations of S-wave

velocities (Meersman, 2013). Thus, a certain amount of shallow V_S variation could be attributed to changing water saturation during the different years of data acquisition

4.3.4 S-wave statics

From the perspective of P/S reflection imaging (which is outside of the scope of this Dissertation and still remains to be carried out for Weyburn 3-C dataset), an important application of the RF analysis could be in inferring the S-wave statics (van Manen et al., 2003). Figure 4.9 shows the S-wave statics derived by using equation (4.4) for each acquisition year of the Weyburn dataset. From these maps, the S-wave statics vary from 20 ms to 40 ms and show a decreasing trend from the northeast to southwest. In the 2002 dataset, some larger statics are also seen in the southeast corner, which are suggested by the larger P/S time lags in Figure 4.5. Unfortunately, converted-wave reflection imaging has not been performed for this dataset, and therefore these statics cannot be illustrated by a stacked image.

4.4 Conclusions

The receiver-function (RF) method is feasible and useful in land 3-C/3-D reflection seismic imaging as well as in time-lapse studies. Identification of converted-wave arrivals in the RFs leads to the measurements of the relative time lags between the P- and S-waves propagating within the near subsurface. Shallow S-wave velocities can be obtained by combining these time lags with P-wave velocities derived from refraction measurements. The resulting constraints on the near-surface S-wave structure allow improving the S-wave static corrections. By using independent RF measurements, the deviations of these statics from the conventional scaled P-wave statics can be detected.

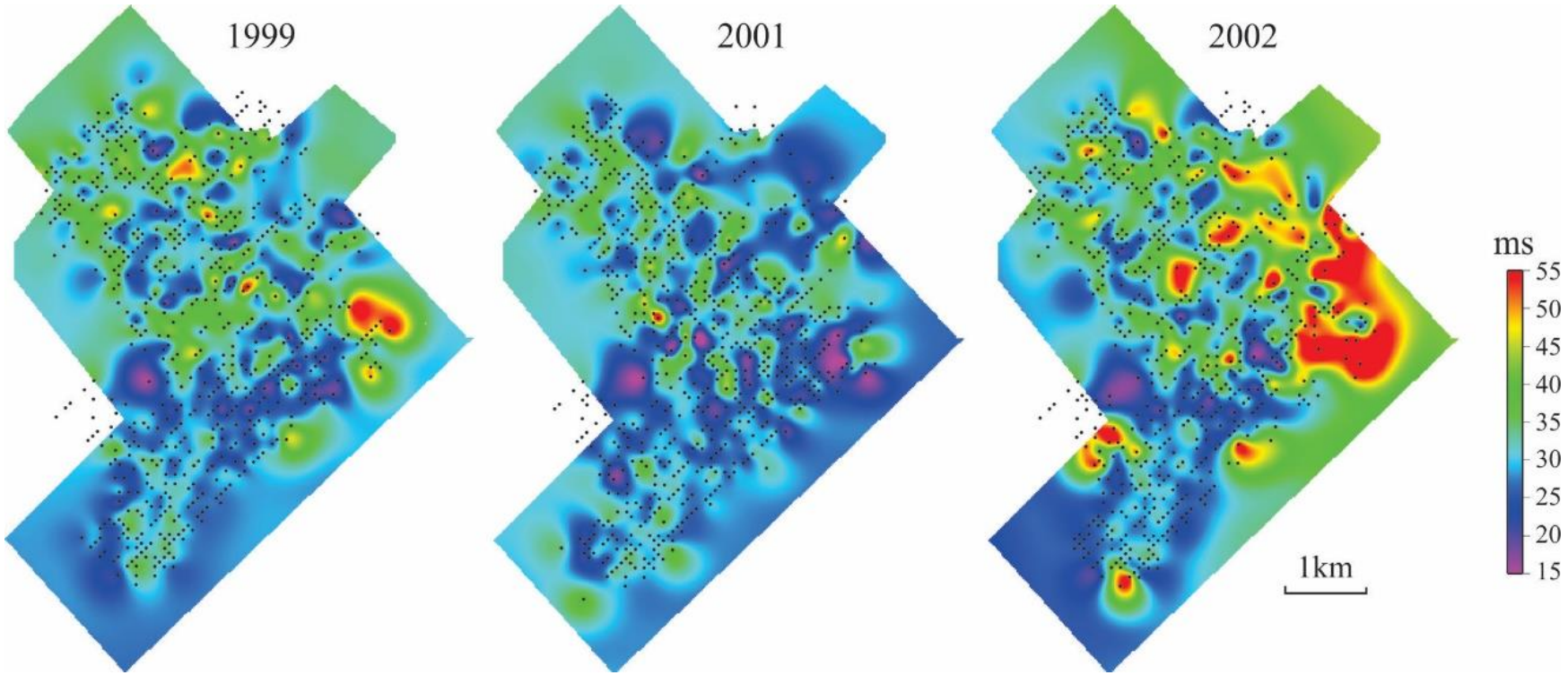

Figure 4.9. S-wave statics inferred for three vintages of the time-lapse dataset. Black dots are the actual picks on common receiver gathers.

In application to the Weyburn time-lapse reflection dataset, the time lags between the primary P and converted P/S waves are close to about 35 ms, which corresponds to the S-wave velocities of 550 m/s within the near surface. Spatial variations of the P/S time lags and V_S/V_P velocity ratios as well as their variations with time were mapped within the study area. The temporal variations are interpreted as related to changes in water content within the near surface affecting the P-wave velocities, and potentially to some degree S-wave velocities as well.

CHAPTER 5

SKELETONIZATION OF GEOPHYSICAL IMAGES

In this Chapter, I explore an approach to automated and quantitative interpretation of arbitrary attributes in 2-D images called “skeletonization”. Although this approach has been tried in several exploration and deep seismic applications, it is still quite new and little explored, particularly in non-seismic applications. This approach was perceived as having great promise for high-resolution AVA/AVO analysis in pre-stack seismic data from the Weyburn-Midale project and for automated detection of structural features in spatial attribute maps, such as studied in Chapter 3. Because of its general character, this approach is also very broad and should be applicable in numerous applications to 2-D gridded data. A brief overview of previous applications of skeletonization and its limitations, and also the general idea of the new approach are described in section 5.1.

Within the scope of the S-wave and AVO data analysis in this Dissertation, skeletonization is a relatively specialized approach aiming at mapping and interpreting maps of detailed AVO anomalies and detection of AVO trends in pre-stack seismic data. Within the limited time span allotted to this part of the project, only a “pilot” application of skeletonization to pre-stack seismic data has been completed and is reported here (subsection 5.3.3). Leading to this seismic application, a substantial development of the skeletonization technique was carried out by using 2-D potential-field images (sections 5.2 and 5.3).

The development and tests of the skeletonization approach in this Chapter is based on the following papers:

***Gao, L**. and Morozov, I., 2012, Skeletonization of Potential-Field and Seismic Images, Proceedings of 2012 CSPG/CSEG/CWLS Convention, Calgary, AB, Canada, p. 1-5, http://cseg.ca/assets/files/resources/abstracts/2012/117_GC2012_Skeletonization_of_Potential-Field_and_Seismic_Images.pdf, last accessed 20 Oct 2016*

***Gao, L**. and Morozov, I., 2012, Skeletonization of Magnetic-Field Images in Southeastern Saskatchewan and Southwestern Manitoba; in Summary of Investigations 2012, Volume 1, Saskatchewan Geological Survey, Sask. Ministry of the Economy, Misc. Rep. 2012-4.1, Paper A-3, 15p.*

As with all other papers in which I am the lead author, the contributions by my supervisor (I. Morozov) consisted in setting the problem, general direction, and providing guidance with writing software for integration of the codes in his seismic processing system IGeoS (Morozov, 2008). The above papers were merged, modified, and reformatted for inclusion in this Dissertation. The *Introduction* and *Method* sections also include material from an unpublished manuscript that I am currently preparing for *Geophysics*.

5.1 Introduction

Geophysical data are used to study the structure, composition, dynamic changes, and to provide reliable models of the Earth based on the principles of physics. Although using

different physical fields and models, many types of geophysical images, such as seismic sections and volumes, gravity and magnetic maps, possess a number of similar geometrical features. Those features can be expressed by linear continuity, branching, amplitudes, widths, polarities, orientations and/or other attributes and can be subdivided into "background trends" on top of which some kinds of "anomalies" or "wavelets" can be recognized. The spatial dimensions of geophysical images may also vary, ranging from the usual distances, elevations and depths. Automatic identification of such spatially-connected wavelets and measurement of their parameters is the general objective of the pattern-recognition process called "skeletonization".

The original development of the skeletonization technique targeted automatic event picking in reflection seismic data (Le and Nyland, 1990; Lu and Cheng, 1990; Li *et al*., 1997). In these approaches, pattern primitives, such as wavelet amplitudes, durations and polarities, were extracted from seismic traces and connected along the offset dimension according to certain similar features to form a coherent event. Starting from the stronger seismic events, weaker events were identified and connected iteratively. This technique was based on the binary consistency-checking (BCC) scheme by Cheng and Lu (1989); however, the use of any particular ranking scheme is not important for skeletonization. More recently, Eaton and Vasudevan (2004) extended this method to aeromagnetic data by using detection on the basis of strike direction, event linearity, event amplitude and polarity. Since this algorithm was derived from previous skeletonization approaches used in seismic processing, Eaton and Vasudevan (2004) processed 2D images in two passes, with the first pass interpreting the X axis as "reflection time", and in the second pass placing the "time" along the Y axis. In addition,

seismic geophysical skeletonization approaches are limited to near-zero mean wavelets, which is a significant limitation for the more general applications such as AVO. Even in reflection seismic records, a low-frequency background can thwart feature extraction and cause disruptions in the "skeleton". Pre-filtering of the image prior to event detection could also be undesirable as this could complicate processing and cause the loss of information about the background trends.

Another important drawback of seismic-algorithm based skeletonization is the reliance on a preferred (time) direction. Although applications of this algorithms to potential-field grids were described by Eaton and Vasudevan (2004), these applications were achieved by making two passes of processing, first by treating the *Y* direction (north) as the "time" and second by transposing the grid and treating the *X* direction (east) as the "time". Thus, the structural features within the image were still detected in only two orthogonal directions. This detection scheme is non-uniform azimuthally and may be biased toward the gridlines of the images, resulting in potential "footprints". In addition, the basic wavelet used by Eaton and Vasudevan (2004) is of a near-zero mean, bipolar "seismic" type, consisting of a peak followed by a trough. This wavelet may be well suited for certain types of magnetic sources (such as dipping magnetic sheet) but it appears to be too specific for general feature detection that may be encountered, for example, in AVA attribute analysis.

In this Chapter, a new approach opposite to that by Eaton and Vasudevan (2004) is taken, and a skeletonization technique is developed for arbitrary two-dimensional (2-D) gridded data. Seismic (pre- or post-stack) records are only considered as special cases of such grids, with specific treatment of the time dimension and also additional constraints

and attributes. While achieving the same general goals of quantitative recognition of linear features in gridded images, this technique is highlighted by the following properties: 1) feature detection performed isotropically, at a continuous range of azimuths (or time-distance moveouts if the image is a seismic section); 2) several new features, such as extraction of orientation angles and background-trend level, are used to meet the complexity of the data; and 3) a more flexible event detection scheme is used instead of the BCC method. In addition, skeletonization is combined with empirical mode decomposition (EMD) (Morozov, 2009), which allows focusing on different-scale structures and exploring them for multiple attributes and purposes.

5.2 Method

Similarly to the previous approaches (e.g., Eaton and Vasudevan, 2004), skeletonization in the present method is achieved in two general steps: 1) identification of elementary "wavelets" in gridded images, and 2) connection of these wavelets to form the "skeleton" of the image. In seismic cases, the skeleton can be interpreted as a set of "horizons", and in the potential-field case, it comprises any "lineaments" (elementary linear and potentially branching features) detected in the image. Each of these "lineaments" is associated with a set of parameters referred to as the "feature set" and can be interconnected with other "lineaments".

5.2.1 Wavelet Detection and Feature Extraction

Starting from a grid of "seed" points located on the vertical and horizontal cross sections, wavelets in the 2-D grid are identified as combinations of one or two amplitude deviations from the background trend level (Figure 5.1). These deviations are referred to

as “humps” here. From each seed point, the humps are first searched within the cross-section line, and then their final locations and orientation azimuths are determined by minimizing the cross-sectional sizes (distance AB in Figure 5.1a). With the new option of subtracting the slow-varying trend, the humps are identified even on top of a slowly varying amplitude background (long-dashed grey line in Figure 5.1b). Several options are available for the wavelet-extraction algorithm. In particular, waveform edges may be identified by their amplitudes passing through the smoothed background level (points A and B in Figure 5.1) or by using zeros of second derivatives of the signal. These options may be useful in the presence of strong-background (as common in magnetic data) or short-wavelength noise in the records.

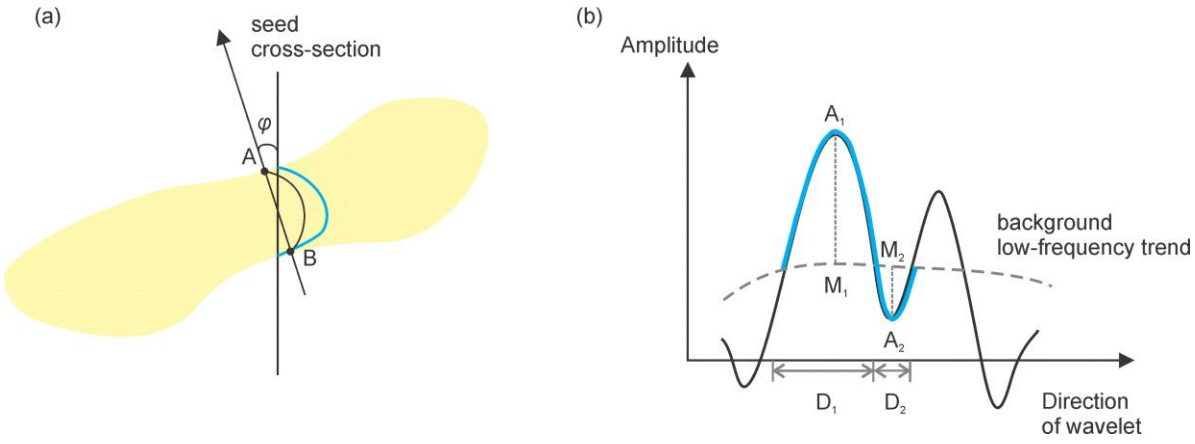

Figure 5.1. Wavelet extraction: (a) Extraction of an anomaly (yellow) from a seed cross-section (black line). AB is the minimal cross-sectional size, and azimuth is defined as the angle of the shortest cross-section across the anomaly; (b) Identification of wavelet attributes. Blue line is the extracted wavelet. A_1 and A_2 are the peak and trough amplitudes, respectively; M_1 and M_2 are the background amplitudes; D_1 and D_2 are the widths of the peak and trough.

Once the wavelets are isolated, their polarities and spatial directions are determined

by comparing the two humps within them (similar to Eaton and Vasudevan, 2004) or also by comparing the amplitudes of adjacent wavelets. "Undefined" values of polarities are also allowed where they cannot be determined consistently.

For subsequent pattern analysis, the wavelets are characterized by their peak or trough amplitudes (A_1 and A_2), widths (D_1 and D_2), orientation angles (φ), background levels and polarities (P; Figure 5.1b). Combinations of these parameters represent the desired feature sets:

$$f = \left(A_1, A_2, D_1, D_2, M_1, M_2, \varphi, P\right). \tag{5.1}$$

5.2.2 Wavelet connections

After all wavelet features are determined, they are spatially connected to form the skeleton. This process is started from either: 1) wavelets manually picked by the user or 2) the largest amplitudes. First, each selected wavelet is connected to several adjacent wavelets according to the lowest connection costs. The cost function for connection is designed to evaluate the similarity of two wavelets. For example, for humps *A* and *B*, the cost function is (Figure 5.2):

$$Cost(A,B) = \left(\mathbf{r}^A - \mathbf{r}^B\right)^2 + \sum_i w_i \left(f_i^A - f_i^B\right)^2, \tag{5.2}$$

where $\mathbf{r}^A$ and $\mathbf{r}^B$ are the spatial coordinates, $\mathbf{f}^A$ and $\mathbf{f}^B$ are the corresponding feature vectors (5.1), and w_i are some empirically-determined weights.

Among all pairs of potential connections, optimal triplets are further identified. For example, for wavelet B in Figure 5.2, several candidates for adjacent connections *A* and *C* are considered based on the orientation angle, φ. Among these candidates, the optimal

pair is found by minimizing the following connection-cost function:

$$Connect(A,B,C) = \left(Cost(A,B) + Cost(B,C)\right) \times \text{cross-correlation}\left(\text{interp}\left(B\right),B\right), \quad (5.3)$$

where interp(B) (blue line in Figure 5.2) is the feature set (wavelet) interpolated at location B by using wavelets A and C. The interpolation is based on the mutual cost functions for pairs of wavelets, *Cost(A,B)* and *Cost(B,C).* Note that this triplet connection scheme does not use the somewhat arbitrary Euclidian distance and area-of-triangle principles used by Li and Vasudevan (1997) but measures the similarity of wavelets directly by their zero-lag cross-correlation (Figure 5.2).

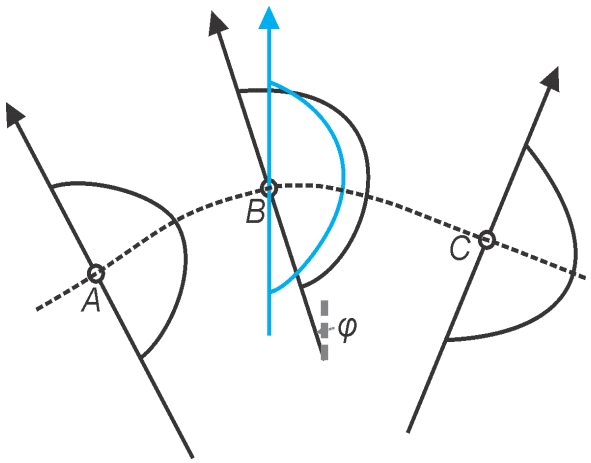

Figure 5.2 Horizon connection. Wavelet A and C are interpolated at the location of B (blue) and cross-correlated with wavelet B. Dotted line is the connection being tested for optimality.

5.2.3 Empirical Mode Decomposition

Prior to identifying the wavelets and features in a 2-D image, it is useful to decompose the image into components containing different scale-lengths. Such decomposition can be performed by a process called Empirical Mode Decomposition

(EMD; Hassan, 2005). The EMD is in an iterative procedure that sequentially extracts 1-D or 2-D dependences called "empirical modes" from the data. In a one-dimensional case, starting from a data record, $u(x)$, the first empirical mode $u_1(x)$ and its residual $r_1(x)$ are determined:

$$u(x) = u_1(x) + r_1(x), \tag{5.4}$$

and the residuals are further decomposed recursively (n = 1,2…):

$$r_n(x) = u_{n+1}(x) + r_{n+1}(x). \tag{5.5}$$

When the coordinate x is the time and $u_n(x)$ are time series, Hilbert transform is used in these equations to extract the "upper" [$E_u(x)$] and "lower" [$E_l(x)$] envelopes of the signal, and the corresponding n-th empirical mode $u_n(x)$ is defined as their average (Hassan, 2005):

$$u_n(x) = \frac{1}{2}\left[E_u(x) + E_l(x)\right]. \tag{5.6}$$

This operation produces a low-frequency signal following the averaged trend of $u(x)$. However, this procedure only works for oscillatory signals such as seismic waveforms, for which $E_u(x)$ and $E_l(x)$ are always positive, and negative, respectively. In 2D, and particularly for potential-field data with a significant background trends in large areas, this assumption fails, and the Hilbert transform does not allow obtaining consistent $E_u(x)$ and lower levels $E_l(x)$ bracketing the signal.

To overcome the above difficulty, Morozov (2009) proposed a simple new type of EMD bypassing the use of Hilbert transform. This procedure is applicable to an

arbitrary number of spatial dimensions. Instead of eq. (5.6), the nearest empirical mode is defined as:

$$u_n(x) = F_k[r_{n-1}], \tag{5.7}$$

where $F_k[\ldots]$ denotes low-pass filtering with cut-off wavenumber k. Starting from $k = 0$ (with $n = 1$), the value of k is gradually increased until the average amplitude of u_n exceeds a small portion (e.g., 5%) of the amplitude or r_{n-1}. This iterative procedure achieves the goals of EMD by effectively constructing a series of band-pass filters in wavenumber k, so that each filtered component (except the original one with $n = 0$) contains an approximately equal portion of energy. As required by the EMD principle, the decomposition of the 2-D signal is controlled only by the signal itself and performed isotopically, i.e. independently of the orientations of the axes of the grid.

5.3 Results

In this section, several examples of potential-field and seismic data are used to illustrate the usefulness of skeletonization and its use with EMD algorithms.

5.3.1 Magnetic-field data examples

First, let us consider examples of regional gridded magnetic-field data from southeastern Saskatchewan and southwestern Manitoba (Gao and Morozov, 2012). The study area for this example analysis extends from W96º to W106.3º and from N49º to N56º (Figure 5.3). Figure 5.4 shows aeromagnetic data obtained from Natural Resources Canada after basic pre-processing and reduction to the pole. In this and other images, the major geologic structures and geographic references can be identified by comparing to

Figure 5.3. In NE parts of this and the following figures, long “wiggly” lines show the edge of the exposed Canadian Shield.

On top of the magnetic grid, Figure 5.4 shows the results of skeletonization using this raw grid with spatial demeaning within a 30-km sliding spatial 2-D window. Coloured circles indicate the picks of major features and black lines indicate linear anomalies connecting the features (the skeleton). The identified anomalies are indicated by circles with sizes proportional to the absolute values of demeaned amplitudes. Colours of the circles correspond to the orientations of the anomalies, defined as the directions in which the cross-sections of the anomalies are the most compact. These angles are thus always oriented across the structure and measured from the eastward direction to the North (upper colour palette in Figure 5.4). As this Figure shows, skeletonization identifies numerous linear elements of the structural fabric of the region, even those which can hardly be recognized visually from the original grid. However, many “seed” picks remain disconnected (looking like isolated dots in Figure 5.4) because of the strong regional bias in the amplitudes in this raw map.

Figures 5.5 through 5.10 show decompositions of the magnetic grid into several “modal” fields by using the 2-D EMD technique described in the preceding section (Morozov, 2009). These modes represent results of progressive low-pass filtering, so that each mode represents a certain spatial scale length, and the sum of all modes again reproduces the original field in Figure 5.3. Each of these empirical-mode images is also skeletonized in a way similar to shown in Figure 5.3. In these EMD-filtered images, note the dominant linear trends of picked events, which are mostly SW-NE in the northern parts of the images and NW-SE in the southern areas.

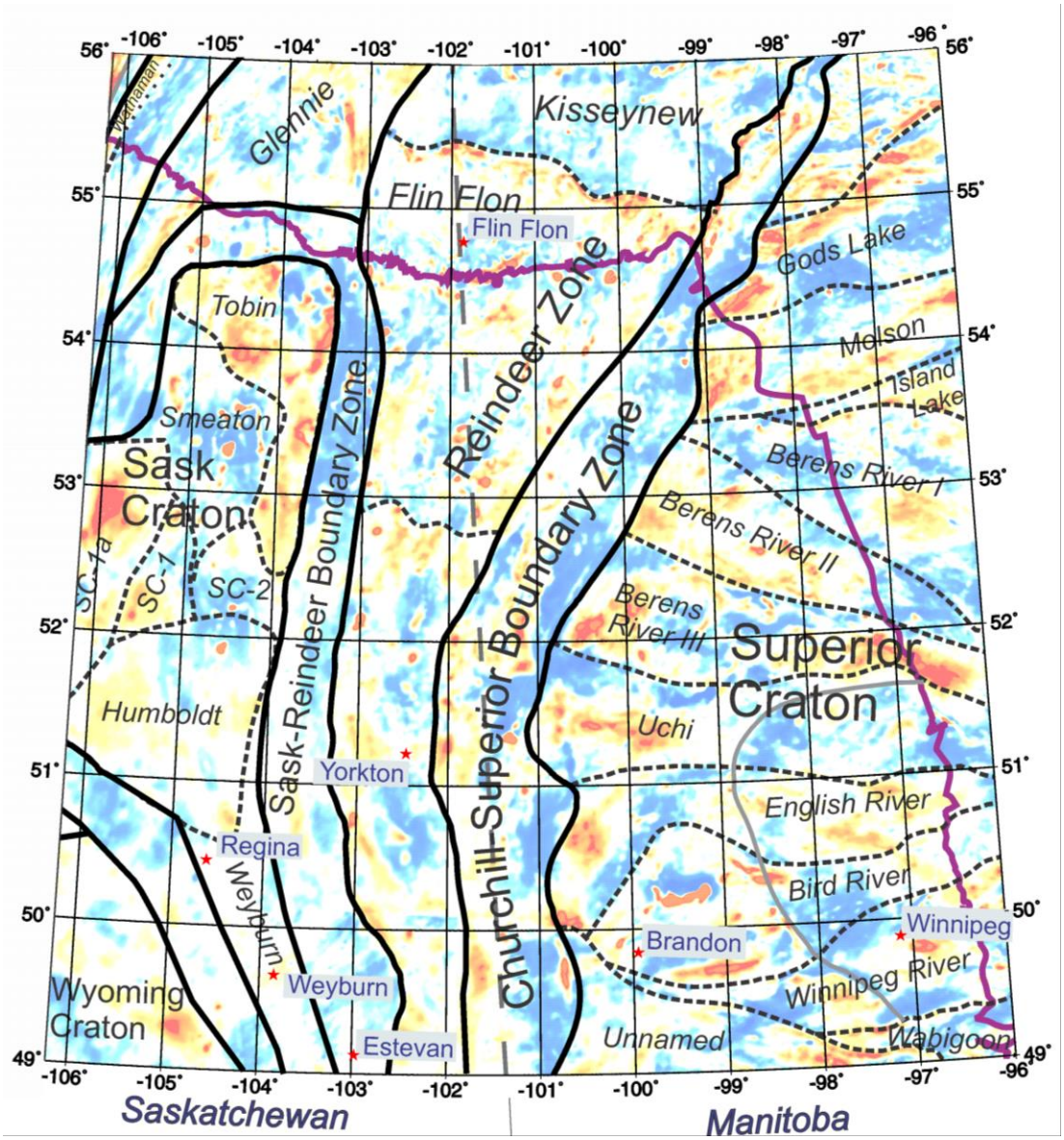

Figure 5.3. Study area in potential-field skeletonization examples. Purple line shows the edge of the exposed Canadian Shield. Labels indicate names of structural domains, red stars indicate several major cities. Colour background is the raw magnetic anomaly.

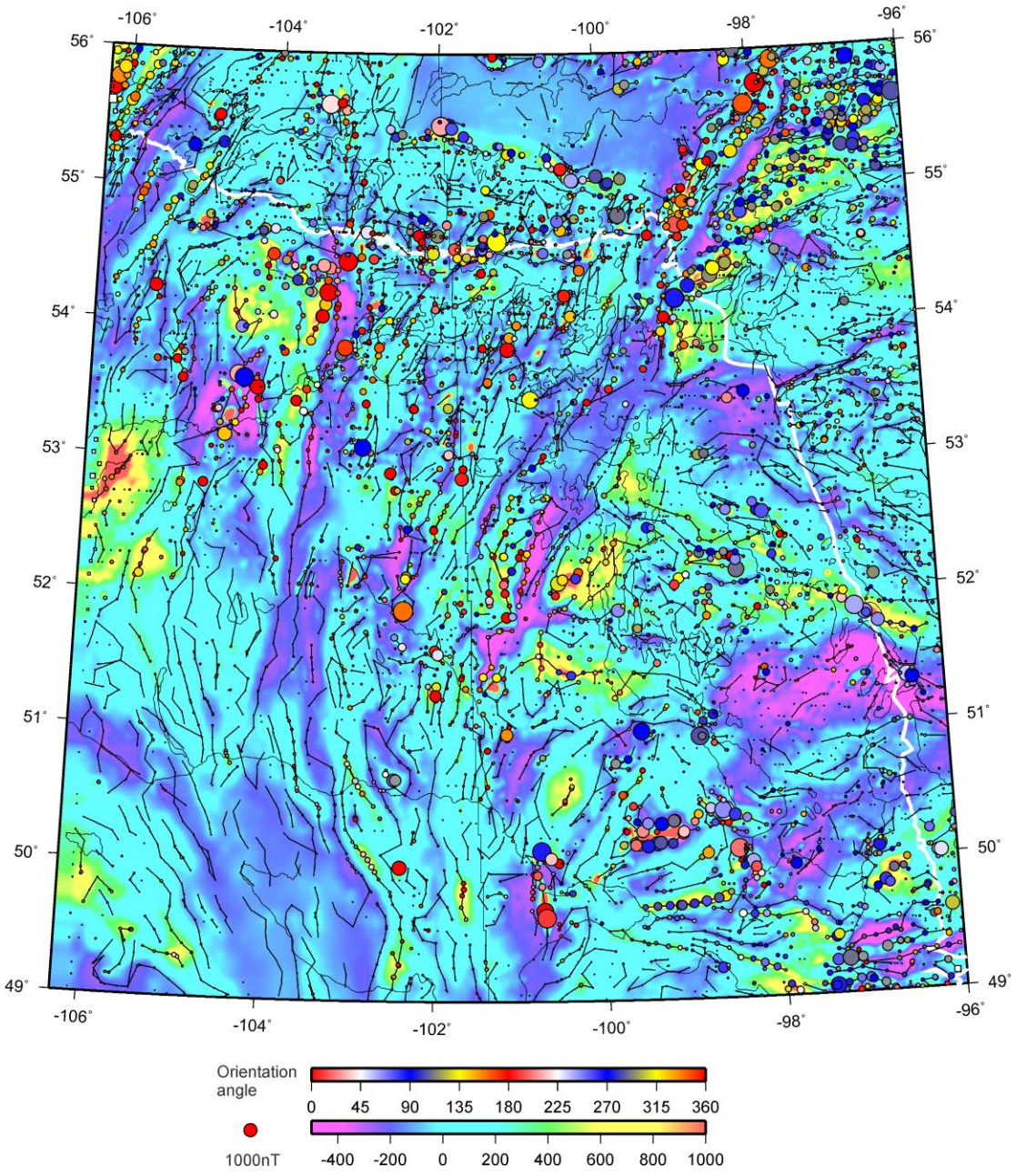

Figure 5.4. Aeromagnetic map of southern Saskatchewan and SW Manitoba with the results of skeletonization. See text for explanations of the lines and symbols. Lower colour palette refers to the grid, upper palette gives the orientation angles of anomalies (coloured circles).

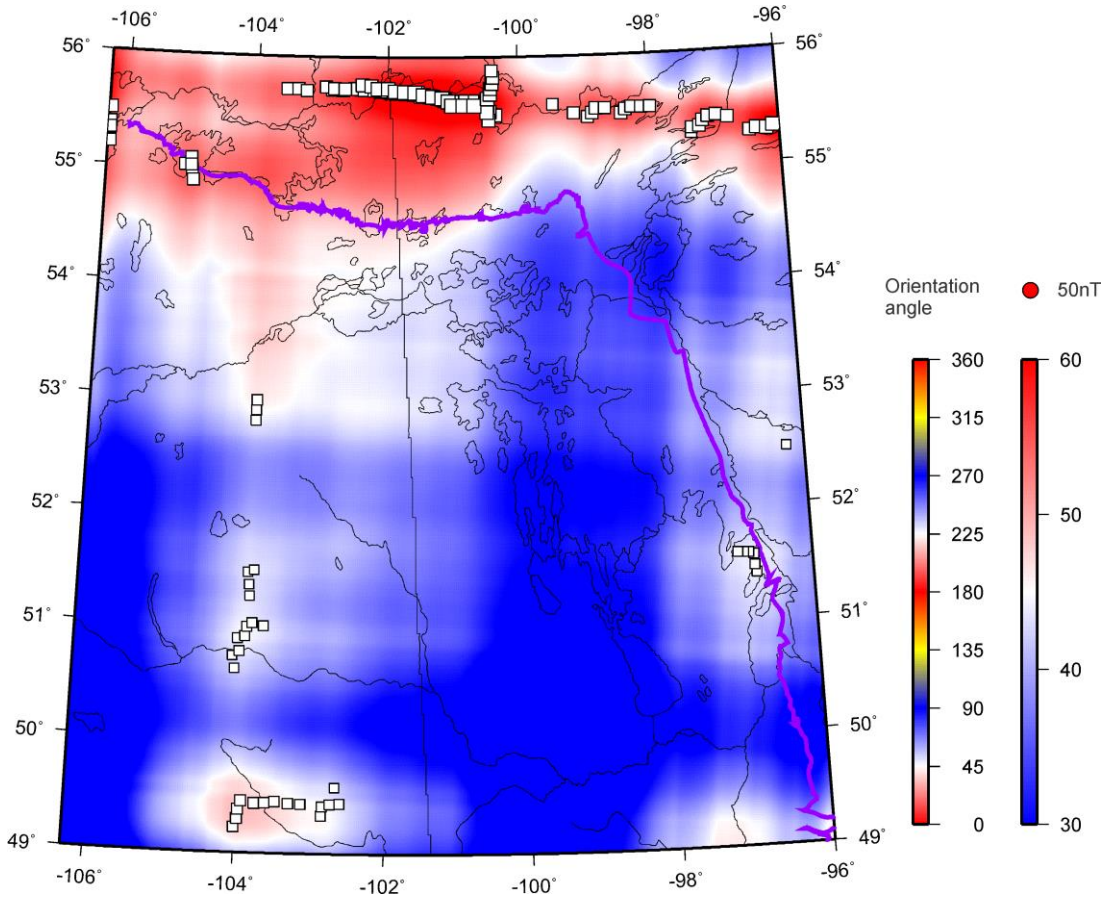

Figure 5.5. Component n = 1 of the Empirical Mode Decomposition of the magnetic field in study area and its "skeleton". Symbols and colour palettes as in Figure 5.3. The orientation angles of anomalies do not present on this figure.

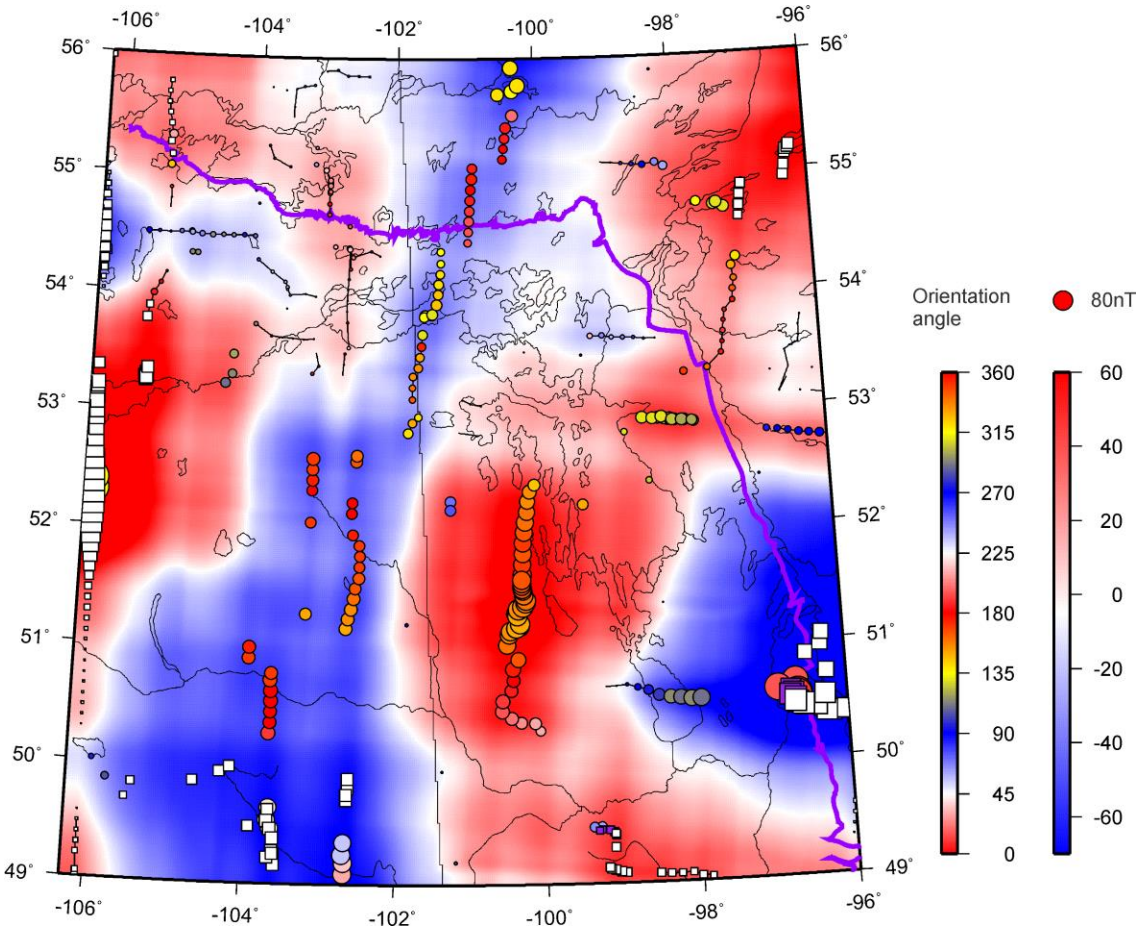

Figure 5.6. Component n = 2 of the Empirical Mode Decomposition of the magnetic field in study area and its "skeleton". Symbols and colour palettes as in Figure 5.3.

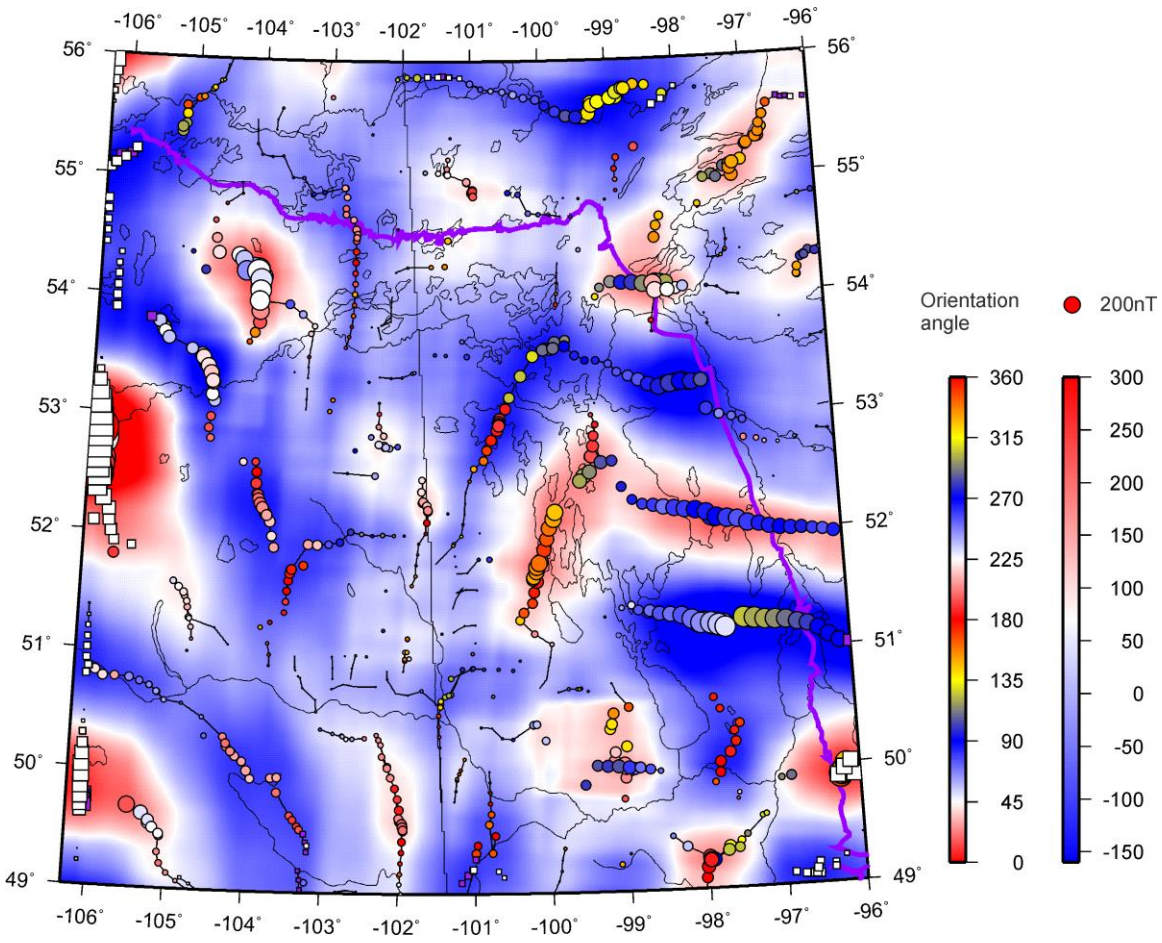

Figure 5.7. Component n = 3 of the Empirical Mode Decomposition of the magnetic field in study area and its "skeleton". Symbols and colour palettes as in Figure 5.3.

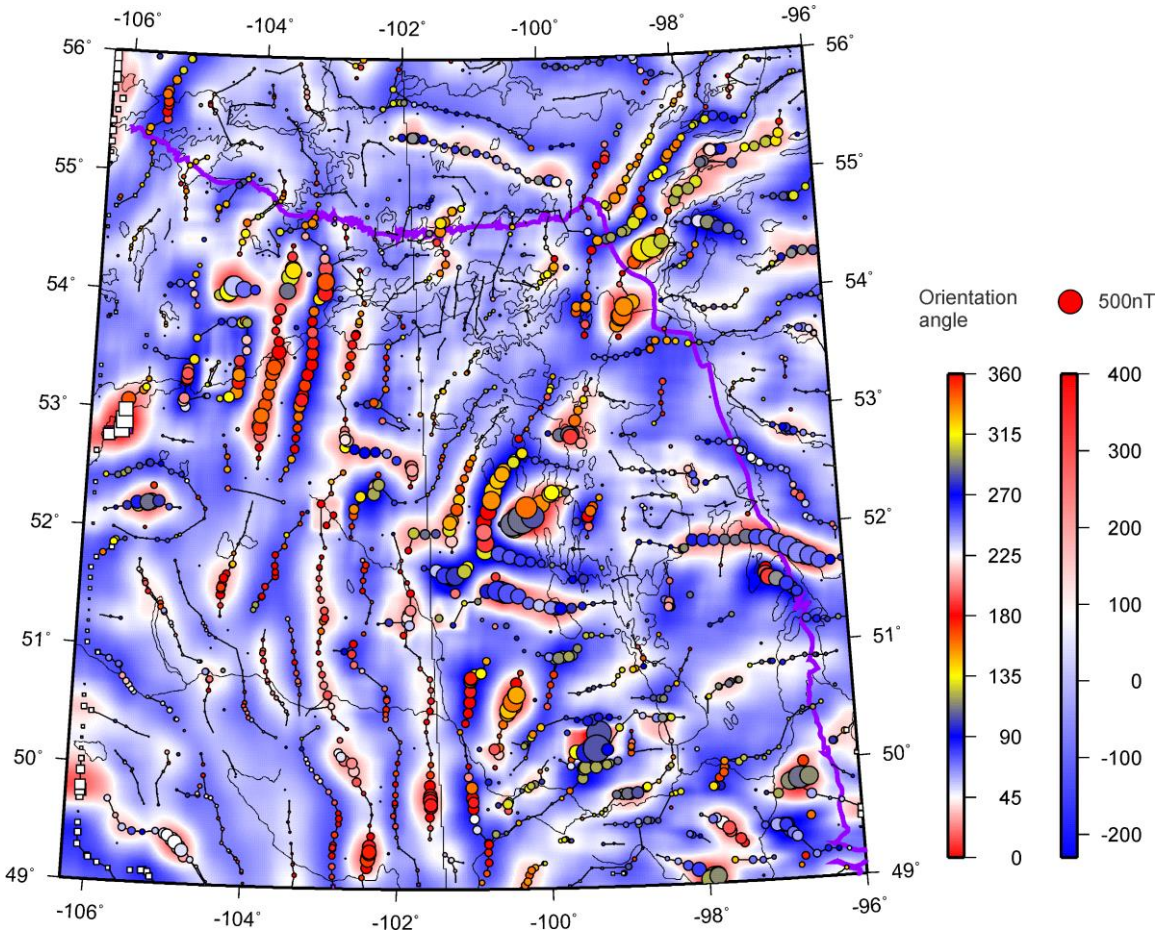

Figure 5.8. Component $n = 4$ of the Empirical Mode Decomposition of the magnetic field in study area and its "skeleton". Symbols and colour palettes as in Figure 5.3.

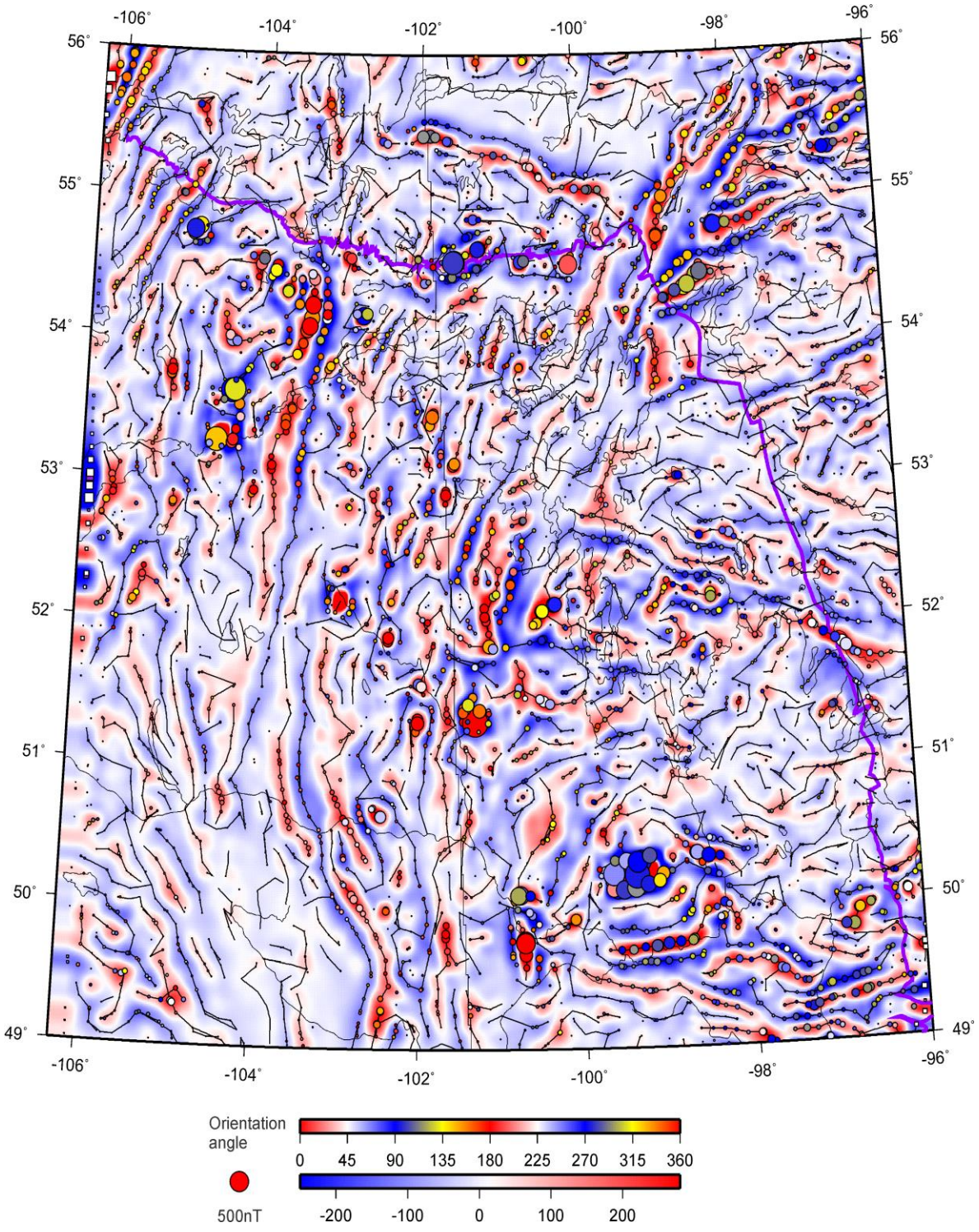

Figure 5.9. Component n = 5 of the Empirical Mode Decomposition of the magnetic field in study area and its "skeleton". Symbols and colour palettes as in Figure 5.3

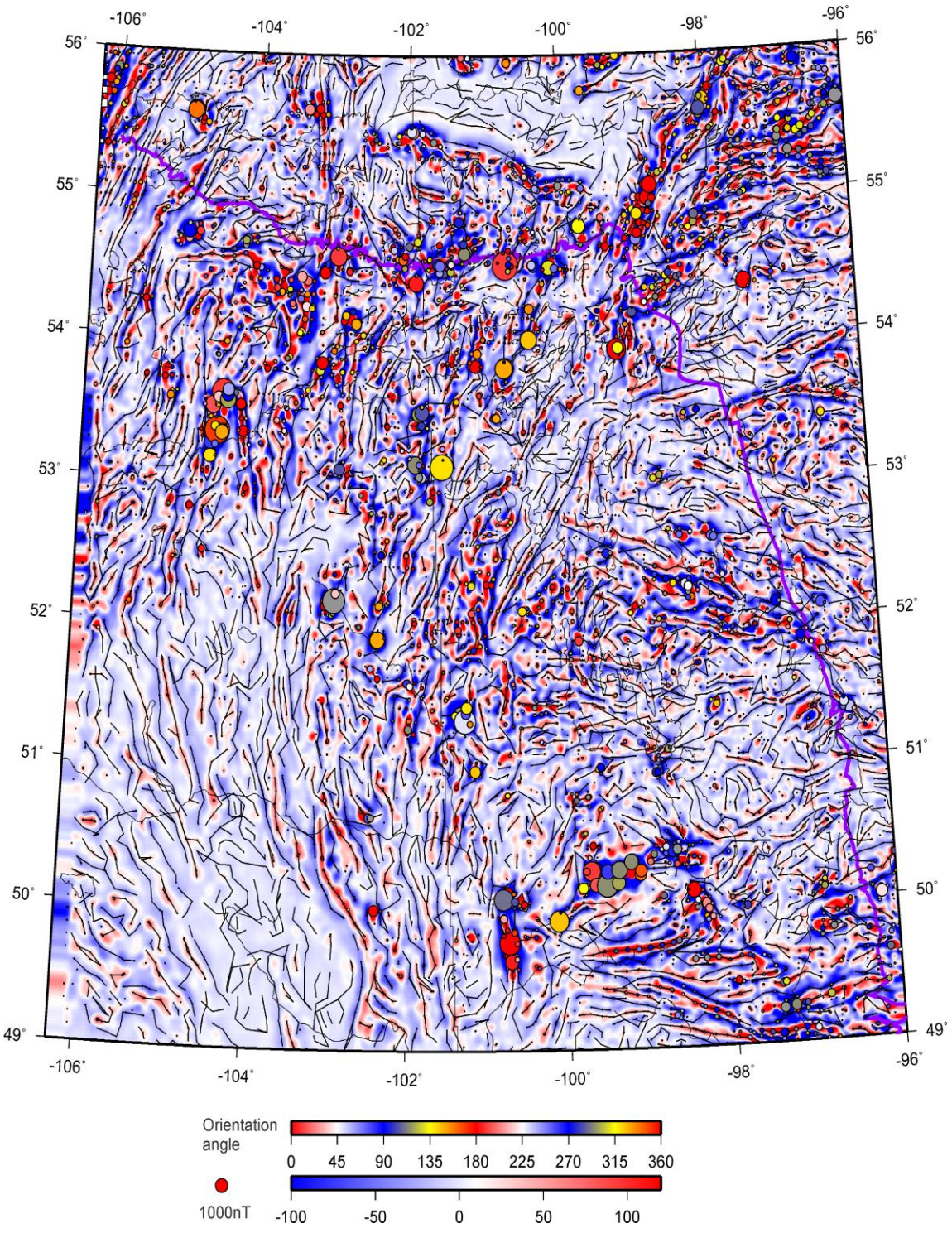

Figure 5.10. Component n = 6 of the Empirical Mode Decomposition of the magnetic field in study area and its "skeleton". Symbols and colour palettes as in Figure 5.3.

The “skeletons” of the images also include the amplitudes of the anomalies, which are indicated by the sizes of coloured circles in these Figures. Purple circles are anomalies of negative “polarities” (*i.e.*, proximities to other anomalies of lower magnitudes; Eaton and Vasudevan, 2004), and white squares indicate the anomalies to which no definite polarities were assigned.

Interestingly, the lowest-order empirical modes (Figures 5.5 and 5.6) are dominated by major structures striking in N-S and E-W directions. These directions indicated the large-scale structure and are not related to the time sampling. Relatively few “skeleton” picks are made in these modes, one per each cross-section of a large anomaly. In lower-order modes (Figures 5.7 and 5.8), notable criss-crossing trends are present, one following the Sask-Reindeer and Churchill-Superior Boundary Zones, and the other nearly orthogonal to it within the Superior Craton. Shorter-scale modes (Figures 5.9 and 5.10) show the greatest detail both before and after skeletonization.

The skeletonized EMD images are convenient for refining the boundaries of geologic domains and sub-domains. Figure 5.11 shows EMD component with $n = 6$ (highest-resolution) superimposed over the boundary delineation by Li and Morozov (2007) (also shown in Figure 5.3). Generally, the identified boundaries match with the contours of this empirical mode, although in some areas contradictions are found, such as indicated by question marks (Figure 5.11). Placement of block boundaries in such areas may likely need to be revisited in more detailed studies in the future, possibly with the use of the obtained image skeleton and using additional attribute maps derived from gravity and aeromagnetic data (Li and Morozov, 2007).

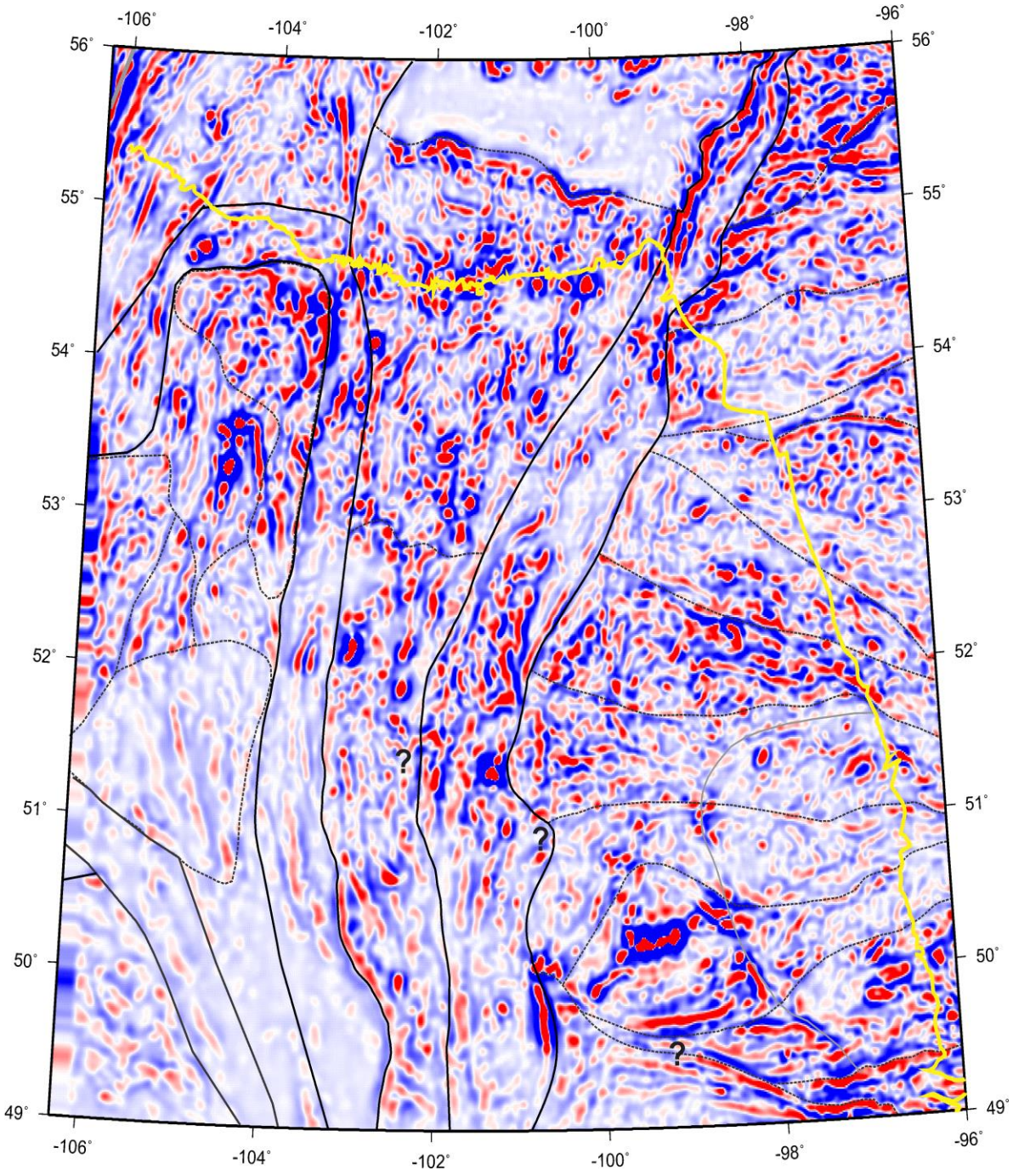

Figure 5.11. Comparison of EMD mode n = 6 with domain and sub-domain boundaries in Figure 5.3.

Once the image is decomposed into wavelets, features extracted and the skeleton created, its spatial attributes can be analysed in many ways. Figure 5.12 shows the skeleton images filtered by the lengths and angles of its near-linear features. Note how the lengths and orientations of near-linear features vary for different parts of the study area.

Rose diagrams in Figure 5.13 summarize the strike directions for the linear anomalies picked from three different scales of the EMD. As noted above, lineations striking at about N-S and E-W directions dominate these images. In Figure 5.14, I also show the azimuthal distributions of the features detected in the highest-resolution EMD component $n = 6$ for three areas: (W96º –106.3º, N54º –56º), (W102º –106.3º, N49º–54º), and (W96º–102º, N54º–56º), indicated by labels (a)-(c) in Figure 5.12. As Figure 5.14 shows, the first of these areas is heavily dominated by lineations striking at ~10º and ~70º south of the eastward direction; in the second area, the lineations are almost N–S, and in the third, they are dominated by the E–W direction.

5.3.2 Gravity data example

For an example of application of skeletonization to gridded gravity data, the study area is the same as for magnetic data examples (Figure 5.3). Similarly to the preceding Figures, Figure 5.15 also reveals dominant linear structural trends, which are SW-NE in gravity measurements are complementary to magnetic, and consequently the features detected in its skeleton could represent useful additional contribution to joint interpretation of the basement structure in the study area (Li and Morozov; 2007).

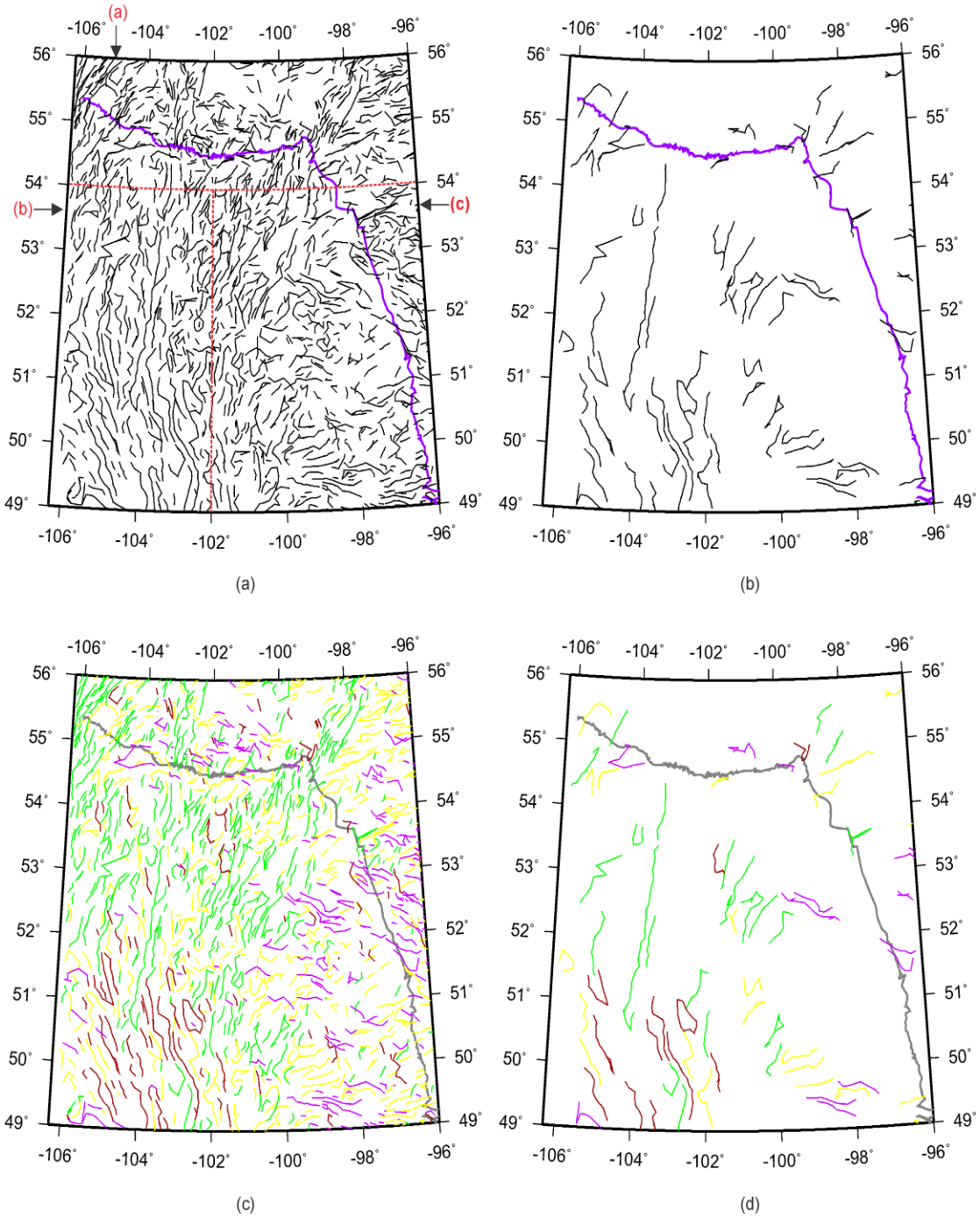

Figure 5.12. Skeleton maps filtered by different length and orientations of linear features: a) all lines (grey) from the raw image in Figure 5.4; b) features longer than 80-km in lengths; c) linear features coloured differently for three orientation directions: 50º–90º(green), 280º–300º(red) 320º–360 º(purple), and all other directions (yellow); d) lines as in c) longer than 80-km length.

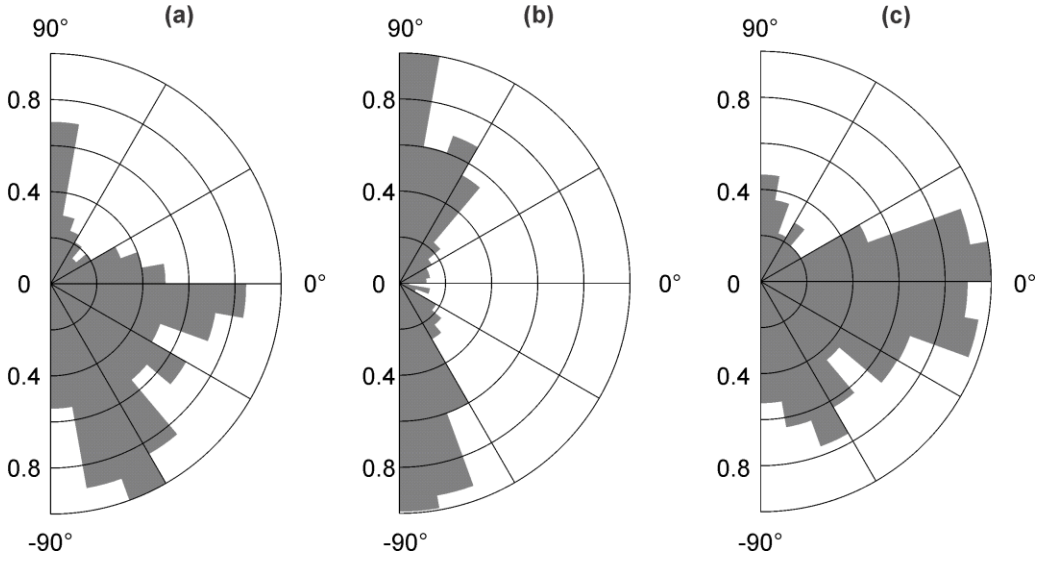

Figure 5.13. Rose diagrams for strike directions within three empirical modes: a) Component $n = 4$ (Figure 5.8); b) Component 5 (Figure 5.9); c) Component 6 (Figure 5.10)

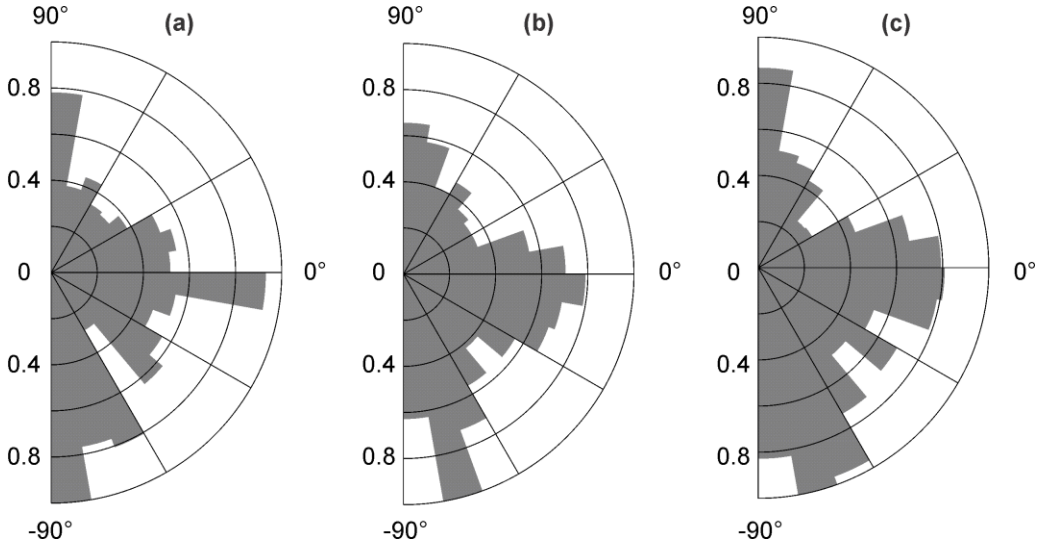

Figure 5.14. Linear-feature strike directions for three different geological areas extracted from component 6 of EMD. The areas are shown by rectangles in Figure 5.12.

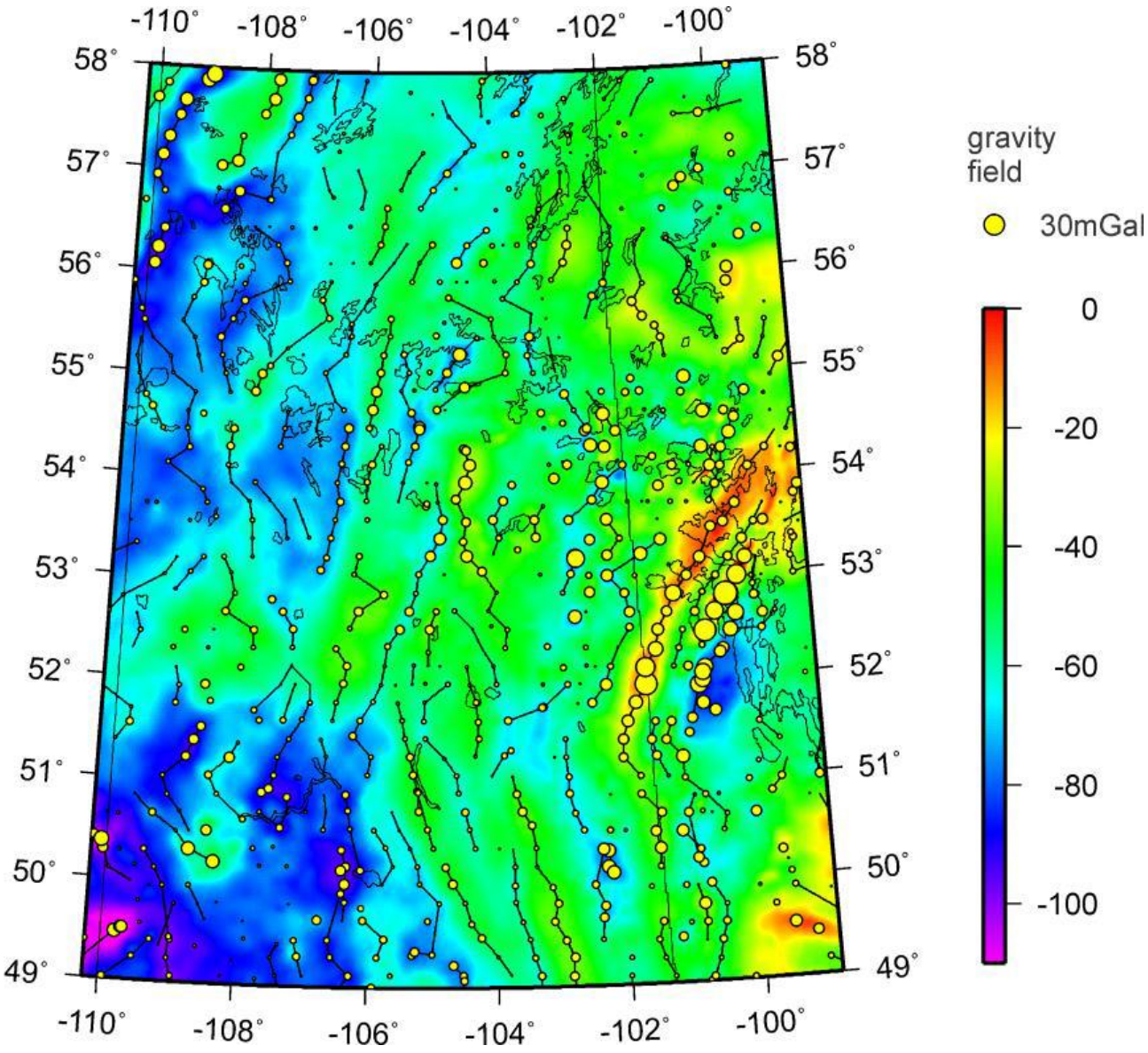

Figure 5.15. Skeletonization of regional gravity data. The lines are connections between the identified features. Circle sizes indicate the amplitudes of the anomalies. Yellow circles indicate positive-polarity and the purple indicates the negative polarity.

the northern parts of the images and NW-SE in the southern areas. The "skeleton" of the image also contains positive anomalies, which are indicated by the sizes of circles plotted in this figure. Due to a different physical nature of the gravity field (unipolar character and slower decay with distance from the source), the spatial detail of the gravity image is significantly lower than that of the magnetic images.

5.3.3 Seismic data example

Figure 5.16 shows the first application of the skeletonization technique to automatic interpretation of seismic data from the Weyburn-Midale Monitoring and Storage Project discussed in Chapters 2 to 4 of this Dissertation. A small portion of a stacked seismic section is shown in Figure 5.16. In Figure 5.16b, the corresponding skeleton image is given, derived by exactly the same 2-D skeletonization algorithm used in the preceding aeromagnetic and gravity-data examples.

The lines in in Figure 5.16 show the automatically picked reflection events, and coloured circles indicate the measured peak and trough amplitudes. These amplitudes were extracted on top of a background trend, which was identified by smoothing using a 30-ms sliding window in time. Note that the connections show the correct trends despite the low-frequency amplitude variations present between 1060–1090 ms in the seismic records (Figure 5.16a). The detailed variations of reflection times and amplitudes are quite apparent in Figure 5.16b and easy to output to other reflection-processing software (for example, residual statics).

Unfortunately, because of the broad scope of this project and also funding and time constraints, I did not pursue the seismic applications of the new skeletonization technique beyond the first attempt shown in Figure 5.16b. The example illustrates the feasibility of automatic feature detection in stacked Weyburn data sections and measurement of their parameters. As described in the next Chapter, in the future, this approach needs to be extended to picking large volumes of stacked data and to detecting AVO anomalies in pre-stack seismic data. Such extensions would fulfill the promise and utilize the power of pattern recognition. In such applications, the advantages of automated image processing

will be most apparent, revealing improved AVO measurements for more precise assessment of the amounts of CO_2 within the reservoir.

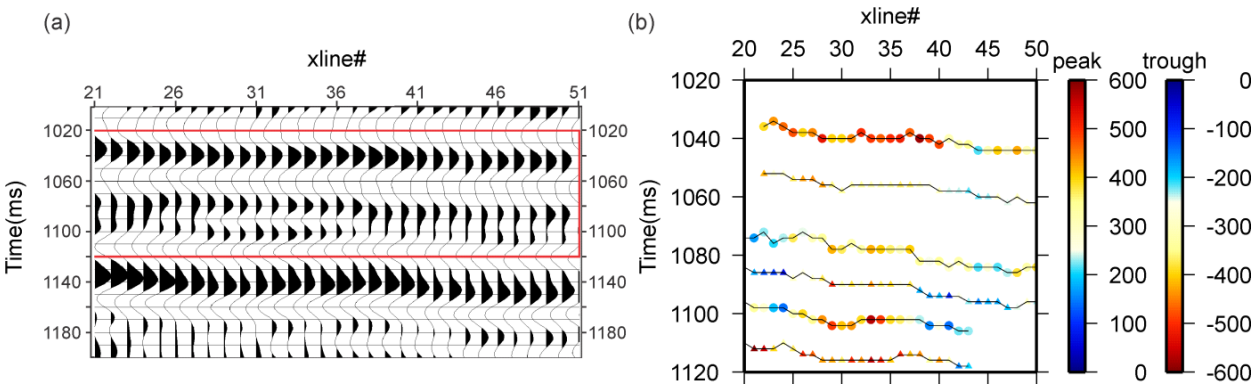

Figure 5.16. Application of skeletonization to Weyburn seismic data: a) stacked section; b) skeleton image from the area marked by the red rectangle (1020 ms to 1120 ms) in plot a), colour bars show amplitudes of peaks and troughs.

5.4 Conclusions

The geophysical skeletonization technique proposed in this Chapter is a powerful, effective and useful tool for pattern recognition in 2-D potential-field and seismic images. The process of skeletonization can help to automatically and objectively identify and characterize various types of amplitude, or AVO anomalies by correlating the adjacent wavelets. Compared with previous methods, this algorithm is more general, isotropic in feature detection, and applicable to arbitrary gridded geophysical data. An important advantage of this algorithm is in its integration in a powerful seismic, well-log, and potential-field data processing system (Chubak and Morozov, 2006; Morozov, 2008). With several innovative options for background-trend extraction, the algorithm provides a more stable identification of lineaments and horizons. The skeleton represents a convenient and quantitative tool for delineating geological structures in the maps or for

auto-picking horizons in seismic images. The wavelets obtained by scanning gridded data along the orientation angles facilitate structure detection and its quantitative characterization.

Applications to both potential-field and seismic data interpretation shows that the skeletonization technique could aid in the interpretation of complex 2-D structures. Skeletonization is particularly useful in combination with 2-D Empirical Mode Decomposition. In future work, these approaches should be particularly useful for refinement of domain and structural-block boundaries, identification of lineation patterns, and for inversion of gridded magnetic and gravity data. The developed technique should also provide a basis for numerous application of 2-D (and in the future, 3-D) skeletonization to improved interpretation of seismic sections and volumes, and also to advanced AVO analysis.

CHAPTER 6

CONLUSIONS AND

DIRECTIONS OF FUTURE RESEARCH

This study focused on extracting the shear wave information from time-lapse 3-D/3-C seismic data and applying it to seismic monitoring of CO_2 injected into the Weyburn reservoir. By using multicomponent instead of conventional single-component data analysis, multiple data sections and volumes were generated containing different information about the P- and S-wave properties of the reservoir.

In this Chapter, I offer three groups of conclusions arising from this study. First, I give main conclusions resulting from the seismic time-lapse 3-C/3-D study (section 6.1). Second, based on the experience gained from this work and correlating its results to other studies, the Weyburn-Midale Monitoring and Storage Project produced a Best Practise Manual, in which several general recommendations from the present Dissertation were included. These recommendations are given in section 6.2. Third, this Dissertation contains a relatively independent and a more general study (skeletonization of geophysical images), and its lessons and conclusions are given in section 6.3. Finally, section 6.4 discusses the directions for future method development and research suggested by work of this Dissertation.

6.1 Conclusions from 3-C/3-D seismic study

In the present study, Amplitude Variation with Angle (AVA) attributes of the reservoir are examined by fluid-substitution modeling and analysis of 3-C/3-D pre-stack surface data. Among the seismic techniques for seismic monitoring of CO_2 injection, which also include P- and P/S-wave reflection imaging and inversion for P- and S-wave impedances, the AVA appears to be the most general and best for assessing the seismic effects of pore pressure and CO_2 saturation of the Weyburn reservoir. From AVA analysis, all of the above seismic attributes can be derived, which is done in the present study for 3-D surface datasets.

AVA modeling showed that the application of Xu's (2006) instead of Batzle-Wang's (1992) equation for calculating the CO_2 properties leads to significantly different fluid-substitution models and AVA attributes. The use of effective porosity in place of total porosity and in conjunction with the shale content correction yields reasonable fluid-substitution models. Using fluid-substitution models based on real well logs yields more realistic AVA attributes than those produced from the traditional two-layered or blocked-log models. Using finite-bandwidth, realistic wavelet in AVA-attribute modeling is also critical for producing synthetics comparable to the real data. Finally, the use of exact reflectivity (Zoeppritz-equivalent) equations rather than their various approximations is essential for accurate modeling of AVA in carbonate reservoirs. At the same time, the two-term, linear AVA attributes (intercept and gradient) model are adequate empirically, and they can be used for classification and interpretation.

Based on detailed AVA modeling, an empirical pressure-CO_2 saturation discriminator is proposed for the Weyburn reservoir. The discriminator is approximately

represented by cut-off CO_2 saturation ($S_c \approx 2\%$) and pore pressure ($p_c \approx$ 18–20 MPa) parameters. It can also be expressed in terms of relative AVA attributes, which makes it independent of the dominant frequency and amplitude of the seismic wavelet. This property should make the proposed discriminator suitable to application to real time-lapse reflection data.

Surface 3-C/3-D reflection datasets from Phase I (acquired in 1999, 2001, and 2002) were re-processed from raw field records. Re-processing included all standard procedures combined with an innovative pre-stack amplitude and wavelet calibration in 3×3-C trace ensembles. Standard processing of each of the three vintages was followed by an assessment of repeatability, three-component transformations, and AVA analysis. The resulting amplitudes and AVA attributes derived above show several temporal trends expected from pore-pressure variations, and with somewhat lower confidence – trends related to CO_2-saturation variations.

Seismic amplitudes and AVO attributes correlate with pore-pressure variations as well as with the injection wells. AVO intercept and gradient variations between different data vintages differentiate CO_2 saturation from pore-pressure. Compared with the forward model, the seismic data show the increasing pore pressure with the decreasing trend of I and increasing G and the increasing CO_2 saturation with decreasing I and G trend. In general, The AVO response for the monitoring datasets is similar to Class III AVO anomalies.

As an investigation of advanced methods for S-wave seismic-data analysis, the receiver-function method was applied to study near-surface structure. The results show that the method is feasible and useful in 3-D/3-C studies and helps in measuring the near-

surface time lags of P- and S-waves in multi-component seismic records. The average time lags of about 35 ms between the primary P and P/S waves were mapped across the study area. Such time lags correspond to near-surface S-wave velocities of 550 m/s. Shallow S-wave velocity estimates allow estimation of S-wave statics that can be useful for converted-wave seismic imaging. Temporal variations within the shallow subsurface were also observed and related to changes in water content.

Analysis of differential travel times in surface-reflection records suggests about 0.5-ms delays accumulated in both monitor datasets over the areas of injection. This could mean that estimated ~10–12 m of the caprock may have been penetrated by CO_2. Qualitatively, such delays are also corroborated by velocity measurements from VSP data.

As an overall conclusion, 3-D active-source seismic monitoring represents the key method for assessing the propagation of injected fluids within the reservoir and the effectiveness of their storage. With improved volumes and quality of recording and further refinement of the imaging and inversion methods described above, quantitative assessment of the propagation of CO2 should become possible, particularly in the zone of low saturation near its front. Joint inversion of 3-D VSP and surface reflection data should help resolving some of the uncertainties of the present work and lead to high-quality seismic AVA analysis.

6.2 Conclusions with regard to CO_2 monitoring

Several general lessons and observations from this as well as similar other studies were noted in the Best-Practise Manual produced as a result of the Weyburn IEA GHG project:

1) Once the CO_2 storage is being undertaken, it is important to monitor its performance periodically, and particularly during early stages of injection. 3-D seismic acquisition is among the best methods for non-invasive monitoring, and practically the only one capable of producing reliable and detailed information about the state of the complete volume of storage, as well as the zones above and below it.

2) In designing seismic studies for CO_2 injection monitoring, it is important to pay attention to the following factors:

   a) If using conventional (explosion) sources, a high-quality vertical-component dataset appears to be more important than a 3-C dataset with sparser coverage. It is recommended that seismic data acquisition is conducted with an AVA analysis in mind. This means that the surveys should use identical (preferably permanently buried) receiver spreads with identical shot patterns and types. Very wide aperture VSP surveys are likely not particularly useful.

   b) However, as 3-C seismic recording is becoming cost-effective and widespread, it should be encouraged for CO_2 monitoring. 3-C seismic data still contains useful additional information that can improve the accuracy of data analysis, including the AVA.

   c) For sufficiently precise calibration of seismic data, it is critical to use as close raw dataset parameters (such as the source and receiver positions ant types) as possible. This would ensure good repeatability of the data in the “pre-stack” domain.

d) If feasible, multiple VSP (*i.e.*, recording the same shots in adjacent wells) could greatly improve the illumination of the subsurface and improve imaging.

e) For datasets with high pre-stack repeatability of data acquisition, seismic processing should also employ time, amplitude, and wavelet calibration at the pre-stack stage.

f) Vertical Seismic Profiling (VSP) should be conducted as a calibration and aid to the surface 3-D recording. At the same time, methods for VSP processing and data analysis still need to be improved in order to confidently constrain the AVA effects observed from surface recording.

3) In terms of seismic attributes that can help distinguish the CO_2 saturation from pressure-related effects, combinations of the AVA intercept (I) and gradient (G) can be used. The monitoring procedure could be similar to the identification of Class III AVA anomalies:

   a) An increase in pore pressure generally decreases I and increases G, *i.e.*, it decreases ($aG–I$), with some $a > 0$. The same variation affects the S-wave reflectivity.

   b) An increase in CO_2 saturation decreases both I and G, *i.e.*, it should be sensitive to combinations like ($I+aG$).

4) CO_2 produces the strongest effect on seismic properties when its saturation is low (below about 3%). This means that seismic monitoring should be conducted at the early stages of injection. Perhaps it would be advisable to conduct two “baseline” surveys prior to CO_2 injection, so that the variability outside of the CO_2 effects can

be studied. This may be particularly important if CO_2 injection follows a history of water injection, as with the Weyburn reservoir.

5) Combining CO_2 injection with enhanced oil recovery (EOR) appears to be the most economically justified approach. Seismic and log data acquired for CO_2 monitoring could provide useful information for the EOR process, and vice versa.

6.3 Conclusions for skeletonization of geophysical images

Skeletonization of 2-D geophysical images is a powerful method which is already useful for quantitatively and automatic interpretation of gridded potential-field images. Applications to several regional-scale aeromagnetic and gravity images show that the method can identify complex geologic structures. Different scales of structures can be identified by combining skeletonization with 2-D empirical mode decomposition.

Specific advantages of the skeletonization scheme developed in this Dissertation are:

1) Its isotropy (absence of preferred feature-detection directions);

2) Use of waveform-based semblance measures and connection cost functions;

3) Integration in a powerful and flexible software package allowing combining this algorithm with numerous other tools for seismic and potential-field data processing.

With additional development, this method should also be successful and useful for automatic picking of AVO anomalies.in pre-stack seismic data and for analysing AVO attribute maps. This approach can identify different attributes related with amplitude and can be generally used in any arbitrary gridded geophysical data. Skeleton images offer straightforward and quantitative ways for auto-picking horizons and detection of various

structures. An application to seismic data illustrates that this technique is feasible for automatic feature detection.

6.4 Recommendations for future research

Seismic data analysis presented in this Dissertation has still not exhausted the potential of Weyburn 3-C/3-D datasets. In particular, converted-wave (P/S) imaging has not been included in this study. Other information, such as water well, precipitation, water table and shallow borehole could be helpful for investigating shallow subsurface. Initial tests at the early stages of this project (by Dr. J. Ma) suggested that P/S imaging was not successful with these 3-D/3-C seismic data. However, with improved imaging techniques and software, such imaging may still be worth exploring. Also, more complete utilization of the three-component recordings could potentially be achieved after further refinement of processing algorithms.

As illustrated by the results of the time-lapse AVO study (Chapter 3), the interpretation of AVO attributes could potentially be improved further. Although most of the AVO results are consistent with injection wells, some attributes appear to be less stable. This suggests that methods for more accurate calibration of the datasets may be needed.

As mentioned in the preceding section, a denser, 1-C/3-D survey could likely provide higher-quality AVO attribute images. For time-lapse imaging, it would also be beneficial to use more vintages of the data, which were not available in this project. The quality of AVO measurements can potentially also be improved by utilizing new

algorithms for pre-stack data analysis. One such innovative type of algorithms tested in this Dissertation is skeletonization.

The present study was the first to use receiver functions (RF) for measuring the properties of the shallow subsurface in exploration seismic data on land. This method should definitely be developed further, and it can be used for practically any reflection dataset. Software tools and improved interpretation approaches need to be created for exploration-scale RF analysis. RF imaging could improve P/S imaging mentioned above.

The skeletonization topic was viewed as a "pilot" study in this project (Chapter 5), and it contains a number of unexplored directions open for development. Based on the initial results of this Dissertation, several lines of further research can be suggested:

4) This approach needs to be applied to large volumes of stacked data and to detect AVO anomalies in pre-stack seismic data.

5) Skeletonized pre-stack seismic data can be used for improving stacking velocity models;

6) Skeletonized pre-stack seismic data can also be very useful for detailed calibration of time-lapse datasets;

7) Skeletonization and empirical model decomposition of AVO and other seismic attribute maps;

8) Potentially, it appears that skeletonization as a "structural" reduction of the data could also be useful in seismic impedance inversion;

9) In gravity and aeromagnetic applications, there exists a broad field of applications for skeletonization in performing structure-based inversion of gridded images. For

example, once a “skeleton” of the image is identified, it can be used to invert for the source and to predict the magnetic field on the surface. By subtracting this predicted field, a new form of field-equation specific “empirical mode deconvolution” would be obtained.

LIST OF REFERENCES

Ammon, C. J., 1991, The isolation of receiver effects from teleseismic P waveforms, Bull. Seismol. Soc. Am., 81, 2504-2510.

Baharvand Ahmadi, A., Gao, L., Ma, J. and Morozov, I., 2011, CO_2 saturation vs. pressure effects from time-lapse 3-D P-S surface and VSP seismic data: Final report as part of IEA GHG Weyburn-Midale CO_2 Monitoring and Storage Project. 102 pp.http://seisweb.usask.ca/Reports/Weyburn_USask_Report_Apr2011.pdf, last accessed 20 Oct 2016

Brown, L.T., 2002, Integration of rock physics and reservoir simulation for the interpretation of time-lapse seismic data at Weyburn Field, Saskatchewan, M.Sc. Thesis, Reservoir Characterization Project, Colorado School of Mines, Golden, Colorado.

Eaton, D., and Vasudevan, K., 2004, Skeletonization of aeromagetic data: Geophysics, 69, 478-488.

Gao, L. and Morozov, I., 2012, Skeletonization of Magnetic-Field Images in Southeastern Saskatchewan and Southwestern Manitoba; in Summary of Investigations 2012, Volume 1, Saskatchewan Geological Survey, Sask. Ministry of the Economy, Misc. Rep. 2012-4.1, Paper A-3, 15p.

Gao, L. and Morozov, I., 2012, Skeletonization of Potential-Field and Seismic Images, Proceedings of 2012 CSPG/CSEG/CWLS Convention, Calgary, AB, Canada, p. 1-5, http://cseg.ca/assets/files/resources/abstracts/2012/117_GC2012_

Skeletonization_of_Potential-Field_and_Seismic_Images.pdf, last accessed 20 Oct 2016

Gao, L. and Morozov, I., 2013, Monitoring CO_2 injection at Weyburn Reservoir Using3-D/3-C seismic datasets, Proceedings of 2012 CSPG/CSEG/CWLS Convention, Calgary, AB, Canada, p. 1-5, http://cseg.ca/assets/files/resources/abstracts/2013/315_GC2013_Monitoring_CO_2_Injection.pdf, last accessed 20 Oct 2016

Gao, L., and Morozov, I.B., 2011, AVO analysis of 3D/3C datasets form Weyburn CO_2 storage and monitoring project, Proceedings of 2011 CSPG/CSEG/CWLS Convention, p. 1-3May 2011, Calgary, AB, Canada, http://cseg.ca/assets/files/resources/abstracts/2011/097-AVO_Analysis_of_3D_3C_Datasets.pdf, last accessed 20 Oct 2016

Gao, L., and Morozov, I.B., 2011, Pressure-saturation effects from AVO attributes in CO_2 monitoring of Weyburn Reservoir, Saskatchewan, Canada, 2011 AGU Fall Meeting.

Gao, L., and Morozov, I.B., 2014, Receiver function analysis of time-lapse 3-C/3-D seismic reflection data, Canadian Journal of Exploration Geophysics, 39, 30-36.

Gao, L., Ma, J., and Morozov, I. B., 2009, Receiver function to improve PS wave statics for Weyburn 4D-3C processing, SEG 2009 Summer Research Workshop – CO_2 Sequestration Geophysics

Hancock, S., 1999, Project brings commercial-scale CO_2 miscible flooding to Canada: Oil and Gas Journal, October.

Hassan, H.H., 2005, Empirical mode decomposition (EMD) of potential field data: airborne gravity data as an example; SEG Technical Program Expanded Abstracts, 2005, p704-706

IEA GHG, 2004, IEA GHG Weyburn CO_2 Monitoring & Storage Project, http://www.ieaghg.org/docs/general_publications/weyburn.pdf, last accessed 20 Oct 2016

Kikuchi, M., and Kanamori, H., 1982, Inversion of complex body waves. Bull. Seismol. Soc. Am. 72, 491–506.

Langston, C.A., 1979, Structure under Mount Rainier, Washington, inferred from teleseismic body waves, Journal of Geophysical Research, 84, 4749-4762.

Lawrence, J. F., and D. A. Wiens, 2004, Combined receiver-function and surface wave phase-velocity inversion using a Niching genetic algorithm: application to Patagonia, Bull. Seismol. Soc. Am., 94, 977-987.

Le, L. H. T., and Nyland, E., 1990, Pattern analysis of seismic records: Geophysics, 55, 20-28.

Li, Q., Vasudevan, K., and Cook, F. A., 1997, Seismic skeletonization: A new approach to interpretation of seismic reflection data: Journal of Geophysical Research, 102, 8427-8445.

Li, Y., 2002, A new method for converted wave statics correction, SEG 72nd Annual Meeting Extended Abstracts, 979-981.

Li, Y., Ma, Z., Sun, P., and Yang, H., 2012, Converted-wave static correction method for thick weathering area, Chinese Journal of Geophysics, 55, 76-83.

Lu, S. Y., and Cheng, Y. C., 1990, An iterative approach to seismic skeletonization: Geophysics, 55, 1312-1320.

Ma, J., Gao, L. and Morozov, I., 2009. Time-lapse repeatability in 3C-3Ddataset from Weyburn CO_2 Sequestration Project, Proceedings of 2009 CSPG/CSEG/ CWLS Convention, Calgary, AB, Canada, p. 255-258, http://cseg.ca/assets/files/resources/abstracts/2009/096.pdf, last accessed20 Oct 2016.

Ma, J., and I. Morozov, 2010, AVO modeling of pressure-saturation effects in Weyburn CO_2 sequestration, The Leading Edge, Feb 2010, 178–183.

Ma, J., and Morozov, I., 2010, AVO modelling of pressure-saturation effects in Weyburn CO_2 sequestration: The Leading Edge, 29, 178-183.

Meersman, Kristof De, 2013, S-waves and the near surface: a time-lapse study of S-wave velocity and attenuation in the weathering layer of an Alberta heavy oil field, The Leading Edge, 32, 40-47.

Moreira, L. P., Friedel, M. J., and França, G. S., 2013, Uncertainty analysis in the joint inversion of receiver function and surface-wave dispersion, Paraná Basin, Southeast Brazil, Bull. Seismol. Soc. Am., 103, 1981-1992.

Morozov, I. B. and Din, M., 2008, Use of receiver functions in wide-angle controlled-source crustal data sets: Geophys. J. Int., 173, 299-308.

Morozov, I. B., 2008, Open-source software integrates data analysis, EOS Trans. Am. Geophys. U., 89 (29), 261-262.

Morozov, I. B., 2009, Advanced geophysical attributes in southern Saskatchewan and Southwestern Manitoba; in Summary of Investigations 2009, Volume 1, Saskatchewan Geological Survey, Sask. Ministry of Energy and Resources, Misc. Rep. 2009-4.1, Paper A2, 11pp.

Morozov, I. B., and Gao, L., 2009, Pre-stack Calibration of 3-C 3-D time-lapse seismic data, Proceedings of 2009 CSPG/CSEG/CWLS Convention, Calgary, AB, Canada, Calgary, AB, Canada, p. 215-219, http://cseg.ca/assets/files/resources/abstracts/2009/101.pdf, last accessed 20 Oct 2016.

Morozov, I.B., and Gao, L., 2016, Receiver functions with artificial sources in: Thybo, H. (Ed.), Encyclopedia of Earthquake Engineering, Springer. Springer-Verlag Berlin Heidelberg 2016, p. 1–25, DOI 10.1007/978-3-642-36197-5_375-1

Morozov , I. B., M. Haiba, and W. Deng, Inverse attenuation-filtering, Geophysics, in revision.

Morozov, I.B., Smithson, S.B., Hollister, L.S. and J.B. Diebold, 1998, Wide-angle seismic imaging of accreted terranes in SE Alaska and British Columbia, Tectonophysics, 299, 281-296.

Russell, B., 1988, Introduction to seismic inversion methods, The SEG course notes Series, 2.

van Manen,, D., Robertsson, J.O.A., Curtis, A., Ferber, R., and Paulssen, H., 2003, Shear wave statics using receiver functions, Geophys. J. Int., 153, F1-F5.

Vinnik, L. P. 1977, Detection of waves converted from P-to-SV in the mantle, Phys. Earth Planet Inter, 15, 294-303.

Wegelin, A., 1984, Geology and reservoir properties of the Weyburn field, southeastern Saskatchewan, in J.A. Lorsong and M.A. Wilsons, eds., Oil and Gas in Saskatchewan: Saskatchewan Geological Society Spec. Pub. No. 7, p. 71-88.

Weyburn Phase I Report, 2004. IEA GHG Weyburn CO_2 Monitoring & Storage Project Summary Report 2000-2004, Proceedings of the 7th International Conference on Greenhouse Gas Control Technologies, Volume III, Sept. 5-9, 2004, Vancouver, CA

White, D., 2009, Monitoring CO_2 Storage during EOR at the Weyburn-Midale Field, The Leading Edge, 28, 838-842.

White, D. J., K. Hirsche, T. Davis, I. Hutcheon, R. Adair, G. Burrowes, S. Graham, R. Bencini, E. Majer, S. C. Maxwell, 2004, Theme 2: Prediction, Monitoring and Verification of CO_2 movements, in M. Wilson and M. Monea, eds., IEA GHG CO_2 Monitoring and Storage Project Summary Report 2000–2004, PTRC, Regina, 2004.

White, D., 2013, Seismic characterization and time-lapse imaging during seven years of CO_2 flood in the Weyburn field, Saskatchewan, Canada: International Journal of Greenhouse Gas Control, 165, 578-594.

Xu, H., 2006, Calculation of CO2 acoustic properties using Batzle-Wang equations: Geophysics, 71, F21–F23.

Zoeppritz, K., 1919, Erdbebenwellen VII. VIIb. Über Reflexion und Durchgang seismischer Wellen durch Unstetigkeitsflächen. Nachrichten von der Königlichen Gesellschaft der Wissenschaften zu Göttingen, Mathematisch-physikalische Klasse, 66-84.